

**STUDIES ON TRANSPORT AND MAGNETIC PROPERTIES OF
NANO PARTICLE DOPED MgB_2 SUPERCONDUCTOR FOR
TECHNOLOGICAL APPLICATIONS**

Thesis submitted to
Cochin University of Science and Technology

for the degree of
Doctor of Philosophy

in
Physics

by
NESON VARGHESE

under the supervision of
Dr. U. Syamaprasad



National Institute for Interdisciplinary Science and Technology
Council of Scientific and Industrial Research (CSIR)
Trivandrum-695019

May 2012



Studies on transport and magnetic properties of nano particle doped MgB_2 superconductor for technological applications

Ph. D. Thesis

May 2012

T 562

T
538.945
NES



Author:

Neson Varghese
Applied Superconductivity Group
Material Science and Technology Division
National Institute for Interdisciplinary Science and Technology (CSIR)
Trivandrum-695019
Email: nesonvarghese@gmail.com
Tel: 9895357167 (Mob)


Supervising guide:

Dr. U. Syamaprasad
Chief Scientist & Head
Applied Superconductivity Group
Material Science and Technology Division
National Institute for Interdisciplinary Science and Technology (CSIR)
Trivandrum-695019
Email: syamsir@gmail.com
Tel: 0471 2515373 (Off)

Cover Page Illustration: MgB_2 crystal structure (front)
 MgB_2 - typical characterizations (back)

DECLARATION

I, **Neson Varghese**, hereby declare that, the thesis entitled "*Studies on transport and magnetic properties of nano particle doped MgB₂ superconductor for technological applications*" is a bonafide record of the research work done by me under the supervision and guidance of Dr. U. Syamaprasad, Chief Scientist, National Institute for Interdisciplinary Science and Technology (CSIR), Trivandrum and no part of this dissertation has been submitted previously for the award of any degree in any other University.


Neson Varghese

Trivandrum
2 May 2012

NATIONAL INSTITUTE FOR INTERDISCIPLINARY SCIENCE AND TECHNOLOGY (NIIST)



(Formerly Regional Research Laboratory, Thiruvananthapuram)

Council of Scientific & Industrial Research
Industrial Estate PO, Trivandrum – 695 019, Kerala, INDIA

Tel : 91-471-2515 373 / 2515 233; Fax : +91-471-2491 712 / 2490 186


E-mail : svamcsir@gmail.com; svam@niist.res.in



Dr. U. SYAMAPRASAD
Chief Scientist and Head
Applied Superconductivity Group

CERTIFICATE

This is to certify that the thesis entitled “*Studies on transport and magnetic properties of nano particle doped MgB₂ superconductor for technological applications*” is an authentic record on the research work carried out by **Mr. Neson Varghese**, under my supervision in partial fulfillment of the requirement for the degree of Doctor of Philosophy of the Cochin University of Science and Technology and further that no part of this thesis has been presented previously for the award of any other degree.


U. Syamaprasad
(Research Guide)

Trivandrum

2 May 2012

*Dedicated to
my family ...*

ACKNOWLEDGEMENTS

I take this opportunity to sincerely acknowledge all those who have contributed in different aspects for the completion of my Ph. D. work and preparation of the thesis.

First and foremost, I praise the almighty for bestowing upon me with abundant love, inspiration, wisdom, determination and good health during the period and for showering his blessings throughout my life.

I would like to express my deep sense of gratitude to my supervising guide, Dr. U. Syamaprasad, Chief Scientist and Head, Applied Superconductivity Group, for his timely suggestions and support during the course of my research work. I could benefit a lot from his excellent ideas and invaluable academic experience, which would certainly help me in future.

I am also very grateful to Dr. Suresh Das, Director, NIIST (CSIR), and Dr. B. C. Pai and Dr. T. K. Chandrashekar, former Directors, for providing all the necessary facilities to carry out this work.

Next, I wish to sincerely thank Mr. P. Guruwsamy, Technical Officer, NIIST (CSIR), for his encouragement and support during the entire period.

I also extend my heartfelt thanks to Mr. M. R. Chandran, Mr. Robert Philip, Mr. Kiran Mohan and Mr. Peer Mohammad for extending different instrumental facilities such as SEM, HRTEM and optical microscope.

I take this chance to sincerely thank Dr. A. Sundaresan, Jawaharlal Nehru Centre for Advanced Scientific Research (JNCASR), Bangalore, Dr. S. B. Roy, Raja Ramanna Centre for Advanced Technology (RRCAT), Indore and Dr. S. Pradhan, Institute for Plasma Research (IPR), Gandhinagar, for experimental equipment support, scientific discussions and collaboration. I also thank Prof. Ashok Rao, Department of Physics, Manipal Institute of Technology, Manipal, and Prof. Y. K. Kuo, Department

of Physics, National Dong Hwa University, Hualien, Taiwan, for experimental support.

It is indeed a pleasure to thank Dr. K. P. Vijayakumar, Head, Department of Physics, Cochin University of Science and Technology, Cochin, for his co-operation and support during both my post graduation period and at various stages of this Ph. D. work. I also express my sincere thanks to Dr. K. G. K. Warriar, Emeritus Scientist, NIIST (CSIR), for encouraging me by attending my assessment presentations.

I am also thankful to my colleagues, R. G. Abhilashkumar, K. Vinod, Syju Thomas, S. Rahul, K. M. Devadas, P. Anees, A. Sivaprakash, S. Santhoshkumar, G. R. Anuraghi, K. T. Jakson, V. F. Rinu, M. Maheshkumar and M. Firozkhan who have supported me intellectually and technically.

I would also like to thank J. B Anooja and P. M. Aswathy for assisting me in rectifying the typographical errors, as much as possible.

Apart from the works related to MgB_2 , I would like to cherish and acknowledge the friendship and support of my colleagues and friends, P. M. Sarun, R. Shabna, S. Vinu, A. Nazeer and S. S. Surya.

I owe my sincere gratitude to my senior colleagues Dr. A. Biju, Principal, M. E. S. Asmabi College, Kodungalloor, and Dr. R. P. Aloysius, Senior Scientist, National Physical Laboratory, New Delhi, for their backing at various stages of my Ph. D. work.

The warm support of all my friends in NIIST has enabled me to complete this thesis and to have a wonderful time along the way.

I am obliged to the NIIST administration for facilitating all the timely help. I also sincerely acknowledge CSIR for providing me with the fellowship.

At last but not the least, I wish to thank my family from the bottom of my heart for providing me enough moral values, privileged education and unconditional support at each turn of the road.

PREFACE

Even after a century of its discovery, superconductivity is one of the captivating topics of modern science with its extensive range from the most elementary aspects of physics to hands-on applications. Significant progress has occurred in the field of superconductivity and the improvements are being sensibly incorporated into the new generation wires, tapes and cables that are being used in a broad range of prototype devices. These devices include NMR magnets, MRI instruments, magnets for fusion power experiments, high field accelerators, motors, generators, and power transmission lines.

Though there are thousands of superconducting materials, only a few of them are suitable for practical applications. The discovery of high temperature superconductors with critical temperature (T_C) above 77 K stimulated the development of superconductors for power applications, yet the most widely used commercial superconductors are NbTi and Nb₃Sn, the two low temperature superconducting materials. The discovery of superconductivity in MgB₂ in early 2001 with relatively higher T_C (39 K), simpler structure, lower anisotropy and nearly transparent grain boundaries spurred renewed interest due to its potential for magnetic applications. The material has already been studied in terms of its crystal structure, thermal and electrical conduction, specific heat, isotope effect and doping effects. Though its T_C is lower than high temperature cuprates, MgB₂ is an intermetallic with very low contact resistance between the grain boundaries, eliminating the weak-link problem that has plagued widespread commercialization of the cuprates. Further, relatively higher coherence length of MgB₂, in comparison to HTS compounds, permits the use of nano particles of various compounds as additives to act as effective pinning centers and thereby enhance its critical current. These superior properties in

comparison to the so called intermetallic BCS type superconductors and HTS cuprates provide MgB_2 an edge over the other superconductors. In addition, the conduction electron density and normal state conductivity are about two orders of magnitude higher for MgB_2 than the cuprates used in present day wires. These features, combined with the low cost, lightweight, and easy fabrication of wires and thin films, make MgB_2 attractive for many applications such as MRI, transformers and generators especially on board in air and sea, where weight is a concern. It is a strong competitor for the currently used NbTi and Nb_3Sn conductors because it can be operated around the 20-30 K temperature range, above the range of current use of LTS. In this range the expensive liquid helium can be avoided and liquid hydrogen or cryocooler can be used. Hence, among the superconducting materials discovered so far, MgB_2 seems to be a potential candidate for the next generation superconductor applications.

The thesis ahead focuses on the establishment of enhanced superconducting properties in bulk MgB_2 via nano particle doping and its conversion into mono/multifilamentary wires. Further, an attempt has also been made to develop prototypes of MgB_2 coil and conduction cooled current lead for technological applications. The thesis is configured into 6 chapters. The opening chapter gives an idea on the phenomenon of superconductivity, the various types of superconductors and its applications in different fields. The second chapter is an introduction on MgB_2 superconductor and its relevance which includes crystal and electronic structure, superconducting mechanism, basic superconducting properties along with its present international status. The third chapter provides details on the preparation and characterization techniques followed through out the study on MgB_2 . Fourth chapter discusses the effect of processing temperature and chemical doping using nano sized dopants on the superconducting properties of MgB_2 . Fifth chapter deals with the optimization of processing parameters and novel preparation techniques for

wire fabrication. Sixth chapter furnishes the preparation of multifilamentary wires with various filament configurations, their electromechanical properties and it also incorporates the development of an MgB_2 coil and a general purpose conduction cooled current lead. The seventh chapter summarizes the major findings and conclusions of the entire work and also provides the scope for future studies.

MgB_2 bulk superconductor is synthesized using a simple Powder-In-Sealed-Tube (PIST) method wherein Mg and B powders were filled in stainless steel tubes and heat treated in atmospheric condition after sealing the ends. The method is simple and cost effective, as it avoids the demand for vacuum or inert atmosphere during synthesis. The in-field current density of the pristine MgB_2 is enhanced using various nano sized dopants. Among the different dopants tried, burned rice husk (BRH), an inexpensive natural material is found to be one of the best additives for enhancing the in-field critical current density of MgB_2 . By selecting suitable combinations of additives a significant enhancement of the critical current density around two orders of magnitude was achieved at higher fields. Later, the focus was on the translation of these properties in mono/multifilamentary wires with various configurations. The influence of sheath material reactivity on the superconducting properties of MgB_2 was studied first which was followed by process optimization studies. Further, the influence of typical nano dopants on the in-field transport J_C of multifilamentary $\text{MgB}_2/\text{Fe}/\text{Cu}/\text{Ni}$ wires was examined. It was observed that the in-field J_C of doped MgB_2 multifilamentary wires showed excellent performance, relatively better than the corresponding bulk samples. Another achievement in conductor fabrication was the lowering of the processing temperature of MgB_2 wires using nano Cu as an additive. It was found that the MgB_2 can be synthesized at around 550 °C with minor Cu addition, which offers a substantial reduction in the processing temperature. In addition, Fe sheathed *in situ* MgB_2 superconducting tapes with high densities were prepared by hot-

pressing of electrically self-heated PIT wires. The method comprised heating of the PIT wires by passing a suitable current, followed by pressing in hot conditions with the help of a hydraulic press. The other highlights of the thesis are the development of a prototype MgB_2 coil having an overall homogenous $J_C \sim 10^5 \text{ A/cm}^2$ at 4.2 K and a general purpose conduction cooling type current lead based on $\text{MgB}_2/\text{Fe}/\text{Cu}/\text{Ni}$ with rating 1000 A at 20-37 K.

In brief, the work compiled in this thesis brings out the influence of nano particle doping in both bulk as well as wire forms of MgB_2 . Moreover, the development of prototype for coil and conduction cooled current lead shows the potential of MgB_2 for technological applications. It is expected that the findings in the thesis can contribute much towards further development in MgB_2 .

List of Publications

► **Articles in SCI journals:**

1. **Neson Varghese, K. Vinod, S. Rahul, K. M. Devadas, Syju Thomas, S. Pradhan and U. Syamaprasad**, "*Influence of nano Cu additive on MgB₂ phase formation, processing temperature and transport properties.*" **Journal of Applied Physics** 109, 033902 (2011)
2. **Neson Varghese, K. Vinod, S. Rahul, P. Anees, K. M. Devadas, Syju Thomas, Shipra, A. Sundaresan, S. B. Roy and U. Syamaprasad**, "*Effect of carbon substitution on the superconducting properties of nano carbon, diamond and SiC doped MgB₂.*" **Journal of the American Ceramic Society** 94, 1133 (2011)
3. **Neson Varghese, K. Vinod, Shipra, A. Sundaresan and U. Syamaprasad**, "*Burned Rice Husk: An Effective Additive for Enhancing the Electromagnetic Properties of MgB₂ Superconductor.*" **Journal of the American Ceramic Society** 93, 732 (2010)
4. **Neson Varghese, K. Vinod, M. K. Chattopadhyay, S. B. Roy and U. Syamaprasad**, "*Effect of combined addition of nano-SiC and nano-Ho₂O₃ on the in-field critical current density of MgB₂ superconductor.*" **Journal of Applied Physics** 107, 013907 (2010)
5. **Neson Varghese, K. Vinod, U. Syamaprasad and S. B. Roy**, "*Doping effect of nano-SiC on structural and superconducting properties of MgB₂ bulks prepared by PIST method in air.*" **Journal of Alloys and Compounds** 484, 734 (2009)
6. **Neson Varghese, K. Vinod, A. Rao, Y. K. Kuo and U. Syamaprasad**, "*Enhanced superconducting properties of bulk MgB₂ prepared by in situ Powder-In-Sealed-Tube method.*" **Journal of Alloys and Compounds** 470, 63 (2009)
7. **Neson Varghese, K. Vinod, R. G. A. Kumar, U. Syamaprasad and A. Sundaresan**, "*Influence of reactivity of sheath materials with Mg/B on superconducting properties of MgB₂.*" **Journal of Applied Physics** 102, 043914 (2007)

8. S. Rahul, **Neson Varghese**, K. Vinod, K. M. Devadas, Syju Thomas, P. Anees, M. K. Chattopadhyay, S. B. Roy and U. Syamaprasad, “*Combined addition of nano diamond and nano SiO₂: an effective method to improve the in-field critical current density of MgB₂ superconductor,*” **Materials Research Bulletin** 46, 2036 (2011)
9. K. M. Devadas, S. Rahul, S. Thomas, **Neson Varghese**, K. Vinod, U. Syamaprasad, S. Pradhan, M. K. Chattopadhyay and S. B. Roy, “*Transport properties of sealed MgB₂/Fe/Ni multifilamentary wires heat treated in air,*” **Journal of Alloys and Compounds** 509, 8038 (2011)
10. K. Vinod, **Neson Varghese**, S. Rahul, K. M. Devadas, Syju Thomas, P. Guruswamy, S. Kedia, S Pradhan and U. Syamaprasad, “*On the current transfer length and current sharing in short length MgB₂ wires,*” **Superconductor Science and Technology** 23, 105002 (2010)
11. K. Vinod, **Neson Varghese**, A. Sundaresan and U. Syamaprasad, “*Highly enhanced in-field critical current density of MgB₂ superconductor by combined addition of burned rice husk and nano Ho₂O₃,*” **Solid State Sciences** 12, 610 (2010)
12. K. Vinod, **Neson Varghese**, S. Rahul and U. Syamaprasad, “*Preparation of in situ MgB₂/Fe superconducting tapes with highly densified core by hot pressing of electrically self-heated PIT wires,*” **Materials Science and Engineering B-Advanced Functional Solid-State Materials** 164, 131 (2009)
13. K. Vinod, **Neson Varghese**, S. B. Roy and U. Syamaprasad, “*Significant enhancement of the in-field critical current density of the MgB₂ superconductor through codoping of nano-TiC with nano-SiC,*” **Superconductor Science & Technology** 22, 055009 (2009)
14. K. Vinod, **Neson Varghese**, U. Syamaprasad, Shipra and A. Sundaresan, “*Structural and superconducting properties of bulk MgB₂ with added nano Tb₄O₇,*” **Superconductor Science & Technology** 21, 025003 (2008)
15. K. Vinod, **Neson Varghese**, R. G. A. Kumar, U. Syamaprasad and S. B. Roy, “*Influence of Mg particle size on the reactivity and superconducting properties of in situ MgB₂,*” **Journal of Alloys and Compounds** 464, 33 (2008)
16. R. G. A. Kumar, K. Vinod, **Neson Varghese** and U. Syamaprasad, “*Reactivity of sheath materials with Mg/B in MgB₂ conductor fabrication,*” **Superconductor Science & Technology** 20, 222 (2007)

► Topical review:

1. K. Vinod, **Neson Varghese** and U. Syamaprasad, “*Superconductivity of MgB_2 in the BCS framework with emphasis on extrinsic effects on critical temperature,*” *Superconductor Science & Technology* 20, R31-R45 (2007)

► Chapter of book:

1. K. Vinod, **Neson Varghese** and U. Syamaprasad, “*Development of MgB_2 superconductors with improved superconducting properties*”, In: **Advances in Materials Science Research. Volume 3** (Nova Science Publishers, Inc.), ISBN: 978-1-61728-998-9 (2009)

► Articles presented in International/National Conferences:

1. **Neson Varghese**, K. Vinod, R. G. Abhilash Kumar and U. Syamaprasad “*Chemical compatibility of sheath materials for in situ MgB_2 superconductor wire/tape fabrication,*” Presented at the International Conference on Advanced Materials and Composites (ICAMC), held at NIIST Thiruvananthapuram on October 24-26, 2007 (Also published in the proceedings: page 773-778)
2. K. Vinod, **Neson Varghese**, R. G. Abhilash Kumar and U. Syamaprasad “*Influence of heat treatment temperature and duration on the crystalline and microstructural properties of insitu MgB_2 superconductor,*” Presented at the International Conference on Advanced Materials and Composites (ICAMC), held at NIIST Thiruvananthapuram on October 24-26, 2007 (Also published in the proceedings: page 784-788)
3. K. Vinod, **Neson Varghese** and U. Syamaprasad “*Effect of sintering temperature on the microstructure and superconducting properties of insitu polycrystalline MgB_2 ,*” Presented at the 52nd DAE Solid State Physics Symposium (DAE SSPS 2007), held at Mysore on December 27-31, 2007 (Also published in the proceedings: vol 52 page 791-792)
4. **Neson Varghese**, K. Vinod, S. B. Roy and U. Syamaprasad “*Enhancement of high field critical current density in nano-SiC doped MgB_2 prepared by Powder-In-Sealed-Tube method,*” Presented at the 53rd DAE Solid State Physics Symposium (DAE SSPS 2008), held at Mysore on December 27-31, 2008 (Also published in the proceedings: vol 53 page 897-898)

5. K. Vinod, **Neson Varghese**, S. Rahul and U. Syamaprasad “*Hot pressing of electrically self heated MgB₂/Fe PIT wires,*” Presented at the 53rd DAE Solid State Physics Symposium (DAE SSPS 2008), held at Mysore on December 27-31, 2008 (Also published in the proceedings: vol 53 page 919-920)
6. **Neson Varghese**, J. B. Anooja, P. M. Aswathy, K. Vinod, S. B. Roy and U. Syamaprasad “*Effect of combined addition of nano SiC and TiC on structural and superconducting properties of MgB₂,*” Presented at the International Conference on Advanced Functional Materials (ICAFM) held at NIIST, Thiruvananthapuram on December 9-10, 2009
7. S. Rahul, G. R. Anuraghi, K. T. Jackson, **Neson Varghese**, K. Vinod and U. Syamaprasad “*Codoping effect of burned rice husk and nano Ho₂O₃ on the in-field critical current density of MgB₂ superconductor,*” Presented at the International Conference on Advanced Functional Materials (ICAFM) held at NIIST, Thiruvananthapuram on December 9-10, 2009
8. K. Vinod, **Neson Varghese**, S. Rahul, P. Anees, P. Guruswamy and U. Syamaprasad “*Current sharing between sheath and superconductor for Fe, Cu and Ti sheathed MgB₂ superconductor,*” Presented at the International Conference on Advanced Functional Materials (ICAFM) held at NIIST, Thiruvananthapuram on December 9-10, 2009
9. K. M. Devadas, **Neson Varghese**, K. Vinod, S. Rahul, Syju Thomas, J. B. Anooja, A. Sundaresan, S. B. Roy and U. Syamaprasad, “*Enhanced superconducting properties of MgB₂ by carbon substitution using Carbon containing nano additives,*” Presented at the 55th DAE Solid State Physics Symposium (DAE SSPS 2010), held at Manipal on December 26-30, 2010 (Published in **AIP Conf. Proc. 1349, 913-914**)
10. **Neson Varghese**, K. Vinod, S. Rahul, K. M. Devadas, Syju Thomas, P. M. Aswathy, S. Pradhan, and U. Syamaprasad, “*Lowering the sintering temperature of MgB₂/Fe wires with high transport current by nano Cu doping,*” Presented at the 55th DAE Solid State Physics Symposium (DAE SSPS 2010), held at Manipal on December 26-30, 2010 (Published in **AIP Conf. Proc. 1349, 891-892**)
11. S. Rahul, **Neson Varghese**, K. Vinod, K. M. Devadas, Syju Thomas, P. Anees, M. K. Chattopadhyay, S. B. Roy, R. P. Aloysius and U. Syamaprasad, “*Nano Diamond and Nano SiO₂ – An Effective Combination to Improve the In-Field Properties of MgB₂ Superconductor,*” Presented at the 55th DAE Solid State

Physics Symposium (DAE SSPS 2010), held at Manipal on December 26-30, 2010 (Published in **AIP Conf. Proc.** 1349, 909)

12. **Neson Varghese**, S. Rahul, K. M. Devadas, Syju Thomas, A. Sundaresan, S. B. Roy and U. Syamaprasad, "*A comparative study on the structural and superconducting properties of carbon variants doped MgB_2* ," Presented at the *Asian Conference on Applied Superconductivity and Cryogenics (ACASC 2011)* held at IUAC, New Delhi on November 16-18, 2011
13. Syju Thomas, **Neson Varghese**, S. Rahul, K. M. Devadas, K. Vinod, G. R. Anuraghi and U. Syamaprasad, "*Enhancement of bending strain tolerance and current carrying property of MgB_2 based multifilamentary wires*," Presented at the *Asian Conference on Applied Superconductivity and Cryogenics (ACASC 2011)* held at IUAC, New Delhi on November 16-18, 2011
14. K. M. Devadas, **Neson Varghese**, S. Rahul, Syju Thomas, S. Pradhan, P. Guruswamy and U. Syamaprasad, "*Development of MgB_2 based conduction cooled current leads with ratings up to 1000 A*," Presented at the *Asian Conference on Applied Superconductivity and Cryogenics (ACASC 2011)* held at IUAC, New Delhi on November 16-18, 2011
15. S. Rahul, K. M. Devadas, Syju Thomas, **Neson Varghese**, K. Vinod, S. Pradhan, M. K. Chattopadhyay, S. B. Roy and U. Syamaprasad, "*Transport properties of MgB_2 based multifilamentary wires heat treated in air*," Presented at the *Asian Conference on Applied Superconductivity and Cryogenics (ACASC 2011)* held at IUAC, New Delhi on November 16-18, 2011

CONTENTS

Chapter 1: Overview on superconductivity

1.1	History in brief	1
1.2	Basic characteristics of the superconducting state	5
1.3	Superconducting materials	10
1.4	Applications of superconductors	16
	References	22

Chapter 2: MgB₂ superconductor – Relevance and applications

2.1	Introduction to MgB ₂ superconductor.....	25
2.1.1	History and background.....	25
2.1.2	Why is MgB ₂ so special?.....	26
2.2	Structural and superconducting properties of MgB ₂	28
2.2.1	Crystal and electronic structure	28
2.2.2	Superconducting Mechanism	31
2.3	Basic superconducting parameters.....	33
2.3.1	Critical temperature (T_C)	33
2.3.2	Critical Current Density (J_C)	34
2.3.3	Critical Field (H_C)	35
2.4	Preparation of MgB ₂ superconductor.....	36
2.4.1	Bulk samples.....	37
2.4.1.1	<i>In situ</i> preparation.....	37
2.4.1.2	Mechanical alloying	38
2.4.1.3	Powder in sealed tube method (PIST)	39
2.4.1.4	Hot Isostatic Pressing (HIP)	39
2.4.2	Wire/tape samples.....	40
2.4.2.1	Diffusion method.....	41
2.4.2.2	Coating techniques	41
2.4.2.3	Powder in tube method (PIT)	42
2.4.3	Thin film	42
2.4.4	Single crystal	43
2.5	Chemical doping effects.....	43
2.6	MgB ₂ – Relevance and applications.....	45
2.7	Objectives of the present work.....	47
	References	49

Chapter 3: Preparation and characterization techniques

3.1	Preparation of MgB ₂ samples	59
3.1.1	Bulk MgB ₂	59
3.1.2	Preparation of MgB ₂ conductors	60
3.1.2.1	Monofilamentary wires	60
3.1.2.2	Multifilamentary wires	61
3.1.2.3	MgB ₂ coils	62
3.1.2.4	MgB ₂ current leads	62
3.2	Structural characterization methods	62
3.2.1	X-ray diffraction (XRD) analysis.....	62
3.2.2	Microstructural characterization methods	64
3.2.2.1	Optical microscopy	64
3.2.2.2	Scanning electron microscopy (SEM)	64
3.2.2.3	Transmission electron microscopy (TEM)	65
3.3	Techniques used for superconducting characterization	65
3.3.1	Magnetization measurements	66
3.3.2	Transport measurements	66
	References	71

Chapter 4: Effect of processing temperature and various nano dopants on the properties of bulk MgB₂

4.1	Introduction	73
4.2	Preparation and characterization of bulk MgB ₂	74
4.3	Pristine MgB ₂ : Effect of processing temperature on structural and superconducting properties	75
4.3.1	Introduction	75
4.3.2	Results and discussion	76
4.3.3	Conclusion.....	81
4.4	Nano oxide doped MgB ₂ : A comparative study on structural and superconducting properties	81
4.4.1	Introduction	81
4.4.2	Results and discussion	82
4.4.3	Conclusion.....	87
4.5	Carbon variants doped MgB ₂ : A comparative study on structural and superconducting properties	87
4.5.1	Introduction	87
4.5.2	Results and discussion	89

4.5.3	Conclusion	96
4.6	Codoped MgB ₂ : An effective method for enhancing the in-field critical current density of MgB ₂	96
4.6.1	Introduction	96
4.6.2	Results and discussion	97
4.6.3	Conclusion	103
4.7	Summary	104
	References	105

Chapter 5: Optimization of processing parameters and novel preparation techniques for MgB₂ wires

5.1	Introduction	109
5.2	Influence of reactivity of sheath materials with Mg/B on superconducting properties of MgB ₂	110
5.2.1	Introduction	110
5.2.2	Results and discussion	111
5.2.3	Conclusion	115
5.3	Effect of processing temperature on the transport critical current of MgB ₂ /Fe superconducting wires	115
5.3.1	Introduction	115
5.3.2	Preparation and characterization of MgB ₂ /Fe monofilamentary wires	116
5.3.3	Results and discussion	118
5.3.4	Conclusion	122
5.4	Influence of nano Cu additive on MgB ₂ phase formation, processing temperature and transport properties.....	123
5.4.1	Introduction	123
5.4.2	Results and discussion	124
5.4.3	Conclusion	129
5.5	Preparation of MgB ₂ /Fe superconducting tapes with highly densified core by hot-pressing of <i>in situ</i> PIT wires.....	130
5.5.1	Introduction	130
5.5.2	Preparation and characterization of hot-pressed <i>in situ</i> PIT wires.....	131
5.5.3	Results and discussion	132
5.5.4	Conclusion	136
5.6	Summary	136
	References	137

Chapter 6: Development of MgB₂ multifilamentary wires, coils and current leads for technological applications

6.1	Introduction	141
6.2	Development of MgB ₂ multifilamentary wires with enhanced in-field critical current density	142
6.2.1	Introduction	142
6.2.2	Preparation and characterization of MgB ₂ multifilamentary wires	142
6.2.2.1	Outer sheath variation	142
6.2.2.2	Dopant variation	144
6.2.3	Results and discussion	144
6.2.3.1	Effect of outer sheath variation	144
6.2.3.2	Effect of nano dopants on in-field J_C	147
6.2.4	Conclusion	149
6.3	Electromechanical properties of multifilamentary wires and development of an MgB ₂ coil	149
6.3.1	Preparation and characterization	150
6.3.1.1	Variation in filament configuration	150
6.3.1.2	Bent & react and react & bent wires	151
6.3.1.3	MgB ₂ coil	152
6.3.2	Results and discussion	153
6.3.3	Conclusion	158
6.4	Development of MgB ₂ based current lead	159
6.4.1	Preparation and characterization of MgB ₂ current lead	160
6.4.2	Results and discussion	162
6.4.3	Conclusion	164
6.5	Summary	164
	References	165

Chapter 7: Summary and conclusions

7.1	Summary	167
7.2	Conclusions	168
7.3	Scope for future work	171
i.	List of symbols	173
ii.	List of abbreviations	175

1

OVERVIEW ON SUPERCONDUCTIVITY

1.1 History in brief

Superconductivity has been an exciting, fascinating and challenging topic since its discovery in 1911. Thousands of materials have been found to exhibit this phenomenon in the temperature range of a few mK to 164 K. Besides pure elements, almost all categories of materials seem to show superconductivity, including metallic alloys, intermetallics, metallic glasses, ceramics, inorganic and organic polymers and various forms of carbon like fullerenes. Over the last 10 decades, the field has proved itself to be extraordinarily rich and dynamic with new discoveries, in the form of a novel material or phenomenon.

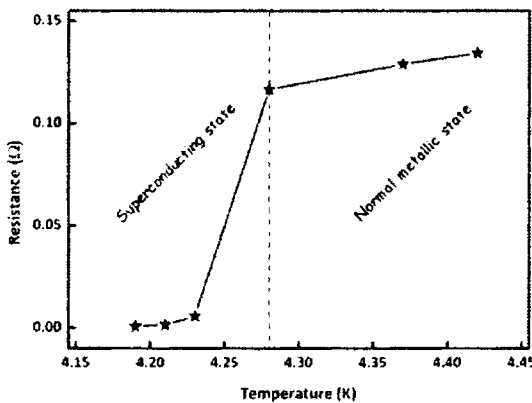


Figure 1.1: Variation of resistance with temperature for Hg obtained by Kamerlingh Onnes

Superconductivity was observed for the first time by a Dutch physicist Heike Kamerlingh Onnes, a professor of physics at the University of Leiden. He successfully liquefied Helium in 1908 and was subsequently able to reduce the temperature of liquid helium (LHe) down to as low as 0.9 K. He had intended to measure the resistivity of metals as a function of

temperature at very low temperatures. By measuring the resistivity of mercury (Hg), as a high purity metal, he found in 1911 that the electrical resistivity of Mercury abruptly dropped to zero, when the sample was cooled below 4.2 K as shown in *figure 1.1* [1]. Onnes realized that the new phenomenon represented a new physical state and termed it the **superconductive state**. Thereafter, the phenomenon of vanishing of electrical resistivity of materials below a particular low temperature is called **superconductivity** and the materials which exhibit this property are called **superconductors**. The temperature at which the transition from the normal state to the superconducting state occurs is called the **critical temperature** (T_C). In 1913, he won Nobel Prize in Physics for his research in this field.

After twenty years of the discovery of Onnes, a major breakthrough came in 1933 when Walther Meissner and his student Robert Ochsenfeld discovered an important magnetic property of superconductors. They observed that a magnetic field lower than **critical field** (H_C) was suddenly expelled by superconductor specimens on cooling below T_C [2]. In other words, the material becomes fully diamagnetic in the superconducting state. This is called the **Meissner effect** and was found to be an intrinsic property of superconductors. It has been widely used for testing the superconducting state. In the superconducting state, an electric current is produced near the surface of sample, in such a way as to create a magnetic field that exactly cancels the external magnetic field.

The superconducting state of a material is decided by three parameters such as temperature, external magnetic field and the current density flowing through the material. These three parameters are coupled together to define the superconducting limits of a material as shown in *figure 1.2* which shows that for the occurrence of superconductivity in a material, the temperature must be below the **critical temperature** (T_C), the external magnetic field must be below the **critical field** (H_C) and the current density flowing through the material must be below the **critical current density** (J_C). These define a critical surface as illustrated in *figure 1.2*, beneath the surface the material is in superconducting state and above the surface the material is in normal state.

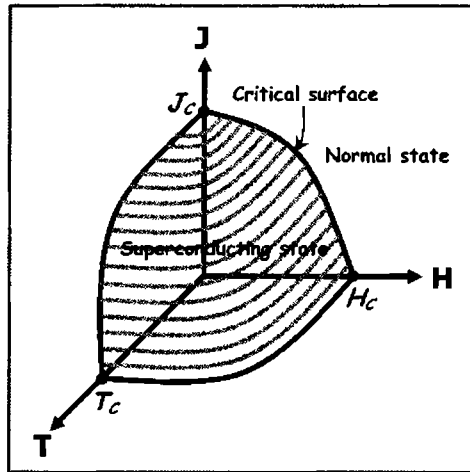


Figure 1.2: Schematic diagram of superconducting domain governed by the critical parameters T_c , J_c and H_c

In 1935, Fritz and Heinz London theoretically explained the Meissner effect by postulating two groups of electrons in a superconducting material, the superconducting electrons and the normal state electrons. They employed the Maxwell's equations to develop a set of electrodynamic equations, called the *London equations* [3, 4]. According to the London equations, the magnetic field exponentially falls off with increasing distance from the surface of a superconducting sample. This characteristic decay length is called the *London penetration depth* (λ). In 1950, V. Ginzburg and L. Landau developed a theoretical explanation for superconductors based on general symmetry properties [5, 6]. Although the *Ginzburg-Landau theory* explained the macroscopic properties of superconductors, the microscopic properties remained unsolved.

Seven years later, three physicists at the University of Illinois, John Bardeen, Leon Cooper and Robert Schrieffer presented a theoretical explanation for the superconducting state [7]. This theory was widely accepted and is well known as the *BCS theory*. Based on this theory, despite the Coulomb repulsive forces between the electrons, due to distortion in the crystal structure (phonon mediation), slight attraction between pairs of electrons located near the Fermi surface leads to the production of bonded

pairs of electrons, called *cooper pairs* [8]. *Coherence length* (ξ) gives approximate spatial dimension of the cooper pair and it sets the length scale on which the superconducting order parameter changes considerably. The BCS theory explained superconductivity in the low temperature and low magnetic field regime. Soon after that, the theory was extended and became useful for high magnetic fields as well [9].

Alexei Alekseevich Abrikosov theoretically investigated the properties of superconductors in external magnetic fields and the way in which magnetic flux can penetrate a superconductor. In 1957 he discovered that superconducting materials can be separated into two groups *type-I* and *type-II superconductors* [10, 11]. Type I superconductors show abrupt transition from superconducting meissner state to normal state above a particular external field which is its *critical field* (H_C), whereas for type-II superconductors there are two critical fields, the *lower critical field* (H_{C1}) and the *upper critical field* (H_{C2}). If the external magnetic field is lower than H_{C1} , the field is completely expelled and the material behaves the same as a type-I superconductor. By increasing the field above H_{C1} up to H_{C2} , the flux partially penetrates into the superconductor as *vortices*. As the field increases above H_{C2} the flux totally penetrates the whole sample, and it returns to the normal state.

In 1962 Brian D. Josephson, a 22 year old British student at Cambridge University, predicted that electric current could flow between two superconducting materials separated by a thin (a few nano meter thick) insulating layer or weak link via a tunneling process [12]. Later, his prediction was experimentally confirmed and became known as the *Josephson effect*. A significant breakthrough then was made in 1986 by George Bednorz and Alex Müller, when they made a ceramic superconductor LaBaCuO with a critical temperature of 30 K [13]. Subsequently, by substitution of yttrium for lanthanum another ceramic superconductor with a critical temperature of 92 K was discovered [14]. Since the critical temperature of the material was considerably higher, it facilitated the use of liquid nitrogen, a cheaper refrigerant.

1.2 Basic characteristics of the superconducting state

Two fundamentally important and intuitively startling properties are associated with superconductivity:

- The transition from finite resistivity, ρ_n in the normal state above a superconducting critical temperature T_C , to $\rho = 0$, i.e. perfect *dc* conductivity below T_C
- The simultaneous change of magnetic susceptibility χ from a small positive paramagnetic value above T_C to $\chi = -1$, i.e. perfect diamagnetism below T_C

The phase transition of a material from its normal state to superconducting state is a second order phase transition which includes the onset of electron pairing and long range phase coherence. This occurs at different temperatures for different compounds, which is often referred as the critical temperature. Though BCS theory provides a formula for estimating T_C , it does not account the specifics of the material considered. In short, till date there is no rule for the prediction of critical temperature of a particular material. The T_C of a superconductor is a macroscopic quantity below which the formation of cooper pair (a two electron coupled boson) occurs, a strictly quantum phenomenon existing both in momentum and real space. In the quantum world, every particle is characterized by a wave function and similar is the case with the cooper pair condensate. It is defined by a wave function $\Psi(r_1-r_2)$, called the **order parameter**, where r_1 and r_2 are the positions of each electron in real space. Both the net spin and net momentum of a cooper pair is zero. The order parameter is a complex scalar which is continuous in real space and has certain properties as stated below:

- ★ It is a single-valued function i.e. at any point $\Psi^*(\mathbf{r})\Psi(\mathbf{r})$ can only have one value where $\Psi^*(\mathbf{r})$ is the complex conjugate of $\Psi(\mathbf{r})$.
- ★ In the absence of magnetic field, $\Psi \neq 0$ at $T < T_C$; and $\Psi = 0$ at $T \geq T_C$.
- ★ $\Psi = 0$ outside a superconductor.
- ★ The order parameter is usually normalized such that $|\Psi(\mathbf{r})|^2$ gives the number density of cooper pairs at a point \mathbf{r} : $|\Psi(\mathbf{r})|^2 = \Psi^*(\mathbf{r})\Psi(\mathbf{r}) = n_s$, where n_s is the number of superconducting electrons and $n_s = n - n_n$,

where n is the total number of free electrons, and n_n is the number of non-superconducting electrons. Then, in a conventional superconductor, $\Psi(\mathbf{r}) = (n_s)^{1/2} e^{i\theta}$.

- ★ In momentum space, the variations of $|\Psi|$ are proportional to variations of the energy gap.

The knowledge of order parameter provides lots of indirect information regarding the superconducting mechanism. The symmetry of the order parameter gives an idea of the attractive force that binds the two electrons in a cooper pair together. For conventional superconductors, the angular momentum is zero and in turn the energy gap has no nodes, but bears a constant positive/negative value throughout the momentum space. Since energy gap is constant, Ψ also should be constant which demands s wave symmetry for conventional superconductors. The s wave symmetry gives a considerable likelihood for the involvement of lattice interaction in the formation of cooper pairs. While in the case of unconventional superconductors, though the net spin and momentum are zero, the angular momentum need not be zero. When the angular momentum is 2, the order parameter is said to have d wave symmetry with an energy gap having two positive and two negative lobes and four nodes between the lobes. For certain unconventional superconductors, the electrons form a triplet state where the angular momentum is 1. Thus, the order parameter has p wave symmetry. Both the p and d wave symmetries point towards a spin fluctuation mediated superconductivity.

In a spatially varying magnetic field or near a superconductor-normal metal boundary, the order parameter varies within a characteristic scale, termed as the coherence length. Though coherence length is often defined as the distance between two electrons in a cooper pair, it is true only for conventional superconductors at a temperature $T = 0$. Here the phase coherence is mediated by the overlap of cooper pair wave functions, also called as Josephson coupling. Moreover, both electron pairing and phase coherence occur simultaneously at T_c . However, in unconventional superconductors the phase coherence is not mediated by Josephson coupling and hence the coherence length and the cooper pair size are not equal.

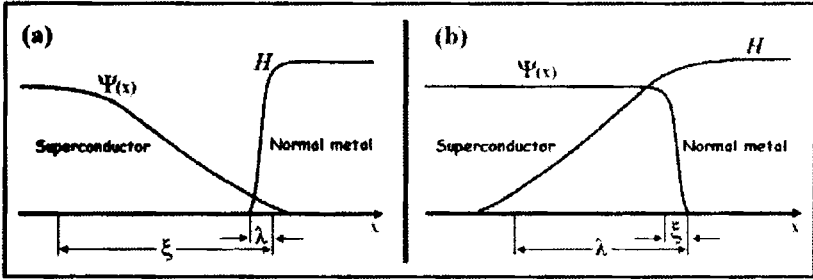


Figure 1.3: Spatial variations of the order parameter $\Psi(x)$ and the magnetic field H near a superconductor-normal metal interface for (a) $K < 1/\sqrt{2}$ and (b) $K > 1/\sqrt{2}$

The order parameter and the coherence length of a superconducting material has a finite value below T_C which does not vanish abruptly i.e. the superconducting region gradually diminishes into the normal one. But the presence of an applied magnetic field can change this scenario. Though we say that a superconductor expels magnetic field below T_C actually the applied field does penetrate to an extent. But the so called Meissner effect is displayed by establishing a persistent super current on its surface that exactly cancels the applied field. The thickness of the layer through which super current flows is called the penetration depth. The ratio of penetration depth to coherence length is an important parameter that characterizes the superconducting material and is approximately independent of temperature. It is a dimensionless material constant, called as the Ginzburg-Landau parameter, K . The value of K can be defined from the surface energy between the normal and superconducting phases. For the conventional superconductors, it yields very small values i.e. $K < 1/\sqrt{2}$ and are now known as *type I superconductors*. But for certain materials, the dependence of critical field on the thickness or temperature did not fit the predictions of Ginzburg-Landau theory. Abrikosov checked whether $K > 1/\sqrt{2}$ can be true as it suggests a negative surface energy between the normal and superconducting states which calls for the existence of a special kind of intermediate state [15]. His calculations led to the conclusion that $K > 1/\sqrt{2}$ is possible and such superconductors have second order transition for any thickness. This category of superconductors was later called as *type II superconductors*. The spatial variations of the order parameter $\Psi(x)$ and the

magnetic field in the vicinity of a superconductor-normal metal interface on the basis of K are shown in *figure 1.3*.

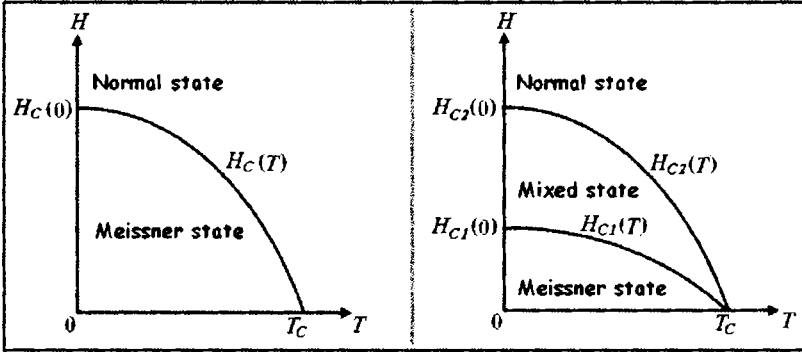


Figure 1.4: Phase diagram on the magnetic field versus temperature for (a) type I and (b) type II superconductor

Though Abrikosov distinguished the two types on the basis of K , the main difference is that they show entirely different response to an external field. While type I expels magnetic flux completely from its interior, type II does it completely only at small magnetic fields but partially at higher fields. The variation of the critical field with temperature for a type I superconductor is approximately parabolic as shown in *figure 1.4*. For a type II superconductor, there are two critical fields, the lower critical field H_{C1} and the upper critical field H_{C2} . In applied fields less than H_{C1} , the superconductor completely expels the field, just as a type I superconductor does below H_C . At fields just above H_{C1} , flux, however, begins to penetrate the superconductor in microscopic filaments called *vortices* which form a regular (triangular) lattice as shown in *figure 1.5*. Each vortex consists of a normal core in which the magnetic field is large, surrounded by a superconducting region, and can be approximated by a long cylinder with its axis parallel to the external magnetic field. Inside the cylinder, the superconducting order parameter Ψ is zero. The radius of the cylinder is of the order of the coherence length, ξ . The super current circulates around the vortex within an area of radius λ , the penetration depth. The vortex state of a superconductor was discovered experimentally by Shubnikov and theoretically explained by Abrikosov and is known as the *mixed state or intermediate state*. It exists for applied fields between H_{C1} and H_{C2} . At H_{C2} ,

the superconductor becomes normal, and the field penetrates completely. Depending on the geometry of a superconducting sample and the direction of an applied field, the surface sheath of the superconductor may persist to even higher critical field, which is approximately $1.7H_{C2}$.

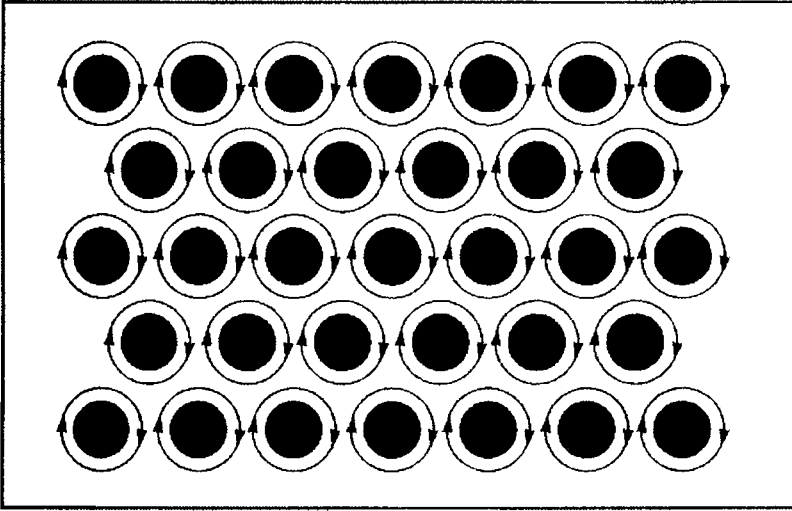


Figure 1.5: Normal state vortices (grey areas) in the mixed state of a type II superconductor form a regular triangular lattice. Arrows shows the super current circulating around the vortices at λ from the centers of vortices. The radius of each vortex is ξ .

The Ginzburg-Landau theory predicts that $H_C(T)\lambda(T)\xi(T) = \Phi_0/(2\sqrt{2}\pi\mu_0)$ where $\Phi_0 = h/2e = 2.0679 \times 10^{-15}$ Wb, is the magnetic flux quantum. In the framework of the Ginzburg-Landau theory, $H_{C2} = \sqrt{2}KH_C$, where $K = \lambda\xi$, is the Ginzburg-Landau parameter. Then, substituting this expression, we obtain $\Phi_0 = 2\pi\xi^2H_{C2}$. This important relation is often used to obtain the values of the coherence length in type II superconductors.

The superconducting state can be destroyed not only by a magnetic field but by a *dc* electrical current as well. The critical current is the maximum current that a superconductor can support. When a type II superconductor in the mixed state is allowed to transport a current from an external source in the direction perpendicular to the vortices, a Lorentz force is acted upon the vortices. In a homogenous superconductor without defects, this Lorentz force sets the vortices into motion which is

accompanied by dissipation of energy. The critical current of such an ideal superconductor becomes zero. Whereas, in an inhomogeneous superconductor containing various types of defects like grain boundaries, dislocations, voids or second phase precipitates, the vortices get pinned by the defects which are known as pinning centers. A finite transport current J is then required to set them moving, such that the Lorentz force produced is enough to tear the vortices off the defects. If the Lorentz force per unit length of a vortex is $f_L = J\Phi_0$, then Lorentz force per unit volume is $F_L = J \times B$. When the vortices are at rest, the Lorentz force is balanced by the pinning forces exerted on the vortices. If the average density of the pinning force per unit volume is denoted by F_p , then critical current density must satisfy the equation, $F_p = J_C \times H$. For F_p independent of the external field, the critical current density is $J_C \propto H^l$. It should be noted that all defects cannot interact with the vortices effectively. If the structural defects have sizes which exceed far from the size of a vortex (ξ), then the vortices will not be pinned. Conversely, structural defects having sizes comparable to coherence length are effective in flux pinning and can cause increase in J_C . The maximum current density that can theoretically be sustained in a superconductor is of the order of H_c/λ .

1.3 Superconducting materials

The first element to display superconductivity is mercury following which many materials including metals, alloys, intermetallics, amorphous compounds, organic materials, oxides, cuprates, doped fullerenes, chalcogenides and pnictides turned out to be superconductors at critical temperatures ranging from a few mK to 164 K [16-18]. Superconductors are proven to be highly varied in composition but elusive and mysterious. It is quite interesting that certain noble materials like Cu, Ag, and Au which are famous as good conductors never showed superconductivity to the lowest attainable temperatures. But at the same time materials which are highly insulating at room temperatures are good superconductors at low temperatures. Since superconducting materials are well known for their diamagnetic behavior, compounds containing ferromagnetic materials like iron are not supposed to be superconductive, but there are exceptions.

Moreover, non-superconducting materials processed at normal conditions may undergo superconducting transition on applying appropriate pressure, inducing suitable charge carriers or by proper irradiation [19].

Superconducting materials can be categorized in various ways which is schematically represented in *figure 1.6*. The classifications of superconductors are mainly based on their critical temperature, electromagnetic property and the underlying mechanism. Superconductors can be categorized as low temperature superconductors (LTS) if it has $T_c < 77$ K and high temperature superconductors (HTS) if $T_c > 77$ K. Based on the behavior of a superconductor in an external magnetic field, superconductors are classified into two categories type I and type II superconductors. Superconductors that can be explained by BCS theory or their derivatives are called conventional superconductors and those which cannot be explained by BCS theory are called unconventional superconductors. They can also be differentiated on the basis of dimensional structure. Although most superconducting materials are three dimensional, some organic compounds and single walled carbon nanotubes are found to exhibit two and one dimensional superconductivity, respectively.

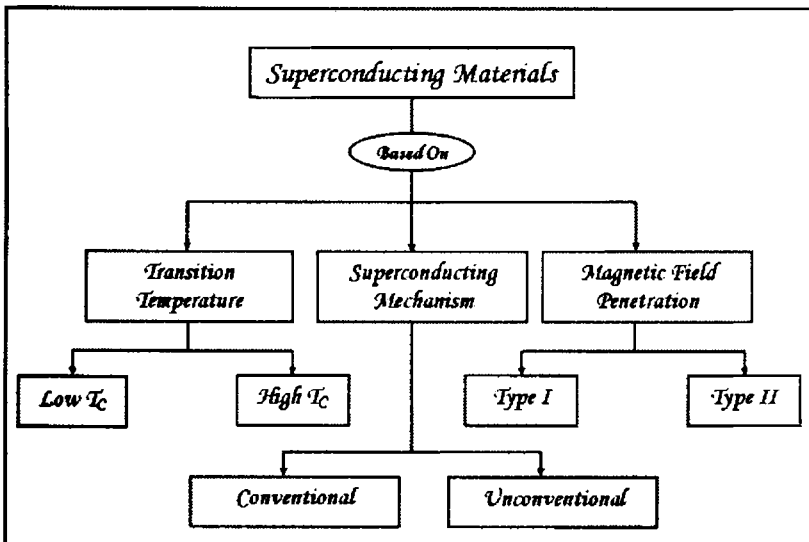


Figure 1.6: Schematic representation of the superconductor classification

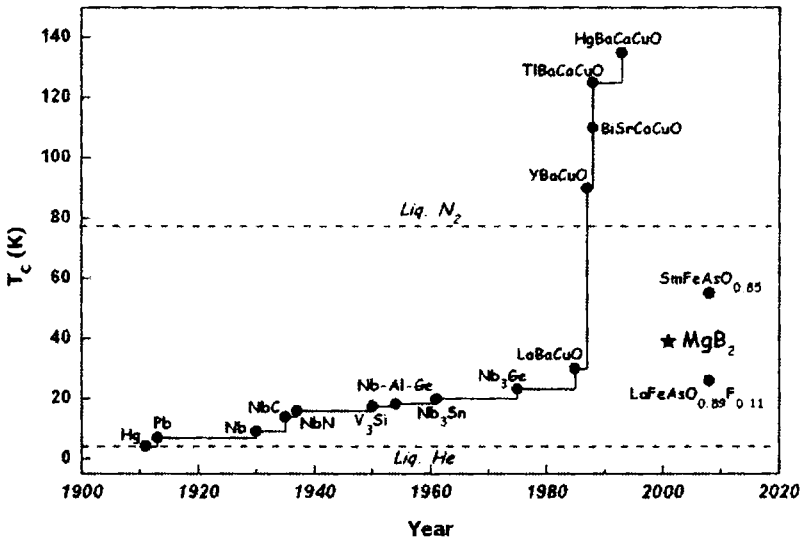


Figure 1.7: Time evolution of superconductors with respective critical temperatures

Based on the type of material, superconductors are classified into various categories as enlisted in *table 1.1*. In subsequent decades after the discovery of superconductivity in Hg, several other materials were found to be superconducting. The time evolution of prominent superconductors with respective critical temperatures is depicted in *figure 1.7*. In 1913, lead was found to superconduct at 7 K, and in 1941 NbN was found to superconduct at 16 K. While most pure metal or pure element superconductors are type I, Niobium, Vanadium, and Technetium are pure element type II superconductors with a T_c of 9.2, 5.4 and 7.7 K respectively. In 1962, the first commercial superconducting wire, an alloy of niobium and titanium (NbTi) was developed. Not much interest existed in the research on A15 compounds until the discovery of superconductivity in V_3Si at 17.5 K in 1953. In the following years several other A_3B superconductors were found. Nb_3Sn was discovered to be a superconductor in 1954 with a T_c of 18.3 K. Nb_3Ge held the record for the highest T_c of 23.2 K from 1971 till the discovery of the cuprates in 1986 [20].

Later heavy fermions showed superconductivity in 1979, where the electronic degrees of freedom are directly linked with magnetic moments of partially filled f-shells of Ce or U atoms [21]. The search for organic

superconductors boosted in the 1960s by the idea that conductive polymer chains with polarizable molecular groups may provide a highly effective cooper pair coupling for electrons and the first discovery of an organic superconductor was in 1980 [22-24]. Fullerenes attracted much attention since their discovery in 1985 as a third modification of elementary carbon. The superconductivity in C_{60} introduced by doping and intercalation of alkali metal atoms drew great attraction, with relatively high T_C 's at normal pressures [25, 26].

Ceramic materials are expected to be insulators, certainly not superconductors. But Bednorz and Muller studied the conductivity of a LaBaCuO ceramic in 1986 which gave a superconducting transition at 30 K and this marked the beginning of a new era in superconductivity [13]. In 1987, Yttrium was substituted for Lanthanum in LaBaCuO molecule and an incredible T_C of 92 K was achieved [14, 27]. Thus, for the first time a material now referred to as YBCO had been found that would superconduct at temperatures above the boiling point of liquid nitrogen. Superconductivity in the BiSrCaCuO system was first reported by the substitution of Bi for La in LaSrCuO with a stoichiometry $Bi_2Sr_2CuO_6$ (known as Bi-2201) having a T_C around 10 K [28]. Later on, Maeda *et al.* increased the T_C in Bi-2201 system by adding Ca to obtain $T_C = 80$ K and 110 K for $Bi_2Sr_2CaCu_2O_8$ (Bi-2212) and $Bi_2Sr_2Ca_2Cu_3O_{10}$ (Bi-2223), respectively [29]. Sheng and Hermann discovered the Tl based high T_C superconductors [30]. The T_C increased by introducing Ca in the TlBaCuO system. Two classes of Tl based systems were reported [31, 32]. One is $Tl_2Ba_2CaCuO_8$ (Tl-2212) of $T_C = 110$ K and the other is $Tl_2Ba_2Ca_2Cu_3O_{10}$ (Tl-2223) where $T_C = 125$ K [33]. The current system of ceramic superconductors with the highest critical temperatures is the mercuric cuprates. The first synthesis of one of these compounds was achieved in 1993. The highest reliable T_C ever measured till date is in the $HgBa_2Ca_2Cu_3O_8$ system ($T_C = 164$ K) under 30 GPa pressure [34]. The discovery of high temperature superconductors started a surge of activity with high hopes to reach materials which would exhibit superconductivity even at room temperatures. The prospect of cooling with cheaper and more practical liquid nitrogen fueled expectations of widespread commercial

applications. Further research on these materials clarified that a Mott insulator with antiferromagnetic ordering can exhibit superconductivity on optimum carrier doping. Many theoretical approaches to the mechanism for the cuprate superconductors have been carried out to understand the mystery of these materials and to predict new high T_C superconductors.

Table 1.1: Superconducting materials under various categories

Type	Example	T_C (K)
Elements	Hg	4.2
	Nb	9.2
	Pd	3.2
	W	5.5
	B	11
Alloys	Li	20
	VTi	7.0
	NbTi	9.0
Amorphous materials	MoTc	16.0
	$U_{85.7}Fe_{14.3}$	1.0
Organic materials	$Th_{80}Co_{20}$	3.8
	(TMTSF)PF ₆	0.9
	kH-ET) ₂ Au(CF ₃) ₄ TCE	10.5
	k-(ET) ₂ Cu[N(CN) ₂]Br	11.8
Magnetic material	(BEDT-TTF) ₂ Cu[N(CN) ₂]Br	0.6
	ErRh ₄ B ₄	10
A15 type	V ₃ Ga	14.0
	V ₃ Si	17.5
	Nb ₃ Sn	18.3
	Nb ₃ Ge	23.2
Laves phase	ZrV ₂	9.6
Chevrel phase	SnMo ₆ S ₈	12.0
	PbMo ₆ S ₈	15.0
Heavy electron systems	UPd ₂ Al ₃	2.0
	CeCu ₂ Si ₃	0.6

Oxides	Ba(PbBi)O_3	13
	$\text{Ba}_{0.6}\text{K}_{0.4}\text{BiO}_3$	30
Cuprates	LiTi_2O_4	13.7
	$\text{LaBa}_2\text{Cu}_3\text{O}_7$	30
	$\text{YBa}_2\text{Cu}_3\text{O}_7$	92
	$\text{Bi}_2\text{Sr}_2\text{Ca}_1\text{Cu}_2\text{O}_8$	80
	$\text{Bi}_2\text{Sr}_2\text{Ca}_2\text{Cu}_3\text{O}_{10}$	110
	$\text{Tl}_2\text{Ba}_2\text{Ca}_2\text{Cu}_3\text{O}_{10}$	125
	$\text{Hg}_2\text{Sr}_2\text{Ca}_2\text{Cu}_3\text{O}_{10}$	135
Doped Fullerenes	$\text{Rb}_{2.7}\text{Tl}_{2.2}\text{C}_{60}$	45
	Cs_3C_{60}	47.4
Borides	ZrB_{12}	5.82
	YRh_4B_4	11.3
Borocarbides	MgB_2	39
	$\text{YPd}_2\text{B}_2\text{C}$	23
Oxypnictides	$\text{LaFeAsO}_{0.89}\text{F}_{0.11}$	26
	$\text{SmFeAsO}_{0.85}$	55

Iron, as a ferromagnet, was believed to be the last element for the realization of superconductivity because of the way ferromagnetism competes against Cooper pair formation. Unexpectedly, in 2006 a new superconductor based on iron, LaFeOP , was discovered by a group at Tokyo Institute of Technology, Japan which has a T_C at 4 K irrespective of hole/electron doping. A large increase in the T_C upto 26 K was then found in $\text{LaFeAsO}_{0.89}\text{F}_{0.11}$ by the same group in 2008 [35]. The T_C of this material was further raised by the scientists in China to 43 K under a pressure of 2 GPa and to 55 K at ambient pressure by replacing La with other rare earth ions of smaller radius, a T_C that is second to the high T_C cuprates [36, 37]. Nevertheless, the high volatility and toxicity of arsenic and the necessity of inert atmosphere along with high processing temperatures demand much more basic research to mould them for technological applications.

Though there are many developments in the superconducting world, MgB_2 is the most recent candidate for superconducting industries looking

for innovation in their products. Borides had been already investigated systematically since the 1950s with an intention to increase T_C . It was expected that the light boron atoms may provide a high characteristic frequency, which will in turn increase T_C according to BCS formula. In the 1990s, the borocarbide superconductors $RENi_2B_2C$ with T_C up to 16.5 K seemed to fulfill this promise partially. The huge surprise came in 2001 with the discovery of superconductivity in MgB_2 , a compound which was well known since the 1950s and which was already commercially available in large quantities since then [38]. Its relatively high values of T_C (39 K), J_C (10^5 - 10^6 A/cm² at 4.2 K and in the self-field) and H_{C2} (15-20 T at 4.2 K) in wire/tape geometry, make it a promising candidate for practical applications. The superconducting properties of MgB_2 differ from those of LTS and HTS in many ways. Besides the relatively high T_C , MgB_2 has a large coherence length, low anisotropy and transparent grain boundaries. MgB_2 offers excellent superconducting properties, without compromising its affordability and robustness, even when made into wires and is the most suited candidate for 20-30 K operation.

1.4 Applications of superconductors

Besides the scientific interest, the search for applications has always been a driving force for superconductor materials science. Superconducting materials are generally looked at from two view points. One is their interest in science, primarily with respect to the mechanism of pairing, whether they can be described by the standard BCS type theory with electron-phonon coupling or whether strong electron correlations are operative. The other interest is the assessment of their usefulness in technology as to whether they have the requisite properties and are capable of being cast into forms suitable for applications. The two properties of superconductors, zero dc resistivity and perfect diamagnetism, can be used to enhance the performance of many devices. In general, applications of superconductor can be divided into small scale and large scale categories. Small scale applications include Josephson devices, Superconducting Quantum Interference Devices (SQUID), microwave devices and resonators. Large scale applications include electric power transmission, superconducting

magnets, magnetic resonance imaging (MRI), energy storage devices, magnetic levitation devices, magnetic confinement in fusion reactors and particle accelerators. The practical applications of conventional superconductors are limited due to the very low operating temperatures. The discovery of high T_C materials extends the feasible applications of superconductors. Small scale applications are expected to be commercialized earlier than large scale applications due to the complexity in fabricating these materials suitable for commercial applications.

The field of electronics holds great promise for practical applications of superconductors. The miniaturization and increased speed of computer chips are limited by the generation of heat and the charging time of capacitors due to the resistance of the interconnecting metal films [39]. The devices based upon the characteristics of a Josephson junction result in more densely packed chips which could transmit information more rapidly by several orders of magnitude. Their low power dissipation makes them useful in high density computer circuits where resistive heating limits the applicability of conventional switches. Superconducting electronics have achieved impressive accomplishments in the field of digital electronics [40]. Logic delays of 13 ps and switching times of 9 ps have been experimentally demonstrated.

Superconducting quantum interference devices have been key elements in the development and commercialization of ultra sensitive electric and magnetic measurement systems. They are of two types: the *dc* SQUID and the *rf* SQUID. The *dc* SQUID, which operates with a *dc* bias current, consists of two Josephson junctions incorporated into a superconducting loop. The maximum *dc* supercurrent, known as the critical current, and the current-voltage (I - V) characteristic of the SQUID oscillate when the magnetic field applied to the device is changed. The oscillations are periodic in the magnetic flux [41]. The *rf* SQUID is based on the *ac* Josephson effect and it utilizes a single Josephson junction. The flux is inductively coupled into the SQUID loop via an input coil and an *rf* coil that is part of a high-Q resonant tank circuit to read out the current changes in the SQUID loop [42]. The *rf* SQUID is less sensitive compared to *dc* SQUID but the former is cheaper and easier to manufacture in smaller

quantities. SQUIDs are widely used to measure the magnetic susceptibility of tiny samples over a wide temperature range. They are also used as highly sensitive voltmeters in Hall Effect and thermoelectric measurements, as ultrasensitive detectors of nuclear magnetic and nuclear quadrupole resonance, and as transducers for gravitational-wave antennas. Another largest area of application is biomagnetism, notably to image magnetic sources in the human brain or heart. In these studies an array of magnetometers or gradiometers is placed close to the subject, both generally being in a magnetically shielded room. The fluctuating magnetic signals recorded by the various channels are analyzed to locate their source. These techniques have been used to pinpoint the origin of focal epilepsy and to determine the function of the brain surrounding a tumor prior to its surgical removal [43].

Superconductors enable the fabrication of high performance RF and microwave devices, due to the low power dissipation, frequency independent penetration depth and the steep transition between the superconducting and the normal state [44]. Related benefits are high stored energies, and hence high unloaded quality factors of resonators, strong miniaturization, and multi-function integration, as well as broad bandwidth and high sensitivity. They are widely used in ultra sensitive detectors for radio astronomy, miniaturized filter banks with extremely sharp bandpass characteristics, dispersive delay lines with high bandwidth delay products, and sensitive RF coils for magnetic resonance receivers. Superconductors are also used in antennas and waveguides. In many applications, it is important to have antennas that are small compared to wavelength of the energy to be transmitted or received. The ohmic losses in the antenna using normal state metals may be large compared to the effective radiation resistance. Superconducting antennas reduce this inherent resistance thereby improving radiation efficiency. The advantage of superconducting electromagnetic waveguides over conventional metal waveguides would be at the higher frequencies. In the case of milli meter sized waveguides, attenuation becomes prohibitive except for applications where the guide length is very short, usually less than a meter.

The application of superconductors in power transmission mainly refers to their attractive feature in transmitting the energy without loss. The superconducting power applications can be divided into two categories: (a) *high field* (> 1 T applications) – generators, motors, fusion, energy storage, etc. (b) *low field* (< 1 T applications) – transmission cables, transformers, fault current limiters (FCL), etc. Superconducting cables can replace the conventional copper/aluminium based cables in electric power transmissions. Cost of the superconducting technology compared to the conventional is the main hurdle in the limited use of superconductors in this sector. Conductors made of BSCCO-2223 are being applied in variety of power transmission and distribution cables [45]. The world's first high temperature superconductor power transmission cable system in a commercial power grid system was energized in New York, USA [46]. Superconductive fault current limiters (SFCL) offer the most ideal performance since they have no impedance in superconductive state [47, 48]. During the short circuit, they quench into normal state as a result of their critical current being surpassed and enter high limiting impedance into the circuit. Only SFCLs can offer a no impedance operation in normal state and a high impedance operation in fault state. Two major types of SFCLs namely shielded and resistive core; the former being characterized by an inductance when the fault occurs while the latter simply enters a resistant in the circuit to limit the fault current. SFCL allows enhancing the reliability of power systems such as coupling of grids and paralleling can be conveniently used with no concern for the increment in fault current level of the system. Superconductive transformers are also having a great role in power industry [49]. They have more current density than conventional ones and less copper losses which makes the power transformation with better efficiency. Another attractive feature of superconductive transformers is their capability to work oil free, capability to work continuously in overload conditions without any lifetime loss because of the ultra cold operating environment, improvement in voltage regulation and possibility to remove the core. Superconducting motors and generators could be made with a weight of about one tenth that of conventional devices for the same output. Superconducting motors are of two types: the hysteresis rotors containing

bulk HTS elements and the reluctance motors with component HTS ferromagnetic rotors, consisting of joined alternating bulk HTS and ferromagnetic plates. Magnetic fields in conventional motors and generators are created by large coils of copper or aluminum wire. HTS wires have much higher current capacities, which means considerably smaller and more powerful motors and generators can be built. In addition, due to the much lower value of electrical resistance in superconductive machines, they have higher efficiencies compared with conventional copper machines. Superconducting generator configurations are being considered for utility applications due to the reduction in size, weight and noise along with the capability of higher current densities in power supply systems.

Right from the discovery, it had been envisioned that superconducting coils with high persistent current might be used to generate strong magnetic fields. Applications related to magnet technology include magnetic energy storage, maglev trains and magnets for MRI and other medical imaging applications. NbTi is the most widely used superconducting material for MRI magnets. In all these cases the superconductor must not only carry a large current with zero resistance under a high magnetic field, but it must be possible to fabricate it in long lengths with high flexibility and a high packing density. The International Thermonuclear Experimental Reactor (ITER) project is engaged in the development of fusion reactor and a large quantity of LTS superconductors is being manufactured for the project. In fusion reactors, the plasma temperature needed for energy production is several million degrees, and high field superconducting magnets are required to confine the plasma. Nb₃Sn and some HTS based inserts were also developed for high field magnets [50]. Due to the increased specific heat of HTS conductors at elevated temperatures, they become less prone to quenching, and therefore, safer operation of fusion reactors is possible, which is the most desirable requirement for the magnets. Moreover, HTS magnets can be easily cooled by conduction cooling methods.

Superconductive magnetic energy storage (SMES) stores energy in the magnetic field of a superconductive coil and offers a high efficiency up to 95 % in the energy storing releasing process. The rapid operation and

high efficiency of this device in converting the energy would play a significant role in improving the system dynamics. SMES could provide the necessary rotating reserve and system damping, as well as suppressing the fluctuations of frequency, voltage and flicker in the power system [51]. In this way, the use of SMES would increase the reliability and stability of the power system and provide an uninterrupted power supply for special load situations.

The perspective for superconducting applications is very attractive; however, all currently available superconductors have certain disadvantages. Hence in order to put superconductors into application, extensive research is needed. The enormously high critical fields $H_{C2} \sim 100$ T of HTS indicate their potential for extremely high field applications. However, HTS vortex physics has turned out to be much more complex which implies strong restrictions for high field and high temperature HTS magnet expectations. Even though HTS based conductors are steadily progressing towards applications, NbTi and Nb₃Sn conductors are still the basis of superconductor wire industry which delivers magnets for MRI systems and high energy physics. The discovery of superconductivity in MgB₂ in early 2001 with $T_C = 39$ K sparked world wide interest to fabricate practically useful conductors for technological applications at temperatures below 30 K. It is a strong competitor for the currently used NbTi and Nb₃Sn conductors because it can be operated around the 20-30 K temperature range, above the range of current use of LTS. In this range the expensive liquid helium can be avoided and liquid hydrogen or cryocooler can be used. Though it has been a decade since the discovery of superconductivity in MgB₂, considerable progress on conductor development will keep MgB₂ based superconductors on the frontiers of research for a long time, in parallel to HTS.

References:

1. H. K. Onnes, *Leiden Commun.* 124, 1226 (1911)
2. W. Meissner and R. Oschenfeld, *Naturwissenschaften* 21, 787 (1933)
3. F. London and H. London, *Proc. Roy. Soc. A* 149, 71 (1935)
4. F. London and H. London, *Physica C* 2, 341 (1935)
5. V. L. Ginzburg and L. D. Landau, *Sov. Phys. JETP* 20, 1064 (1950)
6. V. L. Ginzburg, *Rev. Mod. Phys.* 76, 981 (2004)
7. J. Bardeen, L. N. Cooper, and J. R. Schrieffer, *Phys. Rev.* 108, 1175 (1957)
8. J. Bardeen, L. N. Cooper, and J. R. Shrieffer, *Phys. Rev.* 106, 162 (1957)
9. L. P. Gorkov, *Sov. Phys. JETP* 10, 998 (1960)
10. A. A. Abrikosov, *Sov. Phys. JETP* 5, 1174 (1957)
11. A. A. Abrikosov, *Zh. Eksp. Teor. Fiz.* 32, 1442 (1957)
12. B. D. Josephson, *Phys. Lett.* 1, 251 (1962)
13. G. Bednorz and K. A. Muller, *Z. Phys. B* 64, 189 (1986)
14. M. K. Wu, J. R. Ashburn, C. J. Torng, P. H. Hor, R. L. Meng, L. Gao, Z. J. Huang, Y. Q. Wang and C. W. Chu, *Phys. Rev. Lett.* 58, 908 (1987)
15. A. A. Abrikosov, *Reviews of Modern Physics* 76, 975 (2004)
16. T. H. Geballe, *Science* 293, 223 (2001)
17. P. Phillips, *Nature* 406, 687 (2000)
18. R. Hott, R. Kleiner, T. Wolf and G. Zwicknagl, *Frontiers in Superconducting Materials, Springer-Verlag Berlin Heidelberg* (2005)
19. C. Buzea and K. Robbie, *Supercond. Sci. Technol.* 18, R1 (2005)
20. C. P. Poole, H. A. Farach and R. J. Creswick (Eds.), *Superconductivity, Academic Press, California* (1995)
21. F. Steglich, J. Aarts, C. D. Bredl, W. Lieke, D. Meschede, W. Franz and H. Schäfer, *Phys. Rev. Lett.* 43, 1892 (1979)
22. W. A. Little, *Phys. Rev. A* 134, 1416 (1964).

23. D. Jérôme, A. Mazaud, M. Ribault and K. Bechgaard, *J. Phys. (Paris) Lett.* 41 L95 (1980)
24. G. Saito, H. Yamochi, T. Nakamura, T. Komatsu, M. Nakashima, H. Mori and K. Oshima, *Physica B* 169, 372 (1991)
25. K. Tanigaki, T. W. Ebbesen, S. Saito, J. Mizuki, J. S. Tsai, Y. Kubo and S. Kuroshima, *Nature* 352, 222 (1991)
26. K. Imaeda, J. Krober, H. Inokuchi, Y. Yonchara and K. Ichimura, *Solid State Communications* 99, 479 (1996)
27. Y. L. Page, W. R. Mckinnon, J. M. Tarascon, L. H. Greene, G. Hull and D. M. Hwang, *Phys. Rev. B* 35, 7245 (1987)
28. C. Michel, M. Herrien, M. M. Borel, A. Grandin, F. Deslandes, J. Provost and B. Raveau, *Z. Phys. B. Condens. Matter* 68, 421 (1987)
29. H. Maeda, Y. Tanaka, M. Fukutomi and T. Asano, *Jpn. J. Appl. Phys.* 27, L209 (1988)
30. Z. Z. Sheng and A. M. Hermann, *Nature* 332, 138 (1988)
31. R. M. Hazen, L. W. Finger, R. J. Angel, C. T. Prewitt, N. L. Ross, C. G. Hadidiacos, P. J. Heany, D. R. Veblen, Z. Z. Sheng, A. E. Ali and A. M. Hermann, *Phys. Rev. B* 60, 1657 (1988)
32. M. A. Subramanian, J. C. Calabrese, C. C. Torardi, J. Gopalakrishnan, T. R. Askew, R. B. Flippen, K. J. Morrissey, U. Chowdhry and A. W. Sleight, *Nature* 332, 420 (1988)
33. S. S. P. Parkin, V. Y. Lee, E. M. Engler, A. I. Nazzal, T. C. Huang, G. Gorman, R. Savoy and R. Beyers, *Phys. Rev. Lett.* 60, 2539 (1988)
34. L. Gao, Y. Y. Xue, F. Chen, Q. Xiong, R. L. Meng, D. Ramirez, C. W. Chu, J. H. Eggert and H. K. Mao, *Phys. Rev. B* 50, 4260 (1994)
35. Y. Kamihara, T. Watanabe, M. Hirano and H. Hosono, *J. Am. Chem. Soc.* 130, 3296 (2008)
36. Z. A. Ren, W. LU, J. Yand, W. Yi, X. L. Shen, Z. C. Li, G. C. ChE, X. L. Dong, L. L. Sun, F. Zhou and Z. X. Zhao, *Chin. Phys. Lett.* 25, 2215 (2008)
37. C. Wang, L. Li, S. Chi, Z. Zhu, Z. Ren, Y. Li, Y. Wang, X. Lin, Y. Luo, S. Jiang, X. Xu, G. Cao and Z. A. Xu, *Euro. Phys. Lett.* 83, 67006 (2008)

38. J. Nagamatsu, N. Nakagawa, T. Muranaka, Y. Zenitani and J. Akimitsu, *Nature* 410, 63 (2001)
39. A. W. Stuart and W. P. Francis, *J. Low Temp. Phys.* 105, 1761 (1996)
40. H. Hayakawa, N. Yoshikawa, S. Yorozu and A. Fujimaki, *Proceedings of the IEEE* 92, 1549 (2004)
41. R. L. Fagaly, *Review Of Scientific Instruments* 77, 101101 (2006)
42. J. E. Zimmerman, P. Thiene and J. T. Harding, *J. Appl. Phys.* 41, 1572 (1970)
43. W. Möller, W. G. Kreyling, M. Kohlhäufel, K. Häussinger and J. Heyder, *J. Magn. Magn. Mater.* 225, 218 (2001)
44. M. J. Lancaster, *Passive Microwave Device Applications of High-Temperature Superconductors*, Cambridge: Cambridge University Press, 1997
45. A. P. Malozemoff, J. Maguire, B. Gamble and S. Kalsi, *IEEE Trans. Appl. Supercond.* 11, 778 (2002)
46. www.amscc.com/pdf/HTSC_AN_0109_A4_FINAL.pdf
47. P. J. Lee (Ed.), *Engineering superconductivity*, Wiley-Interscience, John Wiley & Sons, Inc. 391 (2001)
48. T. Yazawa, Y. Eriko, M. Jun, S. Mamoru, K. Toru, N. Shunji, O. Takeshi, S. Yoshihisa and T. Yoshihisa, *IEEE Transaction on Applied Superconductivity* 11, 2511 (2001)
49. B. W. McConnell, *IEEE Transactions on Applied Superconductivity* 10, 716 (2000)
50. H. W. Weijers, U. P. Trociewitz, K. Marken, M. Meinesz, H. Miao and J. Schwartz, *Supercond. Sci. Technol.* 17, 636 (2004)
51. H. J. Kim, K. C. Seong, J. W. Cho, J. H. Bae, K. D. Sim, K. W. Ryu, B. Y. Seok and S. H. Kim, *Cryogenics* 46, 367 (2006)

2.1 Introduction to MgB₂ superconductor

2.1.1 History and background

Magnesium diboride is a binary intermetallic compound, known since early 1950's to the materials science community and is even commercially available. In 1953, Jones *et al.* [1] and Russell *et al.* [2] reported the formation of MgB₂ phase with the interaction of Mg and amorphous B in hydrogen and/or argon atmospheres. Since 1994 there has been much interest in intermetallic superconductors which incorporate light elements, such as boron, due to the discovery of the new class of borocarbides namely RE-TM₂B₂C where RE = Y, Lu, Dy or other rare earths and TM = Ni or Pd. Boron atom has a suitable size and electronic structure for forming direct B-B bonds that can form various kinds of boron networks. Higher dimensionality of networks is formed on increasing the boron content. There are more than 50 boride compounds with different structures reported to be superconductors [3]. However, the most outstanding discovery was the exhibition of superconductivity in B under high pressure with the critical temperature of 11.2 K [4]. All the AlB₂ type borides along with their critical temperatures are listed in the *table 2.1*. Among these diboride compounds, some were discovered before the discovery of superconductivity in MgB₂ and some after. In January 2001, Prof. J. Akimitsu (Aoyama-Gakuin University, Tokyo, Japan) announced the discovery of superconductivity in MgB₂ with a relatively high T_C of 39 K [5]. At the time of its discovery, MgB₂ had the highest critical temperature of any non cuprate superconductor. This discovery stimulated a considerable amount of research and development concerning MgB₂, not only due to its interesting fundamental properties but also due to its potential applications.

Table 2.1: List of diborides with their respective critical temperatures

Formula	T_C (K)
MgB₂	39
NbB₂	0.62
NbB_{2.5}	6.4
Nb_{0.76}B₂	9.2
MoB_{2.5}	8.1
BeB₂	0.79
ZrB₂	5.5
TaB₂	9.5

2.1.2 Why is MgB₂ so special?

The limit of T_C in metallic superconductors had been believed to be ~ 30 K in the framework of the BCS theory. The discovery of unexpectedly high T_C in a simple binary intermetallic compound, MgB₂ triggered enormous interests in superconductivity research. The basic features of MgB₂ that makes it so special are:

- Relatively high T_C
- Weak link free grain boundaries
- Lower anisotropy than HTS
- Larger coherence length ($\xi \sim 5$ nm)
- Presence of two superconducting gaps having values larger than that of Nb (1.5 meV)
- Remarkably low normal state resistivity ($\rho_{42\text{K}} = 0.38 \mu\Omega\text{cm}$)
- High transport current densities, J_C in the range 10^5 - 10^6 A/cm² at 4.2 K
- High upper critical magnetic field H_{C2} in the temperature range from 4.2 to 30 K

- Suitable for low to mid field niche of applications around 20-30 K where cryocooler can be used for cooling
- Low density makes it appropriate for specific lightweight applications
- Low cost and abundant availability of the raw materials
- Much economical conductor fabrication procedure as it does not require expensive sheath materials like Ag for HTS tapes or wires

Table 2.2: List of superconducting parameters of MgB₂

Parameter	Values
Critical temperature	$T_c = 39$ K
Hexagonal lattice parameters	$a = 0.3084$ nm, $c = 0.3524$ nm
Theoretical density	2.63 g/cm ³
Pressure coefficient	$-1.1 - 2$ K/Gpa
Carrier density	$1.7 - 2.8 \times 10^{23}$ holes/cm ³
Isotope effect	$\alpha_T = \alpha_B + \alpha_{Mg} = 0.3 + 0.02$
Resistivity near T_c	$\rho(40K) = 0.4 - 6$ $\mu\Omega$ cm
Resistivity ratio	$\rho(40K)/\rho(300K) = 1 - 27$
Upper critical field	$H_{C2//ab}(0) = 14 - 39$ T, $H_{C2//c}(0) = 2 - 24$ T
Lower critical field	$H_{C1}(0) = 27 - 48$ mT
Coherence lengths	$\xi_{ab}(0) = 3.7 - 12$ nm; $\xi_c(0) = 1.6 - 3.6$ nm
Penetration depths	$\lambda(0) = 85 - 180$ nm
Energy gap	$\Delta(0) = 1.8 - 7.5$ meV

The superconducting properties of MgB₂ resemble those of conventional superconductors rather than of HTS. These properties include isotope effect, a linear T - dependence of the upper critical field with a positive curvature near T_c and a shift to lower temperatures of both $T_{C-onset}$ and $T_{C-offset}$ at increasing magnetic fields as observed in temperature

dependent resistivity measurements. Some of the important superconducting parameters of MgB₂ are enlisted in *table 2.2*.

2.2 Structural and superconducting properties of MgB₂

2.2.1 Crystal and electronic structure

MgB₂ has a hexagonal AlB₂ type crystal structure with a *p6/mmm* space group, which is common among the diborides [3]. The crystal structure is depicted in *figure 2.1*. The boron atoms form graphite like honeycomb network and the Mg atoms are located at the pores of these hexagons. Each Mg atom located at the centre of the hexagon formed by B donates its electron to the B planes; hence the B-B bonding is strongly anisotropic. In the unit cell the atomic positions are (0, 0, 0) for Mg (Weizkoff symbol 1a) and (1/3, 2/3, 1/2) and (2/3, 1/3, 1/2) for B (Weizkoff symbol 2d) atoms [6, 7]. The coordination polyhedra are (B₁₂Mg₆) for Mg and (Mg₆B₃) for B. The lattice parameters are $a = 0.3084$ nm and $c = 0.3524$ nm and the atomic distances are: B-B intralayer = 0.1780 nm, Mg-Mg intralayer = 0.3084 nm, Mg-Mg interlayer = 0.3524 nm and Mg-B interlayer = 0.25 nm [3, 7]. The in-plane B-B distance is almost half that of the inter-plane B-B distance.

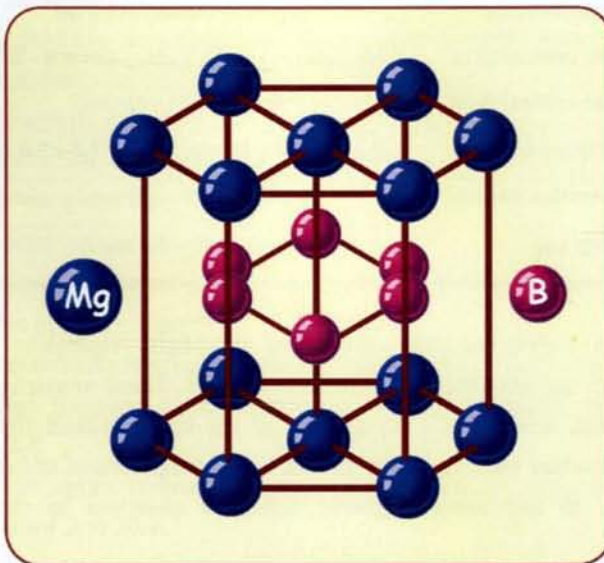


Figure 2.1: Crystal structure of MgB₂

Despite its crystal structure being similar to that of a graphite intercalated compound, MgB₂ has a qualitatively different and uncommon structure of the conducting states. The band structure has been calculated in several studies since the discovery of superconductivity [8-11]. The band structure of MgB₂ is formed by three σ bands (bonding; in-plane sp_xp_y hybridization) and two π bands (bonding and antibonding; p_z hybridization) as shown in *figure 2.2*. The Mg atom donates its valence electrons to the boron planes, forming an ionic bond with the boron atoms. The in-plane boron atoms are held together by strong two dimensional (2D) covalent bonds and three dimensional (3D) metallic bonding existing in between the layers. The 2D covalent σ bands, formed from the sp^2 hybrids of boron 2s and $p_{x,y}$ orbitals, are partially filled. These hole bands are localized on boron planes, while the 3D metallic type π band originates from the boron p_z orbital and is delocalized. The π band contains both electrons and holes as charge carriers [12-14]. Energy of the σ and π bands is nearly the same at the zone centre and there is a chance for charge transfer from σ to π bands [15]. The electronic density of states at the Fermi level and the normal state conductivity has contributions from both the covalent 2D σ band and the metallic 3D π band. The 2D σ band on the boron layer is responsible for the superconductivity.

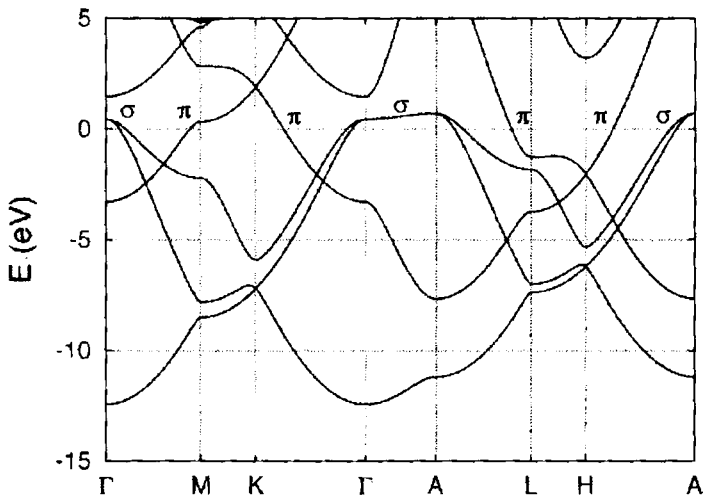


Figure 2.2: Electronic band structure of MgB₂

The valence bands of MgB₂ are formed mainly from the boron $p_{\sigma,x}$ bands and Mg does not contribute much to the band structure. Both the $\sigma_{p_{x,y}}$ and π_{p_z} bands have strong in-plane dispersion due to the large overlap between all p orbitals for neighboring boron atoms [16, 17]. Dispersion of both bands differs considerably. For the $\sigma_{p_{x,y}}$ bands the most pronounced dispersion is observed along Γ -K, while for the π_{p_z} bands it is along Γ -A. The σ bands are degenerate, nearly flat and lie above the Fermi level along Γ -A and constitute two nearly cylindrical hole type Fermi surfaces [16-19] around the Γ -A line. The π bands form two planar honeycomb tubular networks, an antibonding electron type sheet centered at $k_z = 0$ and a bonding hole type sheet centered at $k_z = \pi/c$ [16, 18]. The Fermi surface of MgB₂ is shown in *figure 2.3*. The vertical sections of cylinders are associated with σ bands and the 3D tunnel-like networks are associated with π bands. Green and blue cylinders come from bonding $p_{x,y}$ bands and are hole-like. The blue tubular network (hole type) comes from the bonding p_z bands and the red tubular network is electron-like, from the antibonding p_z band. The last two surfaces touch at the K point.

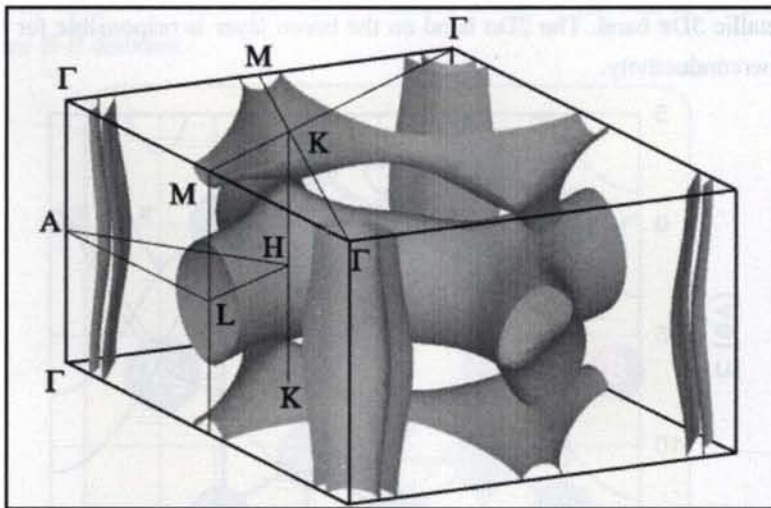


Figure 2.3: The Fermi surface of MgB₂. Green and blue cylinders (hole-like) come from the bonding $p_{x,y}$ bands, the blue tubular network (hole-like) from the bonding p_z bands, and the red (electron-like) tubular network from the antibonding p_z band. The last two surfaces touch at the K point.

The two σ bands and one π band were experimentally observed in the angle resolved photoemission spectroscopic (ARPES) studies [20] and both the ARPES and de Haas-van Alphen effect studies on single crystal MgB₂ samples [20-23] agree reasonably well with the theoretical band structure calculations. The experimentally measured partial density of states (PDOS) of boron by X-ray absorption (XAS) and X-ray emission (XES) spectroscopy show a high PDOS for the boron $\sigma_{p,x,y}$ bands and the observed PDOS agrees well with the band calculations [15, 24, 25]. Measurements of in plane and out of plane Hall coefficients also show dominant hole type carriers along the *ab* plane and electron type carriers along the *c* direction, representing the multiband nature of MgB₂ [26, 27] in transport properties.

2.2.2 Superconducting Mechanism

The basic mechanism for superconductivity is the formation of electron pairs due to the attraction of electrons via the exchange of atomic vibration excitations (phonons) [28-30]. The pairing of electrons is in momentum space rather than in real space. In the BCS theory of superconductivity the expression for critical temperature was derived as $T_C = \Theta \exp(-1/\Lambda_{\text{eff}})$, where $\Theta \sim \Theta_D$ is the Debye temperature of the metal and $\Lambda_{\text{eff}} = \Lambda = N(E_F) \times V$ is the coupling constant between the electrons and phonons. $N(E_F)$ is the electronic level density near the Fermi surface in the normal state and V is the average matrix element of electron interaction which corresponds to the attraction. In the initial BCS theory a weak coupling is assumed between the electrons and phonons and hence the $\Lambda \sim 1$ is assumed to be small [28-30]. The value of T_C according to BCS theory is limited to $T_C \sim 30$ K. As per BCS theory, a material with larger $N(E_F)$, V and Θ_D have higher T_C values. For MgB₂, Θ_D is high but comparable to that of other diborides and light materials. The $N(E_F)$ is relatively low as there are no d electrons present. Thus the observed unusually high T_C in MgB₂, compared to conventional LTS, prompted the researchers to explore the underlying superconducting mechanism.

A lot of theoretical and experimental work has been done to unravel the superconducting mechanism in MgB₂. Superconductivity in MgB₂ differs from other conventional metallic superconductors in many

ways. MgB₂ is the first superconductor to show clearly two distinct superconducting gaps in its superconducting state [31]. At first, many suggested an unconventional exotic superconducting mechanism for the material [32, 33]. Being that holes are the dominant charge carriers in the normal state some suggested hole superconductivity in MgB₂ similar to that in HTS [34, 35]. Majority of the theorists proposed that MgB₂ is a phonon mediated BCS type superconductor, with selective coupling between specific electronic states and specific phonons, the key factor for superconductivity. The unusual high T_C was attributed to the strong anharmonicity of the phonons involved. Being a BCS superconductor the T_C of MgB₂ is influenced by $N(E_F)$, the average energy of the involved phonons and the strength of the coupling between the charge carriers and the phonons. The reduction in $N(E_F)$ decreases T_C of the material.

MgB₂ appears to be the first system for which multiband superconductivity has been identified by several experimental techniques using polycrystalline samples or the single crystals. The strong electron coupling in the 2D bands and weak coupling in the 3D bands lead to existence of two superconducting energy gaps in this material. Besides being a two band superconductor impurity scattering should have a pair breaking effect and thus can decrease the T_C [36]. The charge scattering causes decrease in coherence length and increase in the H_{C2} values. This rule is used for the design and manufacturing of LTS materials over the years. MgB₂ has three scattering channels with different scattering rates: the intra-band scattering within the σ and π bands and the inter-band scattering between the σ and π bands. Tuning of these inter and intra band scattering rates makes it possible to achieve high H_{C2} values in MgB₂, much beyond to the reach of NbTi and Nb₃Sn. Some MgB₂ polycrystals have shown H_{C2} of 40-50 T and the highest H_{C2} of ~ 74 T was reported for a thin film [37].

On the other hand, some reports indicated unconventional superconductivity similar to cuprates, like quadratic T -dependence of the penetration depth and reversal of the hall coefficient near T_C . Moreover, the value of isotopic coefficient of MgB₂ (0.32) is much lower than the expected value (0.5) for BCS superconductor [38]. Nevertheless, majority

of the reports support the BCS mechanism, i.e., an electron-phonon driven *s* wave mechanism of superconductivity in MgB₂.

2.3 Basic superconducting parameters

2.3.1 Critical temperature (T_C)

The superconductivity near 39 K in MgB₂ was completely unexpected compared to other boron based compounds and no other diboride has a T_C comparable to that of MgB₂. Many factors such as material synthesis conditions, crystal structure, crystal defects, strain, chemical composition, doping, external pressure, irradiation by energetic ions and the presence of a magnetic field can affect the T_C of a superconductor in different ways. In MgB₂, T_C is sensitive to boron isotopic substitution while Mg isotopic substitution does not make a significant change in T_C . The large α_B (boron isotopic coefficient) and low α_{Mg} (magnesium isotopic coefficient) clearly show that coupling of B atom vibrations to the electronic structure is responsible for the superconductivity in MgB₂ and the Mg atom vibrations have almost no effect or very little effect on the T_C [39]. For MgB₂, the critical temperature also decreases with pressure up to the highest pressure studied [40-45]. The pressure induced charge variations, changes in phonon modes and changes in the interaction between phonons and charge carriers are the reasons for the observed decrease of T_C under pressure in MgB₂. In the case of MgB₂, there is a significant reduction in T_C upon disordering and irradiation [46, 47]. The T_C of the disordered or strained samples improves on high temperature annealing which heals the disordered and strained regions. For irradiated samples, both reduction in density of states (DOS) and band scattering are the significant factors reducing T_C . The doping studies on MgB₂, with a view to increase its T_C , gave disappointing results so far. In MgB₂, the T_C decreases at different rates for most of the dopants, doped either at Mg or B sites. Dopants such as Al, Li, Si, Zn, Cu, Nb, Mn, Co, Ni, Ag, Sc, Zr, Sn, Ca, Ti, Pb, Au, etc., are tried to substitute at the Mg site and for the B site C is the most tried dopant. Of these studies, Al substitution at the Mg site and C substitution at the B site are the most successful. Many of the other elements do not substitute (or the level of substitution is very low) into the

lattice positions of either Mg or B where doping leads to the formation of finer secondary phase particles, causes significant disorders and distortions in the crystal lattice, which in turn reduces the T_C [48, 49]. However, in strained MgB₂ thin films a slight increase in T_C is observed [50]. The changes in phonon modes and boron σ band contribute to the slight increase in T_C under tensile strains which is equivalent to a negative pressure.

2.3.2 Critical Current Density (J_C)

MgB₂ has high transport current densities at low temperatures. Both the intragrain J_C and intergrain J_C are high for MgB₂. The J_C of MgB₂ depends on many factors such as fabrication technique, heat treatment procedure, microstructure, phase purity and flux pinning. The pristine MgB₂ always shows lower J_C values because of low upper critical field and poor flux pinning. In order to improve $J_C(H)$ properties, a number of experimental techniques, including chemical doping, irradiation, magnetic field annealing, and ball milling methods have been attempted. The grain boundaries act as weak links and hence reduce the intergrain connectivity and J_C in HTS. The misorientation in grain boundaries also affects the J_C of HTS materials like YBCO. But in MgB₂ the grain boundaries are not only transparent to current but also significantly contribute to the flux pinning [51]. MgB₂ is prone to porosity and the density of some of the best samples which showed high J_C is still very much less than the theoretical density (2.55 g/cm³). Porosity reduces the transport J_C in MgB₂ [52]. Processes like hot isostatic pressing (HIP) are to be employed to reduce the porosity and to increase the density. Using nano sized precursors and highly deformed Fe sheaths, Fang *et al.* fabricated highly dense MgB₂ tapes which showed better superconducting properties [53]. The MgO at the grain boundaries acts as weak links and significantly reduces the intergrain J_C which can be avoided using high purity starting powders and oxygen free atmosphere [54]. The nature and toughness of the sheath material and the geometry also play a role in the J_C strain behavior of a superconductor. MgB₂ has relatively high tensile strength and less J_C degradation in applied stress [55]. Stress-strain characteristics of MgB₂ are geometry dependent; wire geometry gives better critical strain than tape [56, 57].

The physics and engineering of vortex dynamics and flux pinning are enormously interesting and constitute an active research field in applied superconductivity. In the case of superconductors placed in magnetic environment with high magnetic permeability, the transport currents can be influenced by the magnetic environment [58]. The only effective way of reducing the flux flow resistance and enhancing J_C is to prevent the motion of vortices by pinning them with defects or with precipitates of non-superconducting phases. The atomic or crystal defects, grain boundaries, voids, point defects, strains, twin planes, inhomogeneities and secondary phases present in any real superconductors are effective pinning sites. The magnetic properties and flux dynamics of MgB₂ are noticeably different as compared with those for the HTS and conventional superconductors. The vortices of MgB₂ are rigid rather than the elastic vortices of HTS [59]. Grain boundary pinning, like in Nb₃Sn, is the dominating pinning mechanism in MgB₂ [51, 60, 61] and the pinning improves with reduced grain size [62]. Besides grain boundary pinning, inclusions and doping can also improve the flux pinning of MgB₂ strongly. The addition of nanometre sized impurities is found to be very effective for the flux pinning of MgB₂ [63, 64]. The addition of nano carbon, nano carbon tubes and nano SiC enhances the pinning at high fields without reducing the T_C much. Irradiation with protons creates modest levels of disorder and improves the J_C in high fields. But the J_C is lower than that of unirradiated samples at low fields [65]. Compared to the various methods attempted to enhance J_C , chemical doping with carbon-containing materials is the most convenient and effective way to enhance the $J_C(H)$ properties of MgB₂. The effects of such additives/dopants have been discussed in *section 2.5*.

2.3.3 Critical Field (H_C)

The critical field is an intrinsic property defined by the (H , T) phase boundary between the superconducting and normal states of a type II superconductor. The upper critical field H_{C2} , lower critical field H_{C1} , and irreversibility field H_{irr} are important parameters to characterize superconductivity. For potential applications, it is essential to have high H_{C2} , as it shows the ability of a superconductor to sustain superconductivity

at high magnetic fields. The introduction of suitable additives in the superconducting matrix or alloying is used to improve the critical field of practical superconductors [66]. Pure MgB₂ has low lower critical field H_{C1} of less than 50 mT [67, 68], upper critical field H_{C2} of 15-20 T and irreversibility field H_{irr} of 6-12 T at 4.2 K [67, 69-71]. This low irreversibility field can cause rapid decrease in J_C at high fields which in turn limits the temperature and field range where MgB₂ could be superior to Nb₃Sn. In order to compete with the Nb₃Sn for liquid helium temperature applications, the $J_C(H)$ of MgB₂ must be improved. For MgB₂ superconductor, defects produced by irradiation can act as strong flux pinners and scattering centers which improve the in-field J_C as well as the H_{C2} [72, 73]. Addition of appropriate impurities or doping can also significantly enhance H_C and J_C . Generally, carbon based dopants like nano C, SiC, B₄C and some hydrocarbons give better J_C and H_{C2} in MgB₂ [74-78]. Significant research is being continued for the improvement of flux pinning and hence $J_C(H)$, H_{irr} and H_{C2} in MgB₂.

For clean single crystal samples, relatively low values of the upper critical fields about $H_{C2//ab}(0) \sim 18$ T and $H_{C2//c}(0) \sim 3.5$ T have been reported parallel and perpendicular to the *ab* plane, respectively [79, 80]. However, the higher value of the upper critical field varies considerably up to about $H_{C2} \sim 29$ T for bulk samples containing impurities [81, 82] and up to about $H_{C2//ab}(0) \sim 48$ T for thin films [83]. Gurevich *et al.* [84] have reported very high upper critical fields, up to 50 T, for MgB₂ thin film with very high resistivity. Such high values of H_{C2} suggest that MgB₂ is a suitable candidate for practical applications.

2.4 Preparation of MgB₂ superconductor

Over the last decade, various preparative methods have been adopted to synthesize MgB₂ based superconductors in bulk, wire/tape, thin film as well as single crystal forms. Mainly MgB₂ superconductors are prepared by either *in situ* (heat treatment of the powder mixture of Mg and B) or *ex situ* (sintering of already reacted MgB₂ powders) methods. The *ex situ* method is reliable for obtaining highly dense and homogeneous core. But, since the filling powder is already reacted, the sinterability is poor and

doping of impurities is not very effective compared to the *in situ* method. For superconducting applications, high quality MgB₂ powder is required. But it is very difficult to obtain phase pure MgB₂ because Mg is extremely volatile and the difference of melting temperature between Mg and B is around 1500 °C. Mg itself is a very reactive element and it oxidizes during powder production and handling. Mg melts at about 650 °C and at temperatures above this both Mg and B are active in forming oxides like MgO and B₂O₃. This insists that the ingredients should be enclosed in Nb/Ta tubes or foils and processed in inert or vacuum conditions.

2.4.1 Bulk samples

MgB₂ superconductor in a bulk form is important for determining basic physical and electrical properties. Although MgB₂ is available from chemical suppliers as commercial powder, the critical properties like current density and upper critical field of this commercial powder are not good enough for practical applications. Different methods of bulk sample preparation are explained below.

2.4.1.1 *In situ* preparation

Several synthesis procedures are reported for the preparation of *in situ* MgB₂ bulks with relatively low temperatures and short durations of heat treatments [85-89]. The starting materials are Mg in powder/flakes/chips and B in amorphous/crystalline powder forms. Precursors of the *in situ* route are mainly mixtures of Mg and B powders with particle sizes as small as available (typically -325 #, <50 μm) with the option of additional ball milling. An alternative approach uses MgH₂ and B [86, 87] with the goal to reduce the oxygen contamination.

MgB₂ can be synthesized simply by the reaction of B with Mg, generally at temperatures above 650 °C which is the melting point of Mg. Till date this method has been used to form MgB₂ powder, sintered pellets, wires and films. The binary phase diagram for Mg-B is shown in *figure 2.4*. MgB₂ is known as a line compound that decomposes above 1500 °C when it is in equilibrium with Mg vapor. As from the phase diagram, the liquid phase of MgB₂ varies from around 650 °C to 1094 °C which also indicates a big variation of processing temperature to form MgB₂. Prolonged liquid

phase reaction is necessary to yield homogenous MgB₂ with better superconducting properties. Yamamoto *et al.* reported that formation of MgB₂ below the melting point of Mg is possible under many hours of processing, which is the solid-solid reaction of Mg and B [90]. GaN and Mg₂Cu have also been used to assist the formation of MgB₂ at relatively lower temperatures via liquid phase sintering [91].

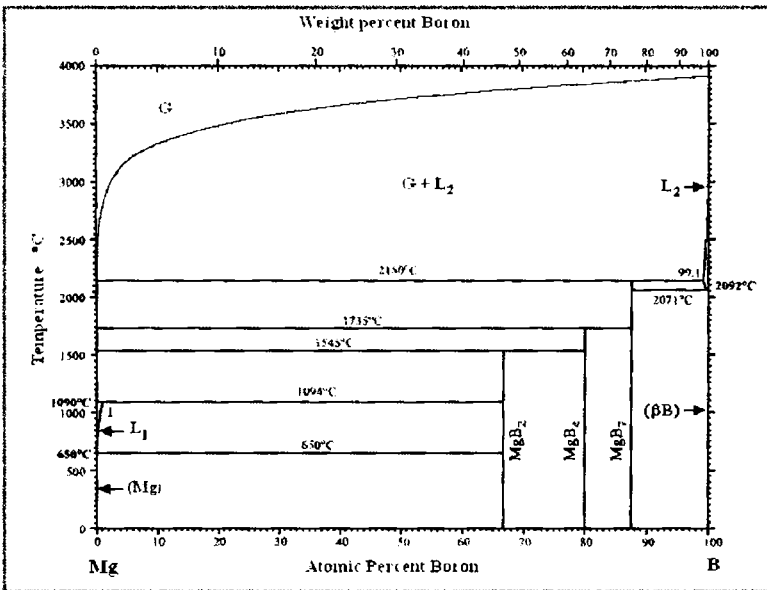


Figure 2.4: Mg – B phase diagram

2.4.1.2 Mechanical alloying

Mechanical alloying is a non equilibrium processing technique to prepare metastable amorphous, quasi crystalline and nanocrystalline materials. The use of mechanical alloying for the preparation of nanocrystalline MgB₂ was shown to be an appropriate technique that yields nanocrystalline structure and refined particle size, thus enhancing flux pinning ability of the grain boundaries. Contamination from the bowl, ball and milling media and particle agglomeration are two main difficulties of this method. The performance of mechanically alloyed or high energy ball milled sample depends on various factors like nature and size of the ball and bowl, ball to powder ratio, speed and milling duration and the milling medium [92, 93]. Starting materials and milling balls are placed together in

a milling vial, which is subjected to a strong vibration or rotational acceleration causing impacts of milling balls leading to repeated fractioning and 'cold-welding' of powder particles. The milling conditions can be adjusted so that the desired phase forms via solid state reaction at moderate temperatures. Normally, the milling process is performed in the Ar atmosphere in a sealed tungsten carbide vial on a planetary ball mill. However, long time of milling will expose the final product to impurities/contamination from the vial. Using mechanically alloyed elemental Mg and B with subsequent hot-pressing has improved the J_C and the irreversibility field substantially. The increment in J_C was ascribed to the large number of grain boundary pinning contributed by nano particles. Meanwhile, mechanical milling on the commercially available MgB₂ powder has led to deterioration of T_C .

2.4.1.3 Powder in sealed tube method (PIST)

High volatility and oxygen affinity of Mg at elevated temperatures inhibit the maximum yield of superconducting properties in MgB₂. Although reasonably dense bulk MgB₂ samples were obtained under hot-pressing of specimen at high pressure and high temperature, the large scale exploitation of MgB₂ as a potential material for various practical applications requires development of more simple and cost effective processing techniques. Generally, the synthesis of MgB₂ is done by enclosing samples in Nb/Ta tubes or foils in inert atmosphere or vacuum. In order to circumvent these problems, a more economical *in situ* method known as 'Powder In Sealed Tube (PIST)' technique was developed and used in the present work. In this method, the ends of the powder filled stainless steel (SS) tubes were pressed and sealed by cold welding so that the samples can be heat treated directly in air (detailed in the next chapter). This can practically eliminate Mg evaporation loss and minimize oxidation of Mg and reduce the cost of synthesis by avoiding expensive Nb/Ta tubes or foils, inert gases and special furnaces.

2.4.1.4 Hot Isostatic Pressing (HIP)

HIP process for MgB₂ is promising as it can produce highly dense, low porosity and crack free samples which allow improvement of

mechanical properties of MgB₂. Most of the *in situ* samples prepared by other methods have porosity and low density (only 50% of theoretical density in many cases). Methods like double step sintering [94, 95], high pressure sintering (HPS) [67, 96, 97] and hot isostatic pressing (HIP) [98, 99] are used to get highly dense MgB₂ bulk samples. Both high pressure sintering and hot isostatic pressing use high pressure for the densification and reduction of porosity. In these methods, the precursor is subjected to high pressures of 0.5-5 GPa during the high temperature heat treatment at 700-1000 °C. The reported properties after HPS or HIP synthesis show some scatter with respect to the pressing system. The main advantage of this technique is the possibility of producing extremely high dense MgB₂ samples with density even close to 100 %. The main disadvantage is the requirement of sophisticated and costly instruments, which also limit the sample dimensions. Though the method is most suitable for bulk samples, some groups used it for making small length wire/tapes with limited success.

2.4.2 Wire/tape samples

Development of superconducting wires and tapes with uniform and high current density are essential for the applications in the cable and magnet industries. Over 50 years of conductor fabrication in LTS and 20 years of experience in HTS helped researchers to fabricate MgB₂ conductors of long length soon after the announcement of superconductivity in the material. The first wire was produced by Canfield *et al.* by diffusing Mg vapor into B fibers with a tungsten wire core [70]. One of the big advantages of the fabrication of MgB₂ conductors compared to the other superconducting conductors is that the MgB₂ phase forms at lower temperatures. Moreover, high grain connectivity and better superconducting properties can be achieved with heat treatment in short durations. Since MgB₂ is mechanically hard and brittle, it is impossible to draw it directly into a fine wire. Nevertheless, some of the fabrication techniques used for HTS can be applied to MgB₂. Diffusion of Mg into B fibers or wires, coating technique and Powder In Tube (PIT) method are used for the

fabrication of MgB₂ based conductors. Of these, PIT is the most popular and industrially preferred method.

2.4.2.1 Diffusion method

Mg diffusion into B wires is a relatively easy method by which commercially available B fibers or wires can be converted into superconducting MgB₂ wires. The first superconducting MgB₂ wires were prepared by this method [70]. The fibers obtained were highly dense and showed low normal state resistivity. Cunningham *et al.* [100] also prepared MgB₂ wires by diffusing Mg into tungsten cored B fibers. By infiltrating a preform of B fibers with liquid Mg and subsequent reaction at elevated temperatures, DeFouw *et al.* [101] fabricated composite MgB₂ wires of several hundred continuous fibers within an Mg matrix. The phase homogeneity of the conductors produced by diffusion is poor and the method is suitable for only short samples.

2.4.2.2 Coating techniques

The coated conductor technique is a well known process, widely used for the fabrication of commercially available YBCO conductors. For MgB₂ high H_{C2} and J_C values in applied fields are observed in thin films [102, 103] and so the coated conductor technique is being tried in some labs. Though coated conductors are not commonly used for magnet windings, it is possible to make small magnets with them [104]. Komori *et al.* [105] used a sputtering technique to make MgB₂ coated conductor in Hastelloy substrate with yttria stabilized zirconia as the buffer layer. The MgB₂ thus coated was composed of very fine grains with size less than 10 nm and showed higher J_C in high magnetic fields, compared to the PIT MgB₂ and the conventional NbTi superconductors. The carbon alloyed MgB₂ coated conductor fabricated by hybrid physical chemical vapor deposition on SiC fibers with a tungsten core by Ferrando *et al.*, showed high H_{C2} and high irreversibility field. Even though the superconducting properties of coated conductors are normally superior to those of conductors fabricated by other techniques, the scaling up of this technique is not straightforward compared to the widely used PIT process.

2.4.2.3 Powder in tube method (PIT)

The *in situ* PIT method is generally preferred, which gives good intergranular connectivity and makes it easier to introduce the superconductor with ternary elements to implement artificial pinning centers. The transport properties of PIT processed MgB₂ conductor are strongly dependent on factors such as the raw materials quality, fabrication procedure, heat treatment condition and the reactivity of the sheath material. In PIT, the stoichiometrically weighed and uniformly mixed precursor powder is filled in various metal tubes, compacted mechanically and end sealed by arc welding. These tubes are then drawn or rolled into wires or tapes followed by a heat treatment in vacuum or inert atmosphere [106-111]. In the case of MgB₂, the metallic sheath chosen must be chemically compatible with MgB₂ at elevated temperatures and should not degrade the superconductivity. The sheath metal must have adequate strength to give mechanical support to the brittle superconducting core, but also must be ductile enough to withstand the mechanical working. Fabrication of PIT MgB₂ wires/tapes have been attempted with different sheath materials such as Fe, Ni, Cu, Ag, Nb, Ta and their alloys [112-121].

2.4.3 Thin film

Superconducting films are important for electronics applications such as Josephson junctions and SQUIDs. Many groups have attempted to prepare MgB₂ thin films. However, the high sensitivity of Mg to oxidation, the high volatility of Mg and the large difference between the vapor pressures of Mg and B are the main obstacles to the preparation of superconducting MgB₂ films. MgB₂ thin films have been prepared using different techniques among which pulsed laser deposition seems to be the most common method. High quality films have been prepared using a one step preparation (*in situ*) or a two step preparation (*ex situ*) technique. *Ex situ* technique consists of deposition of amorphous B precursors on substrates, then heating the film in a rich Mg vapor. This method has been widely used and has been quite successful in growing high quality films [122-124]. Each method has its own benefit and drawback. The two step method gives crystalline films with better superconducting properties, but

cannot be used to fabricate Josephson junction or multi layer films. On the other hand, although the *in situ* method gives films with poor crystallinity and lower T_C , this method is applicable for multilayer fabrication. The one step method gives films with a smoother surface than films made via the two step method, but in general, MgB₂ films have a rough surface morphology compared to YBCO thin films. Therefore, methods need to be improved to prepare films suitable for electronic device applications. Zeng *et al.* [125] reported *in situ* growth of high quality MgB₂ thin films by using hybrid physical chemical vapor deposition. This is expected to be a very promising growth technique in terms of applications for superconducting electronics.

2.4.4 Single crystal

In order to tailor the intrinsic properties of a superconductor especially the anisotropic properties, the formation of single crystal is highly essential. Many groups have attempted to grow single crystals after the discovery of MgB₂ superconductor. So far, two different methods have been developed to prepare sub-millimeter MgB₂ single crystal: one is crystal growth by encapsulation and the other is the high pressure method. However, the formation of MgO phase, the high reactivity of Mg in the vapor and melt phases with containers and flux materials, the low solubility of MgB₂ in Mg, the high Mg vapor pressure and the incongruent melting cause difficulties in the crystal growth procedure of MgB₂ [126, 127].

2.5 Chemical doping effects

One of the most important applications of superconductors is in the area of high current and high field, where high J_C in magnetic field is essential. But the main disadvantage of pure MgB₂ is the relatively weak pinning which leads to rapid degradation of J_C in applied magnetic fields. Therefore, the improvement of J_C under magnetic field is essential for the development of MgB₂ for magnetic applications. Different approaches such as irradiation using heavy ions, chemical substitution and nano particle inclusions have been found to be effective for improving superconducting properties of MgB₂ bulks, tapes, wires and films. Among these, chemical doping is the most effective and easy method for modifying the properties

of MgB₂. Doping can cause crystalline and microstructural changes, create lattice defects/disorders and cause formation of non superconducting precipitates or inclusions in the MgB₂ superconducting matrix. All these defects can act as flux pinning centers and can increase the H_{C2} and H_{in} values and hence enhance the in-field J_C of MgB₂. Various nano/submicron particles and materials including metallic elements, carbon based compounds, silicides, nitrides, borides, oxides and some hydrocarbons have been introduced into MgB₂.

Of the several metallic and non metallic elements added into MgB₂, only C and Al enter into the lattice site: C substitutes at the B site and Al substitutes at the Mg site. C substitution at B site alters the σ and π scattering channels and enhances the H_{C2} and $J_C(H)$ of MgB₂. The metals Ti and Zr are reported to have some positive effect on the $J_C(H)$ of MgB₂ [128, 129]. Ti is found to be a good grain refiner in MgB₂, which absorbs the impurities and hence improves the grain connectivity [130]. Similar results of grain refining have been observed with the dopants Ta and CaB₆ [75]. Materials like Mn and Fe are also reported to substitute at Mg site, but only at very low concentrations. Substitutions with such magnetic impurities are found to suppress superconductivity dramatically because of the spin flip pair breaking scattering. In short, most of the metallic dopants reduced the $J_C(H)$ [131].

Among the various dopants tried, carbon doped samples showed an improved field dependence of the J_C compared with the undoped sample over a wide temperature range. Carbon substitution at B site creates lattice strains and distortions which can act as good flux pinning centers. Addition of metal oxides like Al₂O₃, Fe₂O₃, Co₃O₄, ZrO₂, TiO₂ and SiO₂ are found to increase the MgO formation. However, on the extend of $J_C(H)$ improvement by these metal oxide additions, some groups reported decremental effect while some other reported marginal benefits. The addition of silicides such as ZrSi₂, WSi₂ etc. improves the intergrain connectivity, reduces the pores, increases the density of MgB₂, resulting in improved flux pinning and J_C at high fields [129, 132]. The incorporation of rare earth oxides such as Y₂O₃, Dy₂O₃ [133, 134] at the grain boundaries is highly effective in improving the flux pinning strength in MgB₂. The Y₂O₃ addition results in precipitates

of nearly 10 nm size at the grain boundaries and nearly 3-5 nm sized precipitates uniformly distribute in the MgB₂ grains; both of these precipitates contribute to the pinning.

2.6 MgB₂ – Relevance and applications

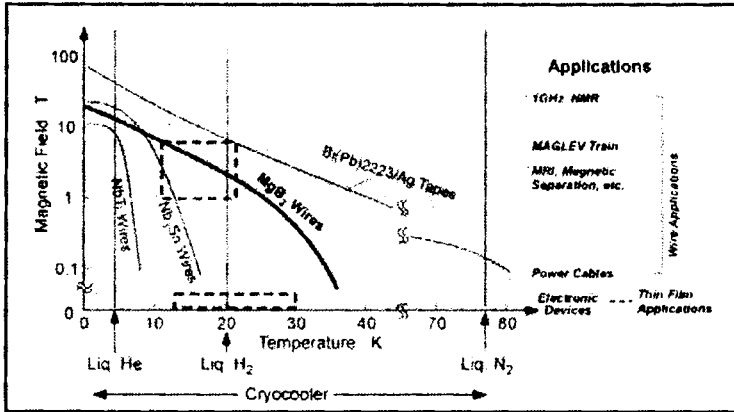


Figure 2.5: Application fields for MgB₂ along with other superconductors

Superconductivity in MgB₂ is one of the most fascinating topics, ranging widely from fundamental aspects to applications. Though there are thousands of superconducting materials, only a few of them are suitable for practical applications. The most widely used commercial superconductors are NbTi and Nb₃Sn, two LTS materials. NbTi, having a T_C of 9 K and H_{C2} (4.2 K) ~ 10-12 T, has high strength and ductility and is easy to fabricate into long wires. NbTi occupies most of the low field magnets in commercial MRI instruments. The use of NbTi is limited to fields <10 T and the operation of NbTi needs liquid helium temperatures, which makes its use costly. Nb₃Sn has a T_C of 18 K and H_{C2} (4.2 K) of more than 20 T and is used in low temperature high field magnets. Though Nb₃Sn offers much higher fields and operating temperatures compared to NbTi; it is brittle, quite sensitive to strains and difficult to fabricate which makes it costlier than NbTi. Another A15 material Nb₃Al with much higher field capacity and strain tolerance than the Nb₃Sn is considered for conductor development. Nb₃Al has a T_C of 20 K and H_{C2} of 40 T at 4.2 K. However, the manufacturing of Nb₃Al conductor with good properties is extremely difficult and it will take few more years to enter into the commercial

market. Most of the HTS materials have T_C above 77 K and higher H_{C2} values than the LTS. But the HTS conductors faced many technical problems in making wires and coils. Their conductor fabrication is not so easy as compared to the LTS materials and needs costly Ag as sheath material and the field performance at higher temperatures is not promising. The most important and commercially interesting HTS are BSCCO (Bi-2223 and Bi-2212) and YBCO (Y-123). Bi-2223 has a T_C of 110 K, Bi-2212 has a T_C of 85 K, and the T_C of YBCO is 92 K. The H_{C2} of all the three HTS is more than 100 T at 4.2 K. Ag sheathed BSCCO conductors known as the first generation HTS conductors are being commercially produced by a number of companies like American Superconductors, Sumitomo Electric Industries Ltd etc. YBCO based coated conductor is considered as the second generation HTS conductors. HTS have high anisotropy and hence the current carrying capacity is low in untextured conductors. Due to their high anisotropy, uniaxial and biaxial texturing are preferred for BSCCO and YBCO respectively. The HTS materials also have weakly connected grain boundaries so that the intergrain connectivity is also a big problem. The recently discovered iron based materials show superconductivity with T_C up to 55 K and H_{C2} values >100 T, however the preparation of quality wires/tapes based on these materials is not successful so far.

Table 2.3: Properties of MgB₂ and other practical superconductors

Material	T_C (K)	Anisotropy	J_c (4.2 K, 0 T) (A/cm ²)	H_{C2} (4.2 K) (T)	$\xi(0)$ (nm)
NbTi	9	-	10^6	11-12	4-5
Nb ₃ Sn	18	-	10^6	25-29	3
Nb ₃ Al	20	-	10^6	30-45	4-5
Bi-2223	110	50-200	10^7	>100	1.5
YBCO	92	5-7	10^6	>100	1.5
MgB₂	39	1.5-5	10^6	30-40	5-12
Fe-Based	26-57	8-15	10^5	>100	2-10

The preparative aspects and superconducting properties of MgB₂ conductors are relevant to technological applications. With a reduced anisotropy compared to the HTS, MgB₂ does not need high texturing and is free from weak links. The grain boundaries are transparent to the supercurrents and act as the main flux pinners in MgB₂. The density of MgB₂ is 2.55 g/cm³, much lower than those of other superconductors and ordinary copper. This makes MgB₂ suitable for specific lightweight applications especially in space applications. Both the reactants of MgB₂ (Mg and B) and the sheath materials used are inexpensive. Thus MgB₂ is much economical for practical applications and the cost/performance ratio for MgB₂ is much lower than those for other superconductors. In contrast to the HTS a variety of sheath materials can be used for MgB₂ with suitable barriers or reinforcing materials, making the conductor design adjustable to specific needs or for specific applications.

MgB₂ can be used in applications around the 20-30 K temperature range, above the range of current use of LTS due to its relatively high T_C . In this range the expensive LHe can be avoided and liquid hydrogen or cryocooler can be used. MgB₂ seems to be the most promising material for high field magnets and a strong competitor for Nb₃Sn and NbTi. Besides the magnet applications, MgB₂ superconductor has potential uses in superconducting transformers, rotors and transmission cables at temperatures around 30 K. The future is positive for MgB₂ superconductors, as there are several ongoing demonstration projects that are directed towards commercial applications.

2.7 Objectives of the present work

Since MgB₂ has the highest T_C of 39 K among metallic superconductors and sufficient chemical stability, it is a prospective candidate for practical applications, such as in superconducting wires and coils, with operating temperature as high as 30 K, which can be easily attained using a cryocooler or liquid hydrogen. Although T_C of MgB₂ is much lower than those of cuprate superconductors developed for practical applications, MgB₂ has many advantages such as strong grain coupling for superconducting current due to large coherence length and high carrier

density, low electromagnetic anisotropy, and simple binary composition without expensive elements. In addition, it should be noted that MgB₂ is free from the nonstoichiometric composition, which results in highly reproducible T_C . These points are quite favorable for the design and development of practical materials, in contrast to other intermetallic compounds and cuprates having cation and/or oxygen nonstoichiometry.

In MgB₂, the fluxoids to be pinned are string like and amenable to pinning by nano particles and precipitates. This opens up a window for chemical doping in this material. Several studies on elemental doping in MgB₂ focused on T_C enhancement but most of them gave negative results. On the other hand, attempts to improve flux pinning, thereby J_C and H_{irr} , via chemical doping gathered momentum. The present work aims at enhancing the superconducting properties especially $J_C(H)$ performance of bulk MgB₂ via substitution or inclusions using suitable nano dopants. The superconducting properties are expected to be enhanced through chemical doping and the possibility of an economic PIT preparation route favor the chances of fabricating MgB₂ wires and coils of desired geometry and property. The thesis addresses the optimization of processing parameters and development of wires, coils and current leads for practical applications. The prime objectives of the thesis are consolidated as follows:

- ☞ Effect of processing temperature and various nano dopants on the properties of bulk MgB₂
- ☞ Optimization of processing parameters and novel preparation techniques for MgB₂ wires
- ☞ Development of MgB₂ multifilamentary wires, coils and current leads for technological applications

References:

1. M. E. Jones and R. E. Marsh, *J. Am. Chem. Soc.* 76, 870 (1953)
2. V. Russell, R. Hirst, F. A. Kanada and A. J. King, *Acta Cryst.* 6, 870 (1953)
3. C. Buzea and T. Yamashita, *Supercond. Sci. Technol.* 14, R115 (2001)
4. M. I. Eremets, V. V. Struzhkin, H. K. Mao and R. J. Hemley, *Science* 293, 272 (2001)
5. J. Nagamatsu, N. Nakagawa, T. Muranaka, Y. Zenitani and J. Akimitsu, *Nature* 410, 63 (2001)
6. D. Tzeli and A. Mavridis, *J. Phys. Chem. A* 109, 10663 (2005)
7. M. E. Jones, and R. E. Marsh, *J. Am. Chem. Soc.* 76, 1434 (1954)
8. R. Zeyer and G. Zwicknagl, *Z. Phys. B* 78, 175 (1990)
9. J. R. Gavaler, *Appl. Phys. Lett.* 23, 480 (1973)
10. R. Hott, *High Temperature Superconductivity, Vol. II Engineering Applications*, (Ed. A. V. Narlikar), Springer Verlag, Berlin (2004)
11. J. G. Lin, C. Y. Huang, Y. Y. Xue, C. W. Chu, X. W. Cao and J. C. Ho, *Phys. Rev. B* 51, 12900 (1995)
12. J. Akimitsu and T. Muranaka, *Physica C* 98, 388 (2003)
13. P. Ravindran, P. Vajeeston, R. Vidya, A. Kjekshus and H. Fjellvag, *Phys. Rev. B* 64, 224509 (2001)
14. K. D. Belashchenko, M. van Schilfgaarde and V. P. Antropov, *Phys. Rev. B* 64, 092503 (2001)
15. E. Z. Kurmaev *et al.*, *Phys. Rev. B* 65, 134509 (2002)
16. I. I. Mazin and V. P. Antropov, *Physica C* 385, 49 (2003)
17. N. I. Medvedeva, A. L. Ivanovskii, J. E. Medvedeva and A. J. Freeman, *Phys. Rev. B* 64, 020502 (2001)
18. L. Ivanovskii, *Phys. Solid State* 45, 1829 (2003)
19. N. Kato, H. Nagao, K. Nishikawa, K. Nishidate and K. Endo, *Int. J. Quantum Chem.* 96, 457 (2004)

20. H. Uchiyama, K. M. Shen, S. Lee, A. Damascelli, D. H. Lu, D. L. Feng, Z. X. Shen and S. Tajima, *Phys. Rev. Lett.* **88**, 157002 (2002)
21. E. A. Yelland, J. R. Cooper, A. Carrington, N. E. Hussey, P. J. Meeson, S. Lee, A. Yamamoto and S. Tajima, *Phys. Rev. Lett.* **88**, 217002 (2002)
22. J. R. Cooper, A. Carrington, P. J. Meeson, E. A. Yelland, N. E. Hussey, L. Balicas, S. Tajima, S. Lee, S. M. Kazakov and J. Karpinski, *Physica C* **385**, 75 (2003)
23. A. Goldoni, R. Larciprete, S. Lizzit, S. La Rosa, A. Bianco and M. Bertolo, *Phys. Rev. B* **66**, 132503 (2002)
24. T. A. Callcott, L. Lin, G. T. Woods, G. P. Zhang, J. R. Thompson, M. Paranthaman and D. L. Ederer, *Phys. Rev. B* **64**, 132504 (2001)
25. J. Nakamura, N. Yamada, K. Kuroki, T. A. Callcott, D. L. Ederer, J. D. Denlinger and R. C. C. Perera, *Phys. Rev. B* **64**, 174504 (2001)
26. Y. Eltsev, K. Nakao, S. Lee, T. Masui, N. Chikumoto, S. Tajima, N. Koshizuka and M. Murakami, *Phys. Rev. B* **66**, 180504 (2002)
27. T. Masui, S. Lee and S. Tajima, *Phys. Rev. B* **70**, 024504 (2004)
28. V. L. Ginzburg, *Rev. Mod. Phys.* **76**, 981 (2004)
29. J. Bardeen, L. N. Cooper and J. R. Schrieffer, *Phys. Rev.* **106**, 162 (1957)
30. J. Bardeen, L. N. Cooper and J. R. Schrieffer, *Phys. Rev.* **108**, 1175 (1957)
31. P. C. Canfield and G. W. Crabtree, *Phys. Today* **56**, 34 (2003)
32. V. A. Ivanov, M. V. Broek and F. M. Peeters, *Solid State Commun.* **120**, 53 (2001)
33. G. Baskaran, *Phys. Rev. B* **65**, 212505 (2002)
34. J. E. Hirsch and F. Marsiglio, *Phys. Rev. B* **64**, 144523 (2001)
35. J. E. Hirsch, *Phys. Lett. A* **282**, 392 (2001)
36. S. C. Erwin and I. I. Mazin, *Phys. Rev. B* **68**, 132505 (2003)
37. V. Braccini *et al.*, *Phys. Rev. B* **71**, 012504 (2005)
38. D. G. Hinks, H. Claus and J. D. Jorgensen, *Nature* **411**, 457 (2001)
39. M. Calandra, M. Lazzeri and F. Mauri, *Physica C* **456**, 38 (2007)

40. M. Monteverde, M. N. Regueiro, N. Rogado, K. A. Regan, M. A. Hayward, T. He, S. M. Loureiro and R. J. Cava, *Science* 292, 75 (2001)
41. E. Saito, T. Takenobu, T. Ito, Y. Iwasa, K. Prassides and T. Arima, *J. Phys.: Condens. Matter* 13, L267 (2001)
42. P. Bordet *et al.*, *Phys. Rev. B* 64, 172502 (2001)
43. B. Lorenz, R. L. Meng and C. W. Chu, *Phys. Rev. B* 64, 012507 (2001)
44. T. Tomita, J. J. Hamlin, J. S. Schilling, D. G. Hinks and J. D. Jorgensen, *Phys. Rev. B* 64, 092505 (2001)
45. V. G. Tissen, M. V. Nefedova, N. N. Kolesnikov and M. P. Kulakov, *Physica C* 363, 194 (2001)
46. R. H. T. Wilke, S. L. Bud'ko, P. C. Canfield, J. Farmer and S. T. Hannahs, *Phys. Rev. B* 73, 134512 (2006)
47. M. Putti, M. Affronte, C. Ferdeghini, P. Manfrinetti, C. Tarantini and E. Lehmann, *Phys. Rev. Lett.* 96, 077003 (2006)
48. C. H. Cheng, Y. Zhao, X. T. Zhu, J. Nowotny, C. C. Sorrell, T. Finlayson and H. Zhang, *Physica C* 386, 588 (2003)
49. D. W. Gu, Y. M. Cai, J. K. F. Yau, Y. G. Cui, T. Wu, G. Q. Yuan, L. J. Shen and X. Jin, *Physica C* 386, 643 (2003)
50. N. Hur, P. A. Sharma, S. Guha, M. Z. Cieplak, D. J. Werder, Y. Horibe, C. H. Chen and S. W. Cheong, *Appl. Phys. Lett.* 79, 4180 (2001)
51. D. C. Larbalestier *et al.*, *Nature* 410, 186 (2001)
52. C. F. Liu, G. Yan, S. J. Du, W. Xi, Y. Feng, P. X. Zhang, X. Z. Wu and L. Zhou, *Physica C* 386, 603 (2003)
53. H. Fang, Y. Y. Xue, Y. X. Zhou, A. Baikalov and K. Salama, *Supercond. Sci. Technol.* 17, L27 (2004)
54. S. Hata, T. Yoshidome, H. Sosiati, Y. Tomokiyo, N. Kuwano, A. Matsumoto, H. Kitaguchi and H. Kumakura, *Supercond. Sci. Technol.* 19, 161 (2006)
55. I. Hušek, P. Kováčik and H. Jones, *Supercond. Sci. Technol.* 17, 1411(2004)

56. K. Salama, Y. X. Zhou, M. Hanna, M. Alessandrini, P. T. Putman and H. Fang, *Supercond. Sci. Technol.* 18, S369 (2005)
57. P. Kováč, T. Melišek, M. Dhall'e, A. denOuden and I. Hušek, *Supercond. Sci. Technol.* 18, 1374 (2005)
58. Y. A. Genenko, A. Snezhko and H. C. Freyhardt, *Phys. Rev. B* 62, 3453 (2000)
59. H. Jin, H. H. Wen, H. P. Yang, Z. Y. Liu, Z. A. Ren, G. C. Che and Z. X. Zhao, *Appl. Phys. Lett.* 83, 2626 (2003)
60. H. Kitaguchi, A. Matsumoto, H. Kumakura, T. Doi, H. Yamamoto, K. Saitoh, H. Sosiati and S. Hata, *Appl. Phys. Lett.* 85, 2842 (2004)
61. X. Y. Song, S. E. Babcock, C. B. Eom, D. C. Larbalestier, K. A. Regan, R. J. Cava, S. L. Bud'ko, P. C. Canfield and D. K. Finnemore, *Supercond. Sci. Technol.* 15, 511 (2002)
62. A. Yamamoto, J. Shimoyama, S. Ueda, Y. Kastura, I. Iwayama, S. Horii and K. Kishio, *Appl. Phys. Lett.* 86, 212502 (2005)
53. S. X. Dou, S. Soltanian, J. Horvat, X. L. Wang, S. H. Zhou, M. Ionescu, H. K. Liu, P. Munroe and M. Tomsic, *Appl. Phys. Lett.* 81, 3419 (2002)
54. J. H. Kim, W. K. Yeoh, M. J. Qin, X. Xu and S. X. Dou, *J. Appl. Phys.* 100, 013908 (2006)
65. Y. Bugoslavsky, L. F. Cohen, G. K. Perkins, M. Polichetti, T. J. Tate, R. Gwilliam and A. D. Caplin, *Nature* 411, 561 (2001)
66. W. A. Fietz and W. W. Webb, *Phys. Rev.* 161, 423 (1967)
67. Y. Takano, H. Takeya, H. Fujii, H. Kumakura, T. Hatano, K. Togano, H. Kito and H. Ihara, *Appl. Phys. Lett.* 78, 2914 (2001)
68. S. L. Li, H. H. Wen, Z. W. Zhao, Y. M. Ni, Z. A. Ren, G. C. Che, H. P. Yang, Z. Y. Liu and Z. X. Zhao, *Phys. Rev. B* 64, 094522 (2001)
69. D. K. Finnemore, J. E. Ostenson, S. L. Bud'ko, G. Lapertot and P. C. Canfield, *Phys. Rev. Lett.* 86, 2420(2001)
70. P. C. Canfield, D. K. Finnemore, S. L. Bud'ko, J. E. Ostenson, G. Lapertot, C. E. Cunningham and C. Petrovic, *Phys. Rev. Lett.* 86, 2423 (2001)

71. S. L. Bud'ko, C. Petrovic, G. Lapertot, C. E. Cunningham, P. C. Canfield, M. H. Jung and A. H. Lacerda, *Phys. Rev. B* 63, 220503 (2001)
72. A. Martinelli, C. Tarantini, E. Lehmann, P. Manfrinetti, A. Palenzona, I. Pallechi, M. Putti and C. Ferdeghini, *Supercond. Sci. Technol.* 21, 012001 (2008)
73. I. Pallechi, C. Tarantini, H. U. Aebersold, V. Braccini, C. Fanciulli, C. Ferdeghini, F. Gatti, E. Lehmann, P. Manfrinetti, D. Marré, A. Palenzona, A. S. Siri, M. Vignolo and M. Putti, *Phys. Rev. B* 71, 212507 (2005)
74. E. W. Collings, M. D. Sumption, M. Bhatia, M. A. Susner, S. D. Bohnenstiehl, *Supercond. Sci. Technol.* 21, 103001 (2008)
75. M. Eisterer, *Supercond. Sci. Technol.* 20, R47 (2007)
76. S. X. Dou, O. Sherbakova, W. K. Yeoh, J. K. Kim, S. Soltanian, X. L. Wang, C. Senatore, R. Flükiger, M. Dhallé, O. Husnjak and E. Babic, *Phys. Rev. Lett.* 98, 097002 (2007)
77. W. K. Yeoh and S. X. Dou, *Physica C* 456, 170 (2007)
78. M. Bhatia, M. D. Sumption and E. W. Collings, *IEEE Trans. Appl. Supercond.* 15, 3204 (2005)
79. Angst M., R. Puzniak, A. Wisniewski, J. Jun, S. M. Kazakov, J. Karpinski, J. Roos and H. Keller, *Phys. Rev. Lett.* 16, 7004 (2002)
80. L. Lyard *et al.*, *Supercond. Sci. Technol.* 16, 193 (2003)
81. A. Gurevich *et al.*, *Supercond. Sci. Technol.* 17, 278 (2003)
82. S. X. Dou, V. Braccini, S. Soltanian, R. Klie, Y. Zhu, S. Li, X. L. Wang, and D. Larbalestier, *J. Appl. Phys.* 96, 7549 (2004)
83. S. Patnaik *et al.*, *Supercond. Sci. Technol.* 14, 315 (2001)
84. A. Gurevich, *Phys. Rev. B* 67, 184515 (2003)
85. S. K. Chen, A. Serquis, G. Serrano, K. A. Yates, M. G. Blamire, D. Guthrie, J. Cooper, H. Wang, S. Margadonna and J. L. MacManus-Driscoll, *Adv. Funct. Mater.* 18, 113 (2008)
86. H. Yamada, M. Hirakawa, H. Kumakura, A. Matsumoto and H. Kitaguchi, *Appl. Phys. Lett.* 84, 1728 (2004)

87. H. Kumakura, H. Kitaguchi, A. Matsumoto and H. Hatakeyama, *Appl. Phys. Lett.* **84**, 18 (2004)
88. S. K. Chen, Z. Lockman, M. Wei, B. A. Glowacki and J. L. MacManus-Driscoll, *Appl. Phys. Lett.* **86**, 242501(2007)
89. Y. F. Lu, J. S. Li, S. K. Chen, G. Yan, M. H. Pu, C. S. Li and P. I. Zhang, *Physica C* **467**, 38 (2007)
90. A. Yamamoto, J. I. Shimoyama, S. Ueda, Y. Katsura, S. Horri and K. Kishio, *Supercond. Sci. Technol.* **18**, 116 (2005)
91. Y. Hishinuma, A. Kikuchi, Y. Iijima, Y. Yoshida, T. Takeuchi and A. Nishimura, *Supercond. Sci. Technol.* **19**, 1269 (2006)
92. B. J. Senkowicz, R. P. Moyet, R. J. Mungall, J. Hedstrom, O. N. C. Uwakweh, E. E. Hellstrom and D. C. Larbalestier, *Supercond. Sci. Technol.* **19**, 1173 (2006).
93. X. Xu, J. H. Kim, W. K. Yeoh, Y. Zhang and S. X. Dou, *Supercond. Sci. Technol.* **19**, L47 (2006)
94. A. N. Ling, C. Chen, X. Li and Q. R. Feng, *Front. Phys. China* **1**, 81(2007)
95. M. Maeda, Y. Zhao, S. X. Dou, Y. Nakayama, T. Kawakami, H. Kobayashi and Y. Kubota, *Supercond. Sci. Technol.* **21**, 032004 (2008)
96. T. Prikhna, W. Gawalek, Y. Savchuk, V. Moshchil, N. Sergienko, A. B. Surzhenko, M. Wendt, S. Dub, V. Melnikov, C. Schmidt and P. Nagorny, *Physica C* **386**, 565 (2003)
97. T. Prikhna *et al.*, *Physica C* **460**, 595 (2007)
98. X. L. Wang, S. Soltanian, M. James, M. J. Qin, J. Horvat, Q. W. Yao, H. K. Liu and S. X. Dou, *Physica C* **408**, 63 (2004)
99. N. A. Frederick, S. Li, M. B. Mapple, V. F. Nesterenko and S. S. Indrakanti, *Physica C* **363**, 1(2001)
100. P. C. Canfield, D. K. Finnemore, S. L. Bud'ko, J. E. Ostenson, G. Lapertot, C. E. Cunningham and C. Petrovic, *Phys. Rev. Lett.* **86**, 2423 (2001)
101. J. D. DeFouw and D. C. Dunand, *Appl. Phys. Lett.* **83**, 120 (2003)
102. C. B. Eom *et al.*, *Nature* **411**, 558 (2001)

103. H. J. Kim, W. N. Kang, E. M. Choi, M. S. Kim, K. H. P. Kim and S. I. Lee, *Phys. Rev. Lett.* 87, 087002 (2001)
104. H. G. Lee, J. G. Kim, L. S. Wang, W. S. Kim, L. S. Wook, K. D. Choi, G. W. Hong and T. K. Ko, *Physica C* 445, 1099 (2006)
105. K. Komori, K. Kawagishi, Y. Takano, H. Fujii, S. Arisawa, H. Kumakura, M. Fukutomi and K. Togano, *Appl. Phys. Lett.* 81, 1047 (2002)
106. H. Fang, P. T. Putman, S. Padmanabhan, Y. X. Zhou and K. Salama, *Supercond. Sci. Technol.* 17, 717 (2004)
107. H. L. Suo, C. Beneduce, M. Dhall'e, N. Musolino, J. Y. Genoud and R. Flükiger, *Appl. Phys. Lett.* 79, 3116 2001
108. H. Kumakura, A. Matsumoto, H. Fujii and K. Togano, *Appl. Phys. Lett.* 79, 2435 (2001)
109. G. Grasso, A. Malagoli, C. Ferdeghini, S. Roncallo, V. Braccini, A. S. Siri and M. R. Cimberle, *Appl. Phys. Lett.* 79, 230 (2001)
110. A. Serquis, L. Civale, D. L. Hammon, J. Y. Coulter, X. Z. Liao, Y. T. Zhu, D. E. Peterson and F. M. Mueller, *Appl. Phys. Lett.* 82, 1754 (2003)
111. H. Fang, S. Padmanabhan, Y. X. Zhou and K. Salama, *Appl. Phys. Lett.* 82, 4113 (2003)
112. G. Grasso, A. Malagoli, C. Ferdeghini, S. Roncallo, V. Braccini and A. S. Siri, *Appl. Phys. Lett.* 79, 230 (2001)
113. S. I. Schlachter, A. Frank, B. Ringsdorf, H. Orschulko, B. Obst, B. Liu and W. Goldacker, *Physica C* 445, 777 (2006)
114. P. Kováč, I. Hušek, C. Grovenor and C. Salter, *Supercond. Sci. Technol.* 16, 292 (2003)
115. P. Kováč, I. Hušek, W. Pachla, T. Melišek, R. Diduszko, K. Fröhlich, A. Morawski, A. Presz and D. Machajdik, *Supercond. Sci. Technol.* 15, 1127 (2002)
116. S. Soltanian, X. L. Wang, A. H. Li, E. W. Collings, M. D. Sumption, E. Lee, H. K. Liu and S. X. Dou, *Solid State Commun.* 124, 59 (2002)
117. R. Flükiger, H. L. Suo, N. Musolino, C. Beneduce, P. Toulemonde and P. Lezza, *Physica C* 385, 286 (2003)

118. M. D. Sumption, M. Bhatia, M. Rindfleisch, M. Tomsic and E. W. Collings, ***Supercond. Sci. Technol.*** 19, 155 (2006)
119. E. Martínez, L. A. Angurel and R. Navarro, ***Supercond. Sci. Technol.*** 15, 1043 (2002)
120. S. Zhou, A. V. Pan, M. Ionescu, H. Liu and S. X. Dou, ***Supercond. Sci. Technol.*** 15, 236 (2002)
121. E. Bellingeri, A. Malagoli, M. Modica, V. Braccini, A. S. Siri and G. Grasso, ***Supercond. Sci. Technol.*** 16, 276 (2003)
122. W. N. Kang, H.J. Kim, E. M. Choi, C. U. Jung and S. L. Lee, ***Science*** 292, 1521(2001)
123. H. J. Kim, W. N. Kang, E. M. Choi, M. S. Kim, K. H. P. Kim and S. Lee, ***Phys. Rev. Lett.*** 8708, 7002 (2001)
124. S. H. Moon, J. H. Yun, H. N. Lee, J. I. Kye, H. G. Kim, W. Chung and B. Oh, ***Appl. Phys. Lett.*** 79, 2429 (2001)
125. X. H. Zeng, A. V. Pogrebnyakov, A. Kotcharov, J. E. Jones, X. X. Xi, E. M. Lysczek, J. N. Redwing, S. Y. Xu, J. Lettieri, D. G. Schlom, W. Tian, X. Q. Pan and Z. K. Liu, ***Nature Materials*** 1, 35 (2002)
126. Lee S., ***Physica C*** 385, 31(2003)
127. Karpinski J., S. M. Kazakov, J. Jun, M. Angst, R. Puzniak, A. Wisniewski and P. Bordet, ***Physica C*** 385, 42 (2003)
128. Y. Feng, Y. Zhao, A. K. Pradhan, C. H. Cheng, J. K. F. Yau, L. Zhou, N. Koshizuka and M. Murakami, ***Appl. Phys. Lett.*** 92, 2614 (2002)
129. Y. Zhao, Y. Feng, C. H. Cheng, L. Zhou, Y. Wu, T. Machi, Y. Fudamoto, N. Koshizuka and M. Murakami, ***Appl. Phys. Lett.*** 79, 1154 (2001)
130. T. M. Shen, G. Li, C. H. Cheng and Y. Zhao, ***Supercond. Sci. Technol.*** 19, 1190 (2006)
131. S. Jin, H. Mavoori, C. Bower and R. B. van Dover, ***Nature*** 411, 563 (2001)
132. Y. Ma, H. Kumakura, A. Matsumoto and K. Togano, ***Appl. Phys. Lett.*** 83, 1181 (2003)

133. J. Wang, Y. Bugoslavsky, A. Berenov, L. Cowey, A. D. Caplin, L. F. Cohen, J. L. MacManus-Driscoll, L. D. Cooley, X. Song and D. C. Larbalestier, *Appl. Phys. Lett.* 81, 2026 (2002)
134. S. K. Chen, M. Wei and J. L. MacManus-Driscoll, *Appl. Phys. Lett.* 88 192512 (2006)

3

PREPARATION AND CHARACTERIZATION TECHNIQUES

3.1 Preparation of MgB_2 samples

In the present work, MgB_2 superconducting samples were prepared in bulk and wire forms. *In situ* solid state preparation method was used for both MgB_2 bulk and wires [1-3]. Mg powder (-325 #, <50 μm , 99.8 %, Good Fellow) and amorphous B powder (-325 #, <50 μm , 99 %, Merck) were used for all type of preparative methods. Synthesis of bulk samples was done using Powder In Sealed Tube (PIST) method whereas the wire samples were prepared by Powder In Tube (PIT) method. Detailed description of each method is given in coming sections.

3.1.1 Bulk MgB_2

Bulk MgB_2 polycrystalline samples were prepared using an *in situ* solid state synthesis method, namely Powder In Sealed Tube (PIST) [4, 5]. A schematic diagram of preparation procedure for PIST method is shown in *figure 3.1*. Stainless steel (SUS 304) tubes were used as the container for synthesis. One end of the tube was pressed uniaxially using a hydraulic press (Herzog TP 20P) so that it became tape shaped. Stoichiometric weights of magnesium and boron powders were taken using an electronic balance (Mettler AE240). The powders were mixed and ground thoroughly in air for about 0.5 hrs to get homogeneous fine powder using an agate mortar and pestle. Then the powder mixture was densely packed through the open end of the pressed SS tube leaving some space unfilled. The unfilled portion was pressed such that both the pressed ends are of equal length. Subsequently, the powder filled middle area was again subjected to uniaxial pressing to get a bar shaped portion. End sealing was performed by arc welding in order to avoid the escape of volatile Mg vapour during the heat treatment. A wet cloth was wound around the specimen during welding to avoid heating up of the sample. The samples were then heat treated directly

in air at 600-900 °C for appropriate durations with a ramp rate of 5 °C/min and subsequently allowed furnace cooling. Heat treatment of all the samples was done in a programmable muffle furnace having stability and accuracy better than 1 °C, controlled using a temperature controller (Eurotherm 2404). Bar shaped MgB_2 core was taken out by grinding the edges of the samples and then mechanically peeling off the SS sheath for structural and superconducting characterizations.

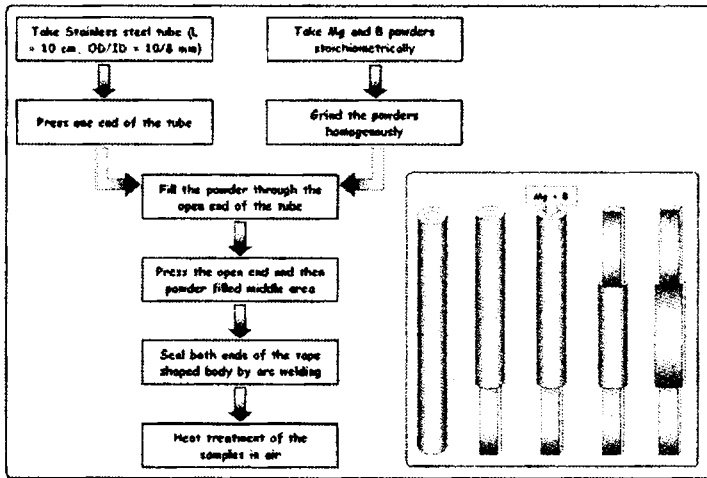


Figure 3.1: A schematic representation of preparation procedure by PIST method

3.1.2 Preparation of MgB_2 conductors

3.1.2.1 Monofilamentary wires

MgB_2 monofilamentary wires have been fabricated by the conventional PIT method [6-8]. Fe tubes (OD/ID = 5/3 mm) of length 5 cm were used for the preparation of short length monofilamentary wires for regular measurements. For the fabrication of multifilamentary wires, coils and current leads, Fe tubes (OD/ID = 8/6 mm) of length 10 cm were used. The tubes were filled with homogeneously mixed Mg and B powders and then mechanically compacted. The ends of the tubes were sealed by inserting copper studs and further crimped mechanically. The composite tubes were groove rolled down to desired dimensions without any intermediate annealing. The regular wires prepared had a diameter of 1.2-1.8 mm. The ends of the wires were pressed and then welded. Some of the

wires were heat treated by electrical self-heating (described in section: 5.8) and others in a muffle furnace at 550-850 °C for 0.5-2 hrs with a ramp rate of 10 °C/min followed by furnace cooling. After heat treatment, short length samples were cut for various structural and superconducting characterizations. A flowchart of preparation procedure for the fabrication of MgB_2 conductors is given in figure 3.2.

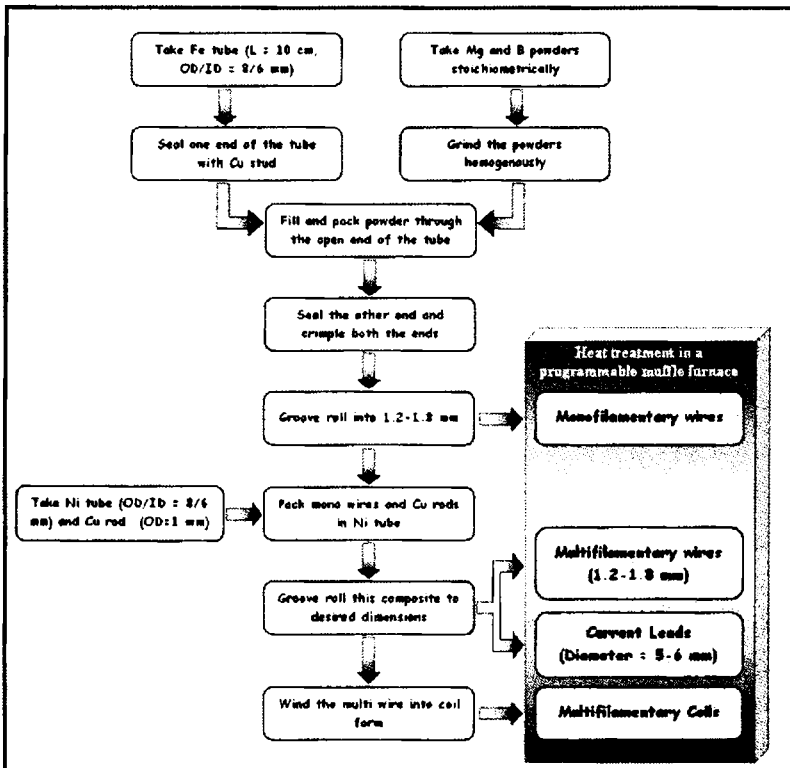


Figure 3.2: Flowchart shows the preparation procedure of mono and multifilamentary MgB_2 wires, coils and current leads

3.1.2.2 Multifilamentary wires

To prepare multifilamentary wires, the groove rolled monofilamentary wires were cut, bundled and packed inside Ni tubes (OD/ID = 8/6 mm) of length 10 cm. Cu wires of diameter 1 mm were also bundled inside the Ni tube along with the filaments. In the present work, multifilamentary MgB_2 conductors were prepared using Fe as inner sheath,

Cu as stabilizer and Ni as outer sheath [9]. Cu is used as the thermal stabilizer, since it has high thermal and electrical conductivity. Ni is chosen as the outer sheath due to its high oxidation resistance at high temperature heat treatment and favorable mechanical properties. The composite was then groove rolled and further heat treated as in the case of monofilamentary wires.

3.1.2.3 MgB₂ coils

The development of long length multifilamentary wires has enabled the design and fabrication of MgB₂ wound solenoid coils. The characterization of these coils gives information on the whole length superconducting properties of MgB₂ multifilamentary wires. In the present work, long multifilamentary wires up to a length of 3 m were prepared using MgB₂/Fe/Cu/Ni (diameter = 1.65 mm) composite. These wires were then wound and reacted to form coils. The coils were further coated with an insulating layer of stycast. The detailed descriptions of the wires and coils are discussed in *chapter 6*.

3.1.2.4 MgB₂ current leads

The MgB₂ based current lead is fabricated by PIT technique followed by Wire In Tube (WIT) method. The methodology adopted for the development of MgB₂ based current leads is shown in the flowchart (*figure 3.2*). Stabilized multifilamentary MgB₂ superconducting wires are the primary components for these leads. Current leads (MgB₂/Fe/Cu/Ni) of around 10 cm length and 5 mm diameter were fabricated from mono wires as test current leads. Detailed description of the current lead fabrication is given in *chapter 6*.

3.2 Structural characterization methods

3.2.1 X-ray diffraction (XRD) analysis

The X-ray powder diffraction technique is the most convenient and easy method for the phase identification of crystalline materials. This technique has been widely employed to examine the phase formation, lattice parameters, strain and grain size. XRD data can also be used for a semi-quantitative phase analysis.

In the present study, powder XRD patterns of the samples were taken using a *Philips X'pert Pro (PW 3040/60)* X-ray diffractometer with $\text{CuK}\alpha$ ($\lambda = 1.540566 \text{ \AA}$) radiation employing a proprietary detector viz. X'Celerator and a monochromator at the diffracted beam side. The system has θ - θ Bragg-Brentano geometry with fully automated operation and data acquisition. Programmable slits were used to limit the X-ray beam to the specified sample area. Most of the scans were performed under a tube voltage and current of 40 kV and 30 mA, respectively. The samples were scanned from 20° to 80° (2θ values) with a step size of $<0.02^\circ$. A typical scan takes about 20 minutes. The samples, either bulk or core of wire, were ground thoroughly into fine powder. The powder samples were then filled in standard sample holders and the XRD data were recorded at ambient conditions. For less amount of powder (especially from wires of smaller diameter) a standard zero background holder was used.

The recorded XRD data were then analyzed for phase identification and lattice parameter calculations. Phase identification of the samples was performed using X'Pert Highscore software with the support of ICDD PDF II database. The volume percentage of different phases in the samples was assessed semi-quantitatively, from the integrated X-ray peak intensities, using the relation:

$$\text{Vol.\% of phase X} = \frac{\sum \text{Integrated peak intensities of phase X}}{\sum \text{Integrated peak intensities of all phases}}$$

The d values of selected peaks of MgB_2 were used for its lattice parameter calculations. Lattice parameters were calculated for the hexagonal crystal structure of space group $p6/mmm$, using the relation:

$$\frac{1}{d^2} = \frac{4(h^2 + hk + k^2)}{3a^2} + \frac{l^2}{c^2}$$

The full width at half maximum (FWHM) of an XRD peak depends on factors like crystalline size, lattice strain, instrumental parameters etc. The FWHM of selected peaks of MgB_2 were used for qualitatively assessing the lattice strain and grain size. The analysis of Williamson-Hall plot (FWHM $\times\cos\theta$ against $\sin\theta$) was done to estimate the lattice strain and crystallite size from the slope and the y-intercept, respectively [10].

3.2.2 Microstructural characterization methods

The optical images of the cross section of MgB_2 wires were taken using an optical microscope. Grain morphology and microstructure have been examined by a scanning electron microscope (SEM) and a high resolution transmission electron microscope (HRTEM) equipped with energy dispersive spectroscopy (EDS).

3.2.2.1 Optical microscopy

Optical microscopy is used to analyze the cross section of the mono/multifilamentary wires. The cross sectional analysis provides the details regarding core area, homogeneity of the filaments, final geometry and the interface between core and sheath for the mono/multifilamentary conductors. An *OLYMPUS SZ-PT* model stereo microscope was used for the study and the samples were examined under magnification up to 30X. Optical microscopy measurements, taken with the help of a scale built into the eyepiece, were used for the exact estimation of core and sheath cross sectional areas of mono/multifilamentary wires/tapes. For the optical microscopy, samples of small size (1-2 cm) were cut from long conductors, polished mechanically and placed under the microscope in suitable holders.

3.2.2.2 Scanning electron microscopy (SEM)

The scanning electron microscope uses electrons rather than light to form image. Usually it is used to observe the features that are beyond the resolution of the human eye ($\sim 100 \mu\text{m}$). The combination of higher magnification, larger depth of focus, greater resolution and ease of sample observation makes the SEM one of the most heavily used material characterization techniques today. SEM is normally used to analyze the microstructural properties of materials such as phase formation, precipitations, porosity, shape/orientation of grains, grain size, grain boundary, texture and defects. In the present study, the microstructural analysis was done using a *JEOL JSM 5600LV* scanning electron microscope equipped with an energy dispersive X-ray spectrometer (*Phoenix*) used in secondary electron imaging (SEI) mode. The typical images were magnified up to 5000 and 10000 times. The instrument used in this study can magnify images to about 100 nm. Freshly fractured surfaces

of the samples were mounted on brass studs using adhesive carbon tapes. Polished surfaces were also used for some samples especially for wire/tape cross sectional analysis. Since the superconducting MgB_2 is electrically conducting, gold coating was not required. Finally, the brass studs with the mounted samples were loaded on the sample holder of the microscope.

3.2.2.3 Transmission electron microscopy (TEM)

TEM permits a direct observation and characterization of fine microstructure. Compared with SEM, TEM has a higher resolution (0.2 nm), which enables the microstructures to be observed in more detail. Besides grain morphology, electron diffraction pattern can be used to obtain precise informations regarding crystal structure, defects and lattice. In this study, TEM is mainly used to get intra and intergrain features of polycrystalline MgB_2 and to determine the grain morphology, grain size and informations of the nano sized dopants. The instrument used was *HRTEM FEI-Tecnai G² 30 S-Twin 300 KV* equipped with an X-ray energy dispersive spectrometer (EDS). Samples were finely powdered, ultrasonicated in acetone to remove agglomeration and then pipetted on carbon coated copper grids and finally loaded on the device. In the present work, energy dispersive X-ray (EDX) analysis was also done using automated EDS system integrated either to SEM or to TEM. The analysis was done at either single point or area of frame, depending on the requirement. The limitation of EDS in the present study was its inability to accurately detect boron in MgB_2 because of its low atomic weight.

3.3 Techniques used for superconducting characterization

The superconducting properties of MgB_2 have been investigated by measuring their transport and magnetic properties in self and applied magnetic fields. The superconducting parameters such as T_C , J_C , $J_C(H)$ and H_{irr} were measured using both magnetization and transport measurements to study the electromagnetic properties of MgB_2 samples prepared at different conditions. DC magnetization measurements up to 8 T were done using PPMS (Physical Property Measurement System), in collaboration with RRCAT (Raja Ramanna Centre for Advanced Technology, Indore) and JNCASR (Jawaharlal Nehru Centre for Advanced Science and Research,

Bangalore). An indigenously designed cryostat integrated with helium based cryocooler was used for self-field transport measurements and an 8 T LHe cooled solenoid magnet was used for field transport measurements. Bulk samples were used for magnetization measurements whereas short length wire samples were used for transport currents at high fields.

3.3.1 Magnetization measurements

High field magnetization measurements for the present study were done using a VSM (Vibrating Sample Magnetometer) and SQUID based PPMS in collaboration with RRCAT and JNCASR, respectively. Bulk samples of typical dimensions $3 \times 3 \times 1.5$ mm were used for the measurements. The measurements were done with magnetic field applied along the longest dimension of the samples. $M-T$ (magnetization vs. temperature) measurements were done at 25 or 100 Oe, mainly in zero field cooling (ZFC) condition. $M-H$ (magnetization vs. field) hysteresis loops were measured at 5 K up to 8 T. T_C of the sample is defined as the temperature at which the $M-T$ plot exhibits the onset of diamagnetic property. ΔT_C is taken as the difference between the temperatures corresponding to 90 % and 10 % of the maximum shielding signal. Magnetic field dependence of the critical current density, $J_C(H)$ of the sample was estimated based on Bean critical state model using the formula:

$$J_C(H) = \frac{20 \times \Delta M}{a(1 - a/3b)}$$

where ΔM (in emu/cm^3) is the width of the $M-H$ loop, a and b (in cm) are the dimensions ($a < b$) perpendicular to the field, for a parallelepiped shaped sample [11]. H_{irr} values of selected samples were estimated as the field at which J_C falls below $100 \text{ A}/\text{cm}^2$.

3.3.2 Transport measurements

Figure 3.3 shows a schematic sketch of the self and in-field transport measurements of MgB_2 wire samples using four probe resistivity method. For self-field transport measurements, an indigenously designed cryostat integrated with an imported cryocooler is used.

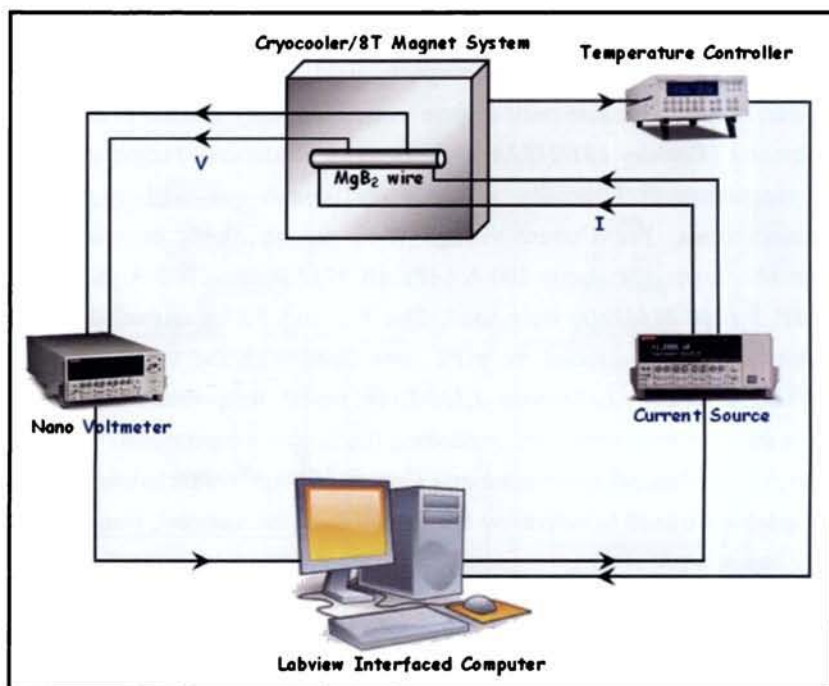


Figure 3.3: Schematic representation of self and in-field transport measurements of MgB₂ wire samples using four probe resistivity method

Figure 3.4 shows the schematic sketch of the cryocooler integrated cryostat. The cryocooler used is a Gifford-McMohan cooler manufactured by *Sumitomo Heavy Industries Ltd (SRDK-408)*. For transport measurements, MgB₂ wires of 6 cm length were anchored to a home made sample holder placed at the second stage of the cryocooler, where temperature can be lowered down to 6 K. Four probe resistivity method is used for the transport measurements (figure 3.3). Oxygen free high conductivity (OFHC) copper wires of suitable gauges were used for both current and voltage measurements. The end leads were directly soldered to the wire sample using ortho phosphoric acid as a flux, after thoroughly cleaning the sheath surface. The in-field transport measurements were carried out by using LHe based 8 T solenoid magnet system (*8 T – 77 mm bore superconducting magnet with J_C-VTI, model A8030-3*) manufactured by *American Magnetics Inc. (AMI)*. Figure 3.5 shows the magnet system comprising the superconducting magnet, variable temperature insert (VTI)

with helium vapor cooled current leads and liquid helium dewar. Samples can be inserted into the uniform magnetic field zone through the top of the dewar. A programmable milli ampere source (*Keithley 220/6220*) and nano voltmeter (*Keithley 181/2182A*) were used for Resistance-Temperature ($R-T$) measurements. Generally, a current of 100 mA was used for the $R-T$ measurements. For Current-Voltage ($I-V$) measurements programmable current sources of capacity 100 A (*APLAB 9711 P*) and 1000 A (*Sorensen DHP 5-1000 MIM9D*) were used. The $R-T$ and $I-V$ measurements were automated and controlled by a PC, interfaced with the system through *GPIB/LABVIEW*. *Lakeshore L332/L340* model temperature controllers were used for monitoring and controlling the sample temperatures.

Resistance-Temperature and Current-Voltage characteristics of the samples were used to determine the T_C and I_C of the samples, respectively. The temperature at which resistance falls sharply is taken as the T_C and the difference between the temperatures corresponding to the 90 % and 10 % of normal state resistivity is defined as ΔT_C for the samples. During $I-V$ measurements, a ramping current was passed for short durations (10-100 ms) at regular intervals of time. From the $I-V$ characteristics, the current at which the voltage shows a sharp rise is defined as the transport I_C . Ratio of I_C to the cross sectional area of MgB_2 core is taken as the critical current density (J_C). $J_C(H)$ and flux pinning force were calculated from the measurement of transport I_C at different magnetic fields.

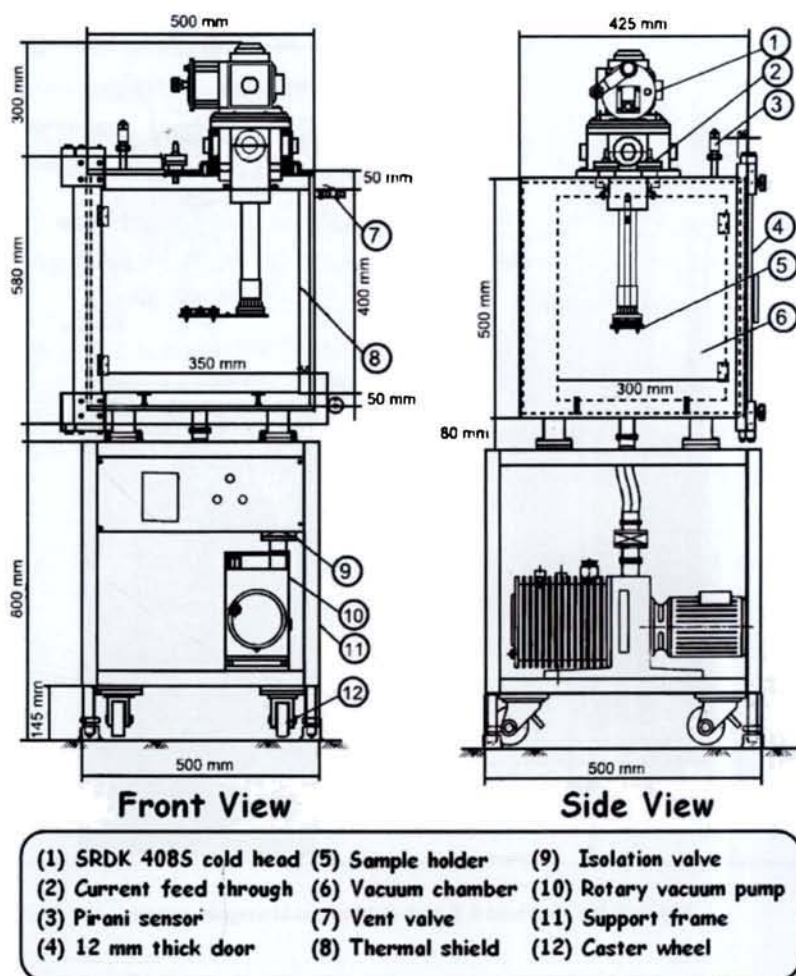


Figure 3.4: Schematic diagram of cryocooler integrated cryostat

References:

1. G. Grasso, A. Malagoli, C. Ferdeghini, S. Roncallo, V. Braccini and A. S. Siri, *Appl. Phys. Lett.* 79, 230 (2001)
2. S. Soltanian *et al.*, *Physica C* 361, 84 (2001)
3. B. A. Glowacki, M. Majoros, M. Vickers, J.E. Evetts, Y. Shi and I. McDougall, *Supercond. Sci. Technol.* 14, 193 (2001)
4. R. G. Abhilash Kumar, K. Vinod, R. P. Aloysius and U. Syamaprasad, *Mater. Lett.* 60, 3328 (2006)
5. Neson Varghese, K. Vinod, S. Rahul, P. Anees, K. M. Devadas, Syju Thomas, Shipra, A. Sundaresan, S. B. Roy and U. Syamaprasad, *J. Am. Ceram. Soc.* 94, 1133 (2011)
6. S. I. Schlachter, W. Goldacker, A. Frank, B. Ringsdorf and H. Orschulko, *Cryogenics* 46, 201 (2006)
7. M. Tomsic, M. Rindfleish, J. Yue, K. McFadden, D. Doll, J. Phillips, M. D. Sumption, M. Bhatia, S. Bohnenstiehl and E. W. Collings, *Physica C* 456, 203 (2007)
8. Neson Varghese, K. Vinod, S. Rahul, K. M. Devadas, Syju Thomas, S. Pradhan and U. Syamaprasad, *J. Appl. Phys.* 109, 033902 (2011)
9. K. M. Devadas, S. Rahul, Syju Thomas, Neson Varghese, K. Vinod, U. Syamaprasad, S. Pradhan, M. K. Chattopadhyay and S. B. Roy, *J. Alloys Compounds* 509, 8038 (2011)
10. G. K. Williamson and W. H. Hall, *Acta Metall.* 1, 22 (1953)
11. C.P. Bean, *Phys. Rev. Lett.* 8, 250 (1962)

4.1: Introduction

MgB_2 is certainly a beneficial superconductor due to its strong grain coupling for superconducting current, long coherence length, high carrier density, low electromagnetic anisotropy, and simple binary composition without expensive elements. It has already been fabricated in the form of bulk, single crystals, thin films, tapes and wires. Moreover, the J_C of pristine MgB_2 bulk at low magnetic fields is high enough for low field applications. But it rapidly decreases with an increase of magnetic field due to low H_{C2} and lack of effective pinning sites. Therefore, both the enhancement of H_{C2} and the introduction of effective pinning sites are essential to improve J_C under high magnetic fields for its practical application [1, 2]. Significant research has been done in developing various techniques like irradiation of energetic ions or neutron and chemical doping for the improvement of flux pinning and hence $J_C(H)$ and H_{C2} in MgB_2 [3-8]. Among these, chemical doping is an effective and easy method for modifying the properties of MgB_2 . Doping of elements or compounds into MgB_2 accompanies element substitution and/or inclusion of impurity particles. In the former case, changes of electronic state, lattice constants and crystallinity are expected to occur; while in the latter case, impurity particles are expected to be dispersed as inclusions throughout the MgB_2 matrix so as to act as effective pinning sites. Elemental substitution at Mg/B site introduces defects in the MgB_2 structure which decreases the mean free path of the normal electrons and creates local pinning centers. This consequently increases the H_{C2} and irreversibility line. Another expected effect of doping is the suppression of the grain growth of MgB_2 . Of the various dopants tried for substitution in MgB_2 , carbon containing compounds seem to be the most effective. On considering doping via inclusion of impurities, the particle size of the additive used is very important. The addition of nano sized dopants is found

to be much effective in MgB₂, since it leads to the formation of nano particle secondary phase inclusions comparable to the coherence length of MgB₂ and thereby enhances the grain connectivity and flux pinning.

4.2: Preparation and characterization of bulk MgB₂

Bulk MgB₂ samples were prepared by *in situ* Powder In Sealed Tube (PIST) method [9-10]. Stainless steel (SS) SUS 304 tubes of 10 cm length with an OD of 10 mm and ID of 8 mm were used for synthesis. One end of the tube was pressed uniaxially (~ 1 GPa) using a hydraulic press so that it became bar shaped. Stoichiometric weights of Mg powder (-325 #, <50 μm, 99.8 %) and B powder (-325 #, <50 μm, 99 %, amorphous) were taken using an electronic balance. Powders were mixed and ground thoroughly in air for about 30 minutes to get homogeneous fine powder using an agate mortar and pestle. Then the powder mixture was densely packed through the open end of the pressed SS tube leaving some space unfilled. The unfilled portion was pressed with the same pressure as that of previous end such that both the pressed ends are of equal length. Subsequently, the powder filled middle area was again subjected to uniaxial pressing to get a bar shaped portion. End sealing was performed by arc welding in order to avoid the escape of volatile Mg. A wet cloth was wound around the specimen during welding to avoid heating up of the sample. Samples were then heat treated directly in air at desired temperatures in a programmable muffle furnace with a ramp rate of 5 °C/min and subsequently performed furnace cooling. Then, bar shaped MgB₂ core was taken out by mechanically peeling off the SS sheath for XRD, SEM and magnetic measurements.

The structural and phase analysis of the samples were performed using an X-ray diffractometer. Phase identification of the samples was performed using X'Pert Highscore Software in support with ICDD PDF II database. The grain morphology and microstructure were examined by SEM and HRTEM. DC magnetic measurements were carried out using a SQUID/VSM based magnetometer on cut pieces having dimensions of 3×3×1.5 mm, with applied field along the longest dimension. The

preparation and characterization of bulk MgB₂ samples has been given in chapter 3 and the same is pursued in the following sections.

4.3: Pristine MgB₂: Effect of processing temperature on structural and superconducting properties

4.3.1: Introduction

Considerable efforts have been made on the synthesis of samples in the form of bulk, thin film, tape and wire. The factors such as purity and size distribution of precursor powder, fabrication procedures and heat treatment schedule influence the superconducting properties of bulk MgB₂. There are two main routes to prepare bulk MgB₂: one, based on the reaction of pure elements (*in situ* technique) [11-13] and the other, sintering of pre-reacted MgB₂ powders (*ex situ* technique) [14-16]. Of which *in situ* method is more preferred since it provides better grain connectivity and effective control of pinning centers. Improvement in $J_C(H)$, H_{C2} and H_{irr} is the key factor for practical applications of MgB₂ superconductor and this depends sensitively on flux pinning, grain connectivity, density, chemical composition and microstructure. MgO phase at the grain boundaries is the major impurity in the *in situ* synthesized MgB₂ that severely affects the J_C . The MgO at the grain boundaries acts as weak links and significantly reduces the intergrain J_C [17].

Several synthesis procedures have been reported for *in situ* bulk MgB₂ synthesis. Generally, the synthesis is done by enclosing samples in Nb/Ta tubes or foils in inert atmosphere or vacuum. The maximum J_C reported is only in the range 10^2 - 10^4 A/cm² at 20 K and 2 T [18-21]. This is due to high volatility of Mg at elevated temperatures resulting in high porosity and poor superconducting properties. Although reasonably dense bulk MgB₂ samples were obtained under hot pressing of specimen at high pressure and high temperature, the large scale exploitation of MgB₂ as a potential material for various practical applications requires the development of more simple and cost effective processing techniques [22-25]. The method we used for bulk MgB₂ synthesis is *in situ* PIST technique in which the ends of the powder filled tubes were pressed and sealed by 'cold-welding' so that the samples can be heat treated directly in air. This

can practically eliminate Mg evaporation loss and minimize oxidation of Mg and reduce the cost of synthesis by avoiding expensive Nb/Ta tubes or foils, inert gases and special furnaces. For *in situ* synthesis of MgB₂, the synthesis method and processing temperature have strong influence on the phase formation, crystallinity and microstructure and hence on the superconducting properties of the material. Therefore, an attempt has been made to optimize the processing temperature of bulk MgB₂ using PIST method. The melting point of Mg, a precursor for MgB₂, is around 650 °C. But MgB₂ processed at temperatures even up to 750 °C showed the presence of unreacted Mg. Moreover, at temperatures above 900 °C, the formation of MgO was found to increase. Hence, to tune the optimum processing temperature which yields the best properties for MgB₂, a temperature range 750-900 °C was chosen. The samples were heat treated at 750, 800, 850, and 900 °C for 2 hrs and named as MB750, MB800, MB850 and MB900 respectively.

4.3.2: Results and discussion

Figure 4.1 shows powder XRD patterns of bulk MgB₂ heat treated at different temperatures 750, 800, 850, and 900 °C for 2 hrs. All the XRD patterns show sharp peaks of MgB₂ phase with only a minute fraction of MgO. Traces of MgO observed are due to the entrapped air in the reaction mixture before end sealing of the tubes. Small amount of unreacted residual Mg is detected for the sample heat treated at 750 °C. This is because the melting point of Mg is around 650 °C, which is very much less than that of B (2080 °C) and so the kinetics of the expected liquid-solid reaction between Mg and B is not fast enough at this temperature to complete the reaction. However, MgB₂ peaks become sharper and stronger as the heat treatment temperature increases which indicate increase in phase purity and/or crystallinity. Absence of the peaks corresponding to MgB₄ or other higher borides in all the samples confirms that there is no evaporation of Mg during the heat treatment process. Moreover, absence of the peaks corresponding to Fe and Fe containing compounds indicates that there is no interfacial reaction occurring between Mg/B/MgB₂ and SS sheath at these temperatures.

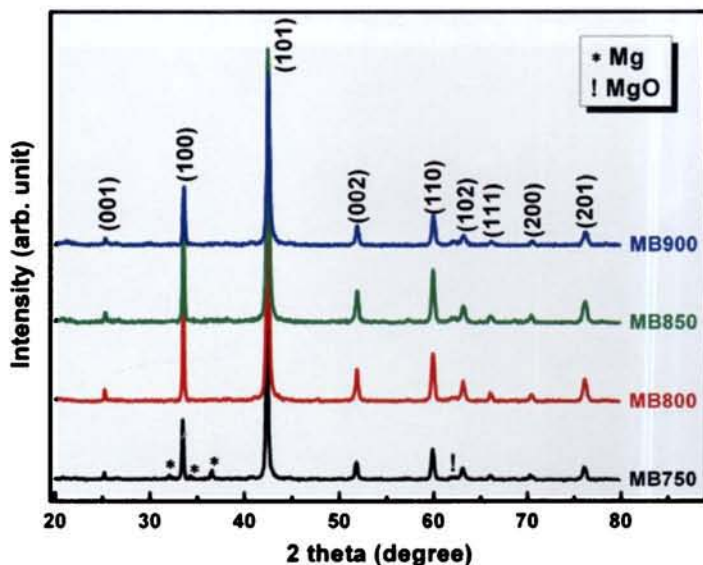


Figure 4.1: XRD patterns of MgB₂ samples heat treated at different temperatures (750, 800, 850 and 900 °C)

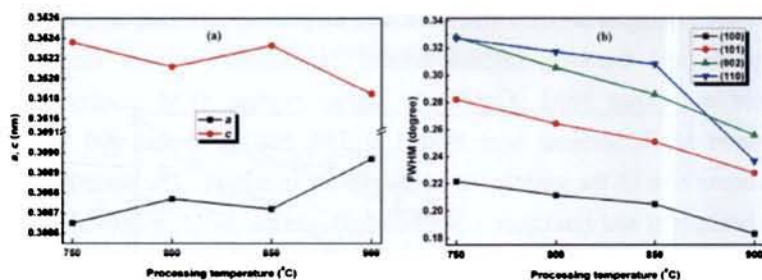


Figure 4.2: Variation of (a) Lattice parameters a & c and (b) FWHM of (100), (101), (002) and (110) peaks of MgB₂ samples with processing temperature

Lattice parameters a , c and full width at half maximum (FWHM) of the (100), (101), (002) and (110) peaks of the samples are shown in figure 4.2. The lattice parameters are calculated from XRD for hexagonal structure with space group $p6/mmm$. The samples show no significant variations in lattice parameters within the experimental error. FWHM of all the peaks decreases significantly on increasing the sintering temperature indicating the increase in grain size of MgB₂ with temperature.

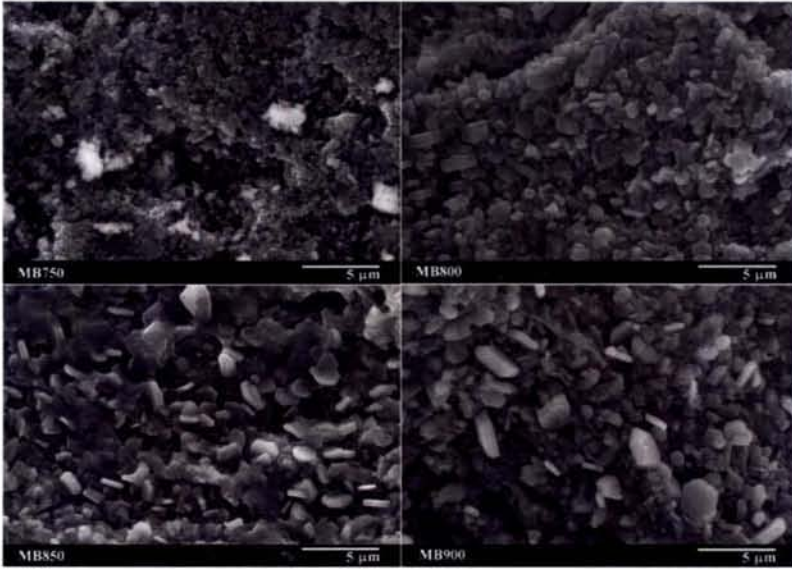


Figure 4.3: SEM images of bulk MgB_2 heat treated at 750, 800, 850 and 900 °C

To analyze the effect of grain size on peak broadening and study the morphological features, microstructural examination of the samples is carried out using SEM. *Figure 4.3* shows typical SEM images of the fractured MgB_2 samples heat treated at 750, 800, 850, and 900 °C. The microstructure of the samples is homogenous in nature. The samples show fine hexagonal and randomly oriented MgB_2 grains. SEM images also show that the average grain size of the crystalline MgB_2 increases with sintering temperature, well in agreement with the decrease of FWHM from XRD. It is to be noted that the smaller grain size of pure MgB_2 processed at lower temperatures increases the number of grains which in turn enhances the density of grain boundaries. In pure MgB_2 , grain boundaries are the main flux pinners [26, 27]. Hence, the increased number of grains contributes to enhance the flux pinning property and hence the $J_C(H)$ characteristics of the samples processed at relatively low temperatures.

Temperature dependence of magnetization ($M-T$) of the samples is shown in *figure 4.4*. All the samples show sharp superconducting transitions with T_C around 38.5 K and $\Delta T_C (T_{C90\%} - T_{C10\%}) \sim 1$ K indicating the high

phase purity and homogeneity of MgB_2 samples sintered at different temperatures. Almost identical T_C and ΔT_C values of the samples indicate that the final stoichiometry of all the samples are same and samples are identical with respect to lattice or structural defects and electronic states in the superconducting B planes.

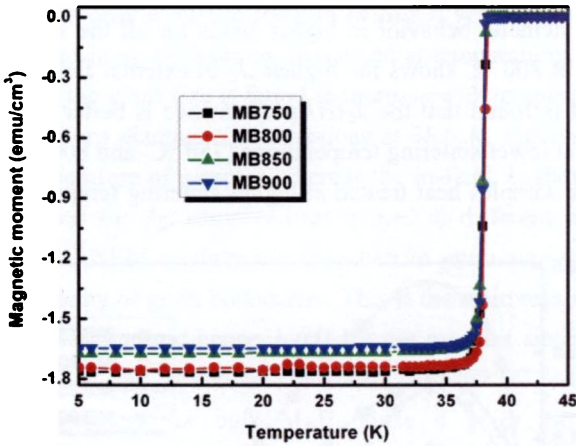


Figure 4.4: DC magnetic susceptibility versus temperature plots of MgB_2 samples processed at different temperatures

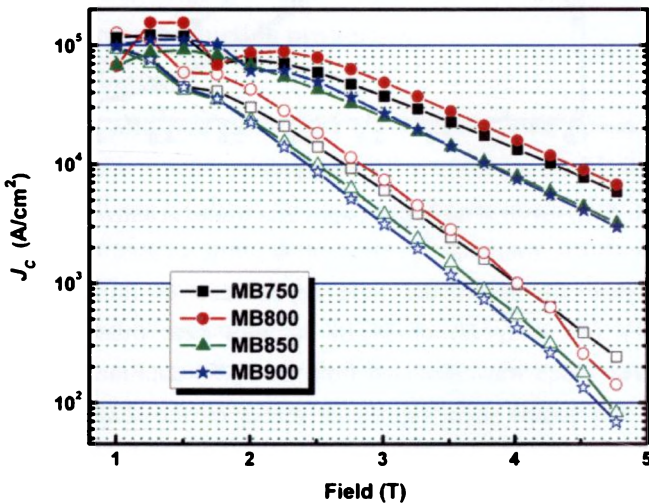


Figure 4.5: $J_c(H)$ curves of MgB_2 samples synthesized at different temperatures. Closed and open symbols represent $J_c(H)$ at 10 K and 20 K respectively

The critical current density J_C of the bulk MgB_2 samples was calculated from the width of the magnetization hysteresis ($M-H$) loops on the basis of the Bean critical state model [28]. Figure 4.5 illustrates the dependence of J_C on applied magnetic fields up to 5 T of MgB_2 samples at 10 K and 20 K. At 10 K, J_C jumps abruptly at low fields where the estimation of J_C may not be accurate due to the flux jumps whereas $J_C(H)$ follows a systematic behavior in higher fields for all the samples. Sample heat treated at 800 °C shows the highest J_C in external fields at both 10 K and 20 K. It is found that the $J_C(H)$ performance is better for the samples heat treated at lower sintering temperatures (750 °C and 800 °C), while it is lower for the samples heat treated at higher sintering temperatures (850 °C and 900 °C).

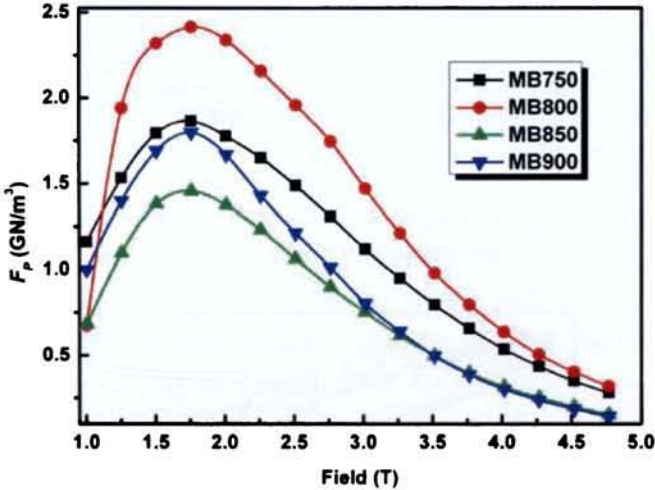


Figure 4.6: $F_p(H)$ curves of the MgB_2 samples heat treated at different temperatures

Figure 4.6 shows the field dependence of flux pinning force density, F_p ($F_p = J_C \times H$) of MgB_2 samples heat treated at different temperatures which was calculated from the $J_C(H)$ data measured at 10 K. Since the flux jumps show significant marks on the shape of the $F_p(H)$ curves, the curves are plotted after refining the $J_C(H)$ data up to 2 T. The samples heat treated at relatively lower temperatures (MB750 and MB800) showed enhanced flux pinning as compared to those processed at higher temperatures. The reduced grain size and hence the increased grain

boundary is the main reason behind the improved flux pinning and $J_C(H)$ for the samples sintered at lower temperatures.

4.3.3: Conclusion

The superconducting properties of bulk *in situ* PIST MgB₂ at different temperatures were studied. XRD analysis gives sharp peaks of MgB₂ phase with only a minute fraction of MgO. Well crystallized MgB₂ grains are formed in all the samples processed at temperatures in the range 750-900 °C and the grain size is found to increase with temperature. All the samples show sharp diamagnetic transitions at 38.5 K, independent of the processing temperature of samples whereas the in-field J_C shows distinctly different behavior for the samples heat treated at different temperatures. Both FWHM and SEM confirm the reduction in grain size which in turn increases the density of grain boundaries. This is the main reason behind the improved flux pinning and hence $J_C(H)$ for the samples sintered at lower temperatures. Therefore, it can be concluded that 800 °C is the optimum processing temperature for bulk MgB₂ since it gives the best $J_C(H)$ performance when compared to the rest.

4.4: Nano oxide doped MgB₂: A comparative study on structural and superconducting properties

4.4.1: Introduction

Doping with rare earth (RE) elements has little effects on T_C of MgB₂ due to the low solid solubility of RE elements in the MgB₂ lattice as well as the relatively localized 4f electrons. The paramagnetism of the rare earth metals originates from their inner 4f electrons which are rather localized [29]. The itinerant 3d electrons of transition metals may interact with the conduction electrons of the system whereas the localized 4f electrons do not interact with the conduction electrons, thus superconductivity is not suppressed by the RE elements while it is remarkably suppressed by ferromagnetic elements. Hence, rare earth oxide dopants are good candidates to enhance flux pinning properties of MgB₂. It has been reported that doped rare earth oxides (REO) give rise to REB₆ and REB₄ impurity precipitates which get embedded into the MgB₂ matrix and

work as effective pinning centers; significantly improving J_C and H_{irr} of MgB_2 [30-35]. Here, typical nano sized rare earth oxides like nano Tb_4O_7 (n- Tb_4O_7), nano Ho_2O_3 (n- Ho_2O_3) and a non rare earth oxide, nano SiO_2 (n- SiO_2), have been chosen for studying their effect on bulk MgB_2 . The weight percentage of dopant to be added was fixed after analyzing bulk MgB_2 samples doped with different doping levels of each nano oxides. It was seen that MgB_2 samples doped with 5 wt% of nano oxides gave the best $J_C(H)$ performance and hence, doped samples with 5 wt% of each nano oxide are chosen for a comparative study of their effects on MgB_2 . Polycrystalline MgB_2 (MB), MgB_2+5 wt% n- Tb_4O_7 (MBTb), MgB_2+5 wt% n- Ho_2O_3 (MBHo) and MgB_2+5 wt% n- SiO_2 (MBSi) were prepared by *in situ* PIST method, using Mg, amorphous B, Tb_4O_7 (< 60 nm, 95+ %), Ho_2O_3 (< 60 nm, 99.5+ %) and SiO_2 (10 nm, 99.5 %) as starting powders. The preparation and characterization of samples are detailed in previous sections.

4.4.2: Results and discussion

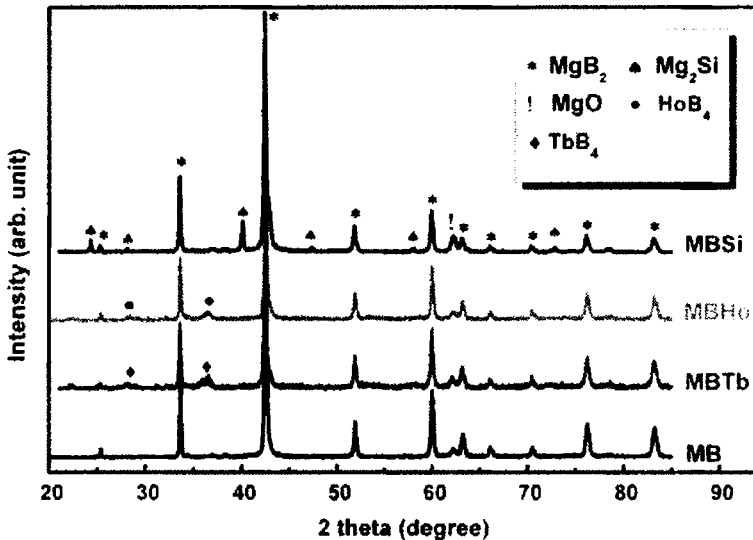


Figure 4.7: XRD patterns of pure and nano oxide doped MgB_2 samples

Figure 4.7 shows the XRD patterns of MgB₂ with different nano oxide dopants, heat treated at 800 °C for 2 hrs. MgB₂ is the main phase, with a trace amount of MgO, observed in all the samples. The peak intensities of MgB₂ are reduced in doped samples, indicating that the undoped sample has better phase purity and crystallinity. In n-REO doped samples, the presence of REB₄ indicates that the added n-REO decomposed and reacted with B, whereas in n-SiO₂ doped samples the dopant reacted with Mg to form Mg₂Si. The slight MgO observed in pure sample is due to the entrapped air before end sealing of the tubes, and the amount of MgO in the doped samples is slightly higher compared to the undoped sample, which is due to the excess oxygen available from the added oxides. The *a* and *c* lattice parameters, calculated from the XRD data, for a hexagonal crystal structure, are given in table 4.1. However, the very small change in the lattice parameters may be due to the strain induced by the nano particles, rather than a substitutional effect or structural change, as suggested by Wang *et al.* for Y₂O₃ addition [30].

Table 4.1: Structural and superconducting properties of pure and doped MgB₂

Samples	Lattice parameters (nm)		<i>T_C</i> (K)	ΔT_C (K)	<i>J_c</i> (A/cm ²) at 5 K		<i>H_{irr}</i> (T) at 5 K
	<i>a</i>	<i>c</i>			4 T	8 T	
					($\times 10^4$)	($\times 10^2$)	
MB	0.3087	0.3519	38.6	1.01	1.4	1.8	7.5
MBTb	0.3087	0.3515	38.5	1.01	2.3	0.7	7.9
MBHo	0.3085	0.3517	38.1	1.01	3.5	1.9	8.8
MBSi	0.3084	0.3520	38.3	1.02	3.2	8.3	10.4

Figure 4.8 shows the SEM images of the fractured surfaces of pure and nano oxide doped MgB₂ samples. All the samples show homogenous microstructure with tiny hexagonal and randomly oriented grains of average size around 1 μ m wherein the grain boundaries are sharp and clear except for MBHo. The MBHo has tightly packed well connected MgB₂ grains with size relatively smaller than the others.

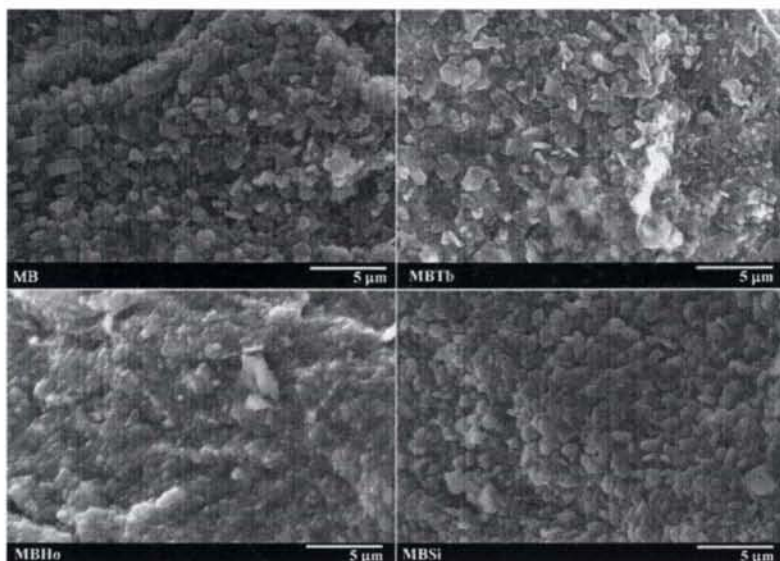


Figure 4.8: SEM images of pure and nano oxide doped MgB_2 samples

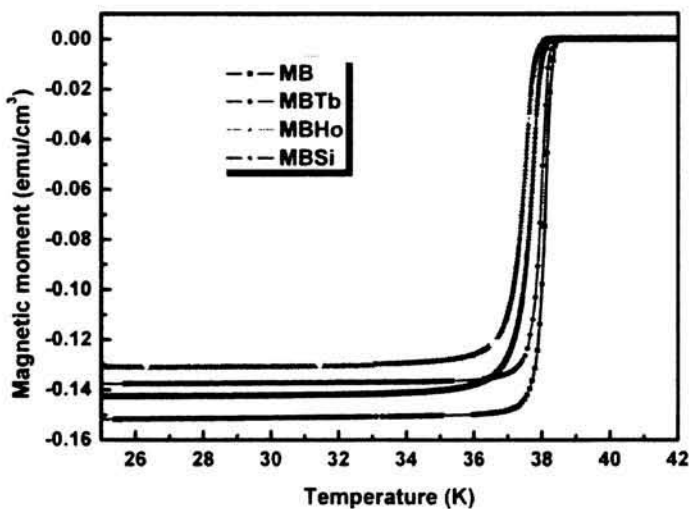


Figure 4.9: DC magnetic susceptibility vs temperature plots of pure and nano oxide doped MgB_2 samples

$M-T$ plots of the samples are shown in figure 4.9. All the samples show sharp superconducting transitions with T_C in the range 38.1-38.6 K

and $\Delta T_C \sim 1$ K. The almost identical T_C and lower ΔT_C indicate that the samples have high crystallinity and homogeneity and are not affected by any grain boundary connectivity problem. This infers that the doped nano oxides and the addition induced reacted secondary phases are incorporated within the MgB_2 grains rather than precipitated or segregated at the grain boundaries.

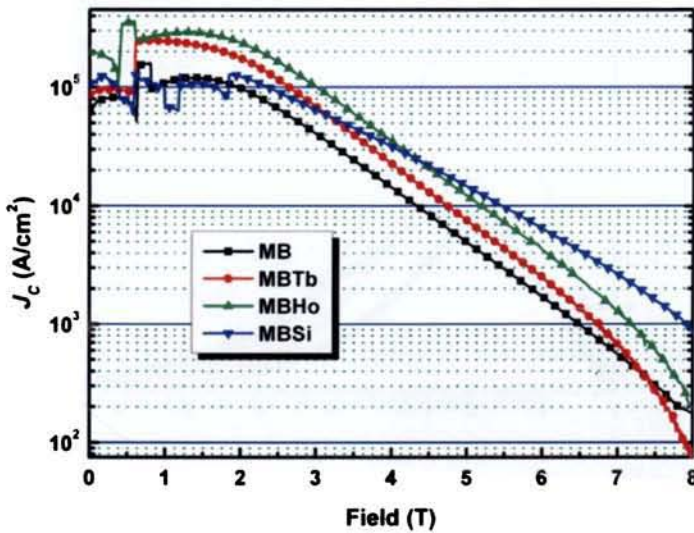


Figure 4.10: $J_C(H)$ curves of pure and nano oxide doped MgB_2 samples

Figure 4.10 shows the field dependence of magnetic J_C of the samples upto a field of 8 T at 5 K, deduced from $M-H$ data. Materials with high critical current density, high magnetic diffusivity and low heat capacity usually cause thermomagnetic flux jumps in magnetization hysteresis loop. Such thermomagnetic flux jumps are observed around 1 T for all the samples. When compared to the undoped sample, the $J_C(H)$ is enhanced for all the doped samples, for the entire field of study. At lower fields, the improvement in $J_C(H)$ is higher for n-REO doped samples but at higher fields the n- SiO_2 doped sample shows better $J_C(H)$ performance. The better low field J_C of these n-REO doped samples indicates that the grain connectivity is not disturbed by the secondary phases precipitated by them. The enhanced $J_C(H)$ performance of MBHo at lower fields can be attributed to the improved grain connectivity as observed in SEM. As shown in table

4.1, it can be seen that the $J_C(H)$ and H_{irr} are significantly improved for all nano oxide doped MgB_2 samples. The improvement in $J_C(H)$ and H_{irr} of the doped samples can be due to the flux pinning caused by the nano sized secondary phases with size comparable to the coherence length of MgB_2 .

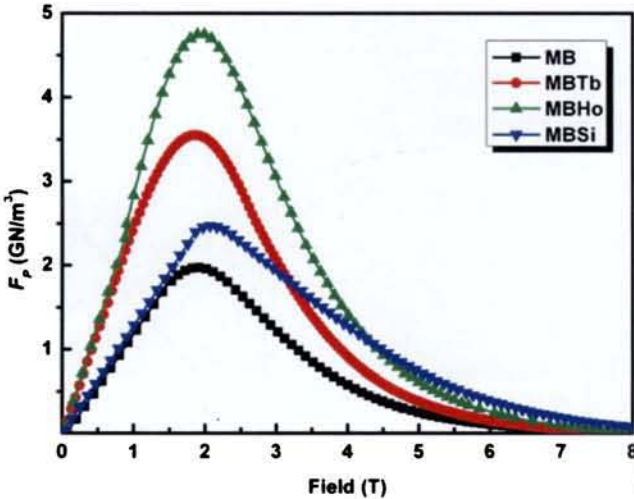


Figure 4.11: $F_p(H)$ curves of the pure and nano oxide doped MgB_2 samples

In order to analyze the flux pinning behavior, F_p of undoped and doped samples at 5 K is calculated (figure 4.11). Since the flux jumps show significant marks on the shape of the curves, the curves are plotted after refining the $J_C(H)$ data up to 2 T. The introduction of nano dopants in MgB_2 , generally, increases the density and strength of flux pinning centers either by substitution or homogeneous nano inclusions (reacted or unreacted impurities). All the nano oxide doped MgB_2 samples show enhanced flux pinning strength up to 8 T, when compared to the pure one. The maximum flux pinning force density (F_{pmax}) values for MB, MBTb, MBHo and MBSi are 2.0, 3.5, 4.7 and 2.5 GN/m^3 respectively. Among all, n- Ho_2O_3 doped MgB_2 sample shows the maximum flux pinning behavior in the entire field of study. Ho_2O_3 causes the formation of HoB_4 as the reacted impurity phase, which possesses a strong magnetic moment. Since magnetic impurities like HoB_4 can interact more strongly with the flux lines and exert a strong force to trap the flux lines, n- Ho_2O_3 doped sample exhibits better flux pinning behavior and hence $J_C(H)$ performance.

4.4.3: Conclusion

The effect of nano oxide dopants on the microstructural and superconducting properties of *in situ* bulk MgB_2 was studied. Absence of appreciable change in lattice parameters and T_C , points out that the additives are not substituted at either Mg or B sites in MgB_2 . In n-REO doped samples, the added n-REO decomposes and reacts with B to form REB_4 whereas in n- SiO_2 doped samples the dopant reacts with Mg to form Mg_2Si . On comparing with pure sample, the $J_C(H)$ performance is significantly enhanced for all the doped samples. The addition induced reacted phases act as strong flux pinners thereby improving the $J_C(H)$ and H_{irr} of the nano oxide doped samples. Flux pinning analysis also confirms the same. The n- Ho_2O_3 doped MgB_2 sample shows the maximum flux pinning behavior in the entire field of study due to the presence of magnetic impurities like HoB_4 as strong flux pinners.

4.5: Carbon variants doped MgB_2 : A comparative study on structural and superconducting properties

4.5.1: Introduction

Of the various elements and compounds being doped in MgB_2 , carbon containing compounds such as SiC , C , B_4C and hydrocarbons have been found to be the most efficient for significant J_C enhancement in high magnetic fields [36, 37]. Since MgB_2 is a two gap superconductor, the substitution of carbon for boron has a great impact on the carrier density and impurity scattering [38]. The $J_C(H)$ characteristics depend not only on C substitution but also on the effectiveness of the dopant in the formation and distribution of nano scale secondary phases into the grains as flux pinners. It was observed that the amount of C getting substituted and the efficacy of the resulting secondary precipitates, mostly depend on the nano additive used. In order to improve the superconducting properties especially the in-field J_C , an attempt has been made to study bulk MgB_2 samples doped with typical variants of carbon. The weight percentage of carbon dopant to be added was fixed after analyzing bulk MgB_2 samples doped with different doping levels of carbon ($MgB_{2-x}C_x$ where $x: 0 \rightarrow 0.2$). It was seen that MgB_2 samples doped with 2.6 wt% of carbon dopant ($MgB_{1.9}C_{0.1}$) gave the best

$J_c(H)$ performance [39]. Hence, all the doped variants of MgB_2 containing 2.6 wt% of carbon are chosen for a comparative study of their effects on structural and superconducting properties of MgB_2 . The carbon variants such as nano diamond (n-D), nano carbon (n-C), nano silicon carbide (n-SiC) and burned rice husk (BRH) are used in the present study.

Considering the significant improvement in $J_c(H)$ by n-SiC and n-C additions [39, 40], BRH is explored as an alternative low cost replacement of these expensive nano dopants. BRH is a nonconventional raw material of SiC which contains ultra fine amorphous silica (SiO_2) and carbon. The presence of amorphous SiO_2 in a matrix of friable carbon, easy availability and low cost make BRH a promising dopant for MgB_2 . The ratio of SiO_2 to C in BRH can be optimized by controlling the burning temperature of rice husk. The structural and superconducting properties of all the nano sized carbon variants mentioned above are compared with the best result obtained for BRH doped MgB_2 (5 wt%).

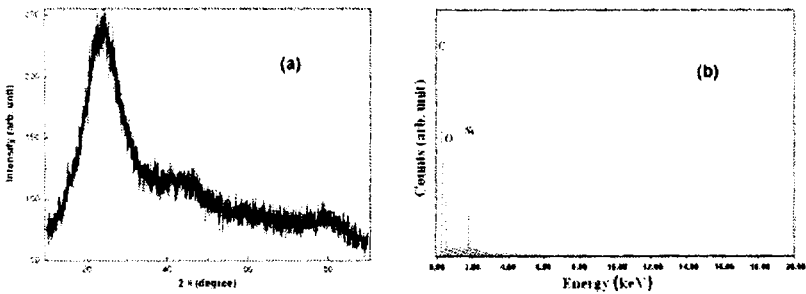


Figure 4.12: (a) XRD pattern and (b) EDX analysis of burned rice husk

Polycrystalline bulk MgB_2 and its doped variants (dopants: n-D, n-C, n-SiC and BRH) were prepared by *in situ* PIST method using Mg, amorphous B, n-D (< 10 nm, 95+ %), n-C (< 50 nm, 99+ %), n-SiC (< 100 nm, 97.5+ %) and BRH as the starting materials. The BRH used here was prepared by heating the raw rice husk at 300 °C for 1 hr. Figure 4.12(a) shows the powder XRD pattern of the BRH powder which gives only a broadened peak of SiO_2 , indicating its amorphous nature. Since the XRD doesn't show the presence of amorphous C, EDX analysis of BRH was also carried out which confirmed the presence of Si (~40 wt%), O (~10 wt%)

and C (~50 wt%) as shown in figure 4.12(b). The preparation and characterization of samples are detailed in previous sections. The MgB_2 samples, pure and those doped with n-D, n-C, n-SiC and BRH, are named as MB, MBD, MBC, MBS and MBR respectively.

4.5.2: Results and discussion

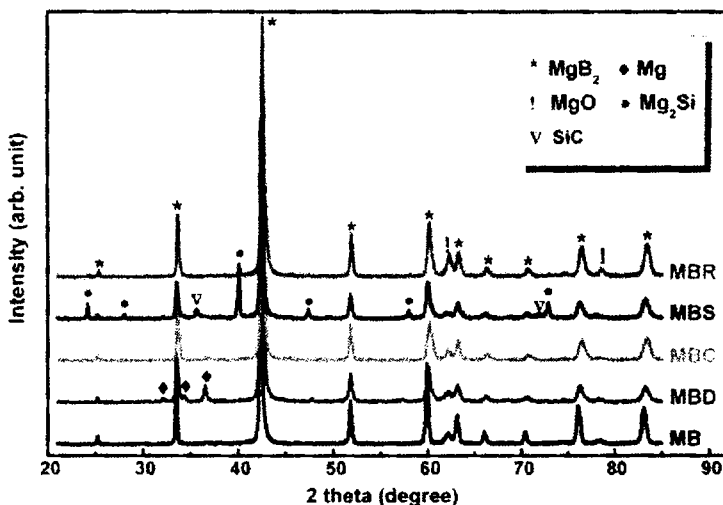


Figure 4.13: XRD patterns of pure and carbon variants doped MgB_2 samples

Figure 4.13 shows the XRD patterns of pure and carbon variants doped MgB_2 samples. All the samples show MgB_2 as the main phase with a trace amount of MgO . The MgO formation is due to entrapped air before the end sealing of the tubes. For n-D doped sample, slight amount of unreacted Mg is detected apart from MgO even at low level doping. The presence of unreacted Mg and the absence of any C containing secondary phases in MBD indicate the relatively low reactivity of n-D at the synthesis temperature of 800 °C. But for MBC, no impurity phases (including C containing secondary phases) other than MgO are detected. The MBS shows Mg_2Si and traces of unreacted SiC as impurity phases and the presence of Mg_2Si confirms the dissociation of SiC which is consistent with earlier works [41]. While the dissociated Si reacts with Mg to form Mg_2Si , the remaining free C is incorporated into the MgB_2 lattice. The XRD pattern of

MBR shows Mg₂Si and MgO as main impurity phases wherein the MgO content is much higher compared to the other doped samples. Hence, it is clear that SiO₂ contained in BRH reacts with Mg to form Mg₂Si and MgO and the remaining C substitutes at B site.

For all doped samples, the (110) peak of MgB₂ which is related to the in-plane lattice constant shifts to higher angles, which shows a decrease in lattice parameter a indicating that substitution of C atom into the B site has occurred. On the other hand, the (002) peaks undergo a relatively small shift. This means that the lattice parameter c does not vary significantly within the range of dopants studied but the lattice parameter a decreases when these dopants are added. The lattice parameter a of the hexagonal structure of MgB₂ are calculated and tabulated in *table 4.2*. As can be seen, among all the doped samples the lattice parameter a is decreased to a maximum extent for the MBC whereas it is the least for MBD. However, in the case of MBS and MBR, the value of a is comparable to that of MBC. This implies that the level of substituted C is highest in the case of MBC, MBS and MBR samples while it is lesser for MBD at identical processing conditions. The decrease of a axis is an indication of the C substitution for B, which is further proven by the depression of the T_c of all the doped samples. It is expected that C, which has one more electron than B, will donate electrons to the σ band. Also, an increase of impurity scattering within the π band and the modification of band structure are achieved by C substitution [42, 43].

Table 4.2 shows the full width at half maximum (FWHM) of (100), (101), (002) and (110) peaks of carbon variants doped and undoped MgB₂ samples. It is seen that the values of the FWHM sharply vary from pure to doped samples except for (002) peak. Since (100) and (110) peaks reflect the in-plane lattice constant of honeycomb boron lattice, the broadening of these peaks suggests the occurrence of some distortion in the lattice due to C substitution at B site. This result is consistent with the earlier reports in which the FWHM of these peaks has a positive correlation with the H_{irr} of MgB₂, i.e. H_{irr} increases with increasing FWHM [44, 45]. Since the honeycomb boron lattice is responsible for superconductivity in MgB₂, the distortion results in the impurity induced scattering of charge carriers and

distortion results in the impurity induced scattering of charge carriers and thus enhances critical field through a reduction of coherence length. But the out-of-plane FWHM of (002) is practically independent of carbon dopants. These results strongly indicate that the in-plane structure was selectively disordered by the C substitution at B site. It may be noted that a decrease in grain size could also result in peak broadening.

Table 4.2: Structural properties of pure and carbon variants doped MgB_2 samples

Samples	Lattice parameters (nm)		FWHM (degree)			
	<i>a</i>	<i>c</i>	(100)	(101)	(002)	(110)
MB	0.3087	0.3519	0.155	0.207	0.239	0.215
MBD	0.3078	0.3523	0.242	0.374	0.301	0.403
MBC	0.3074	0.3519	0.289	0.390	0.290	0.468
MBS	0.3076	0.3525	0.319	0.451	0.280	0.456
MBR	0.3075	0.3521	0.267	0.372	0.318	0.449

Figure 4.14 shows SEM images of the fractured surfaces of the undoped and carbon variants doped MgB_2 samples. The undoped sample shows a homogenous microstructure with tiny and well packed hexagonal grains of average size 1 μm where grain boundaries are sharp and clear. In MBC and MBR samples, the grains are found to be more packed with increasing density of grain boundaries whereas MBD and MBS samples show a homogenous mixture of smaller and larger grains. The smaller grain size will increase the density of grain boundaries thereby enhancing the flux pinning property and $J_C(H)$ characteristics of doped samples. Figure 4.14(f) shows HRTEM micrograph and corresponding EDX analysis of MBR. It is clear that the impurities in the BRH doped sample is homogeneously distributed within the MgB_2 grains. These uniformly distributed impurities with size (~ 10 nm) comparable to the coherence length of MgB_2 can pin the flux lines within the grains. EDX analysis reveals that the intragrain impurities are Mg, B, C, Si and O (The excessive peak intensity in respect of C is due to the additional contribution from the carbon present in the

sample grid). This finding supports the XRD result that the secondary phases/inclusions are Mg_2Si and MgO . These intragrain nano sized inclusions and the crystal defects created by C substitution act as strong pinning centers and are responsible for the improved flux pinning in the BRH doped sample.

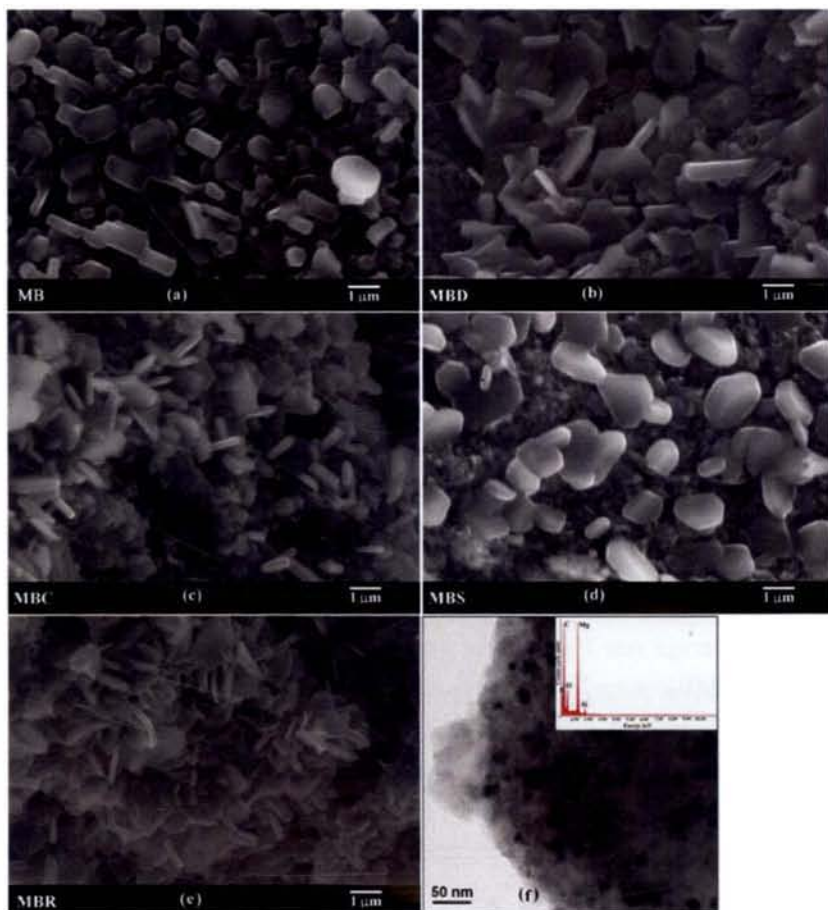


Figure 4.14: (a)-(e) SEM images of pure and carbon variants doped MgB_2 samples. (f) HRTEM image of MBR sample (inset shows EDX analysis of the same sample)

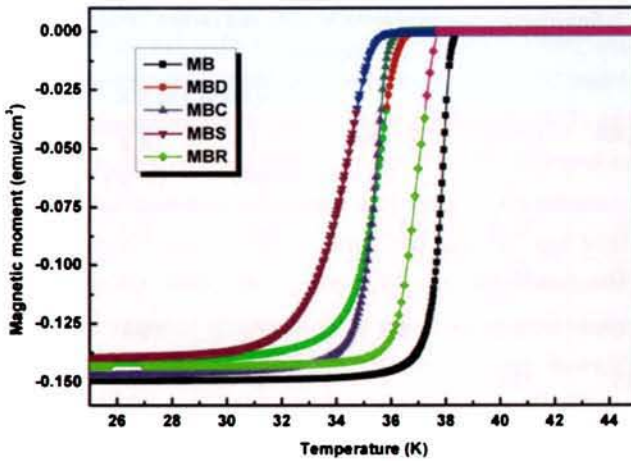
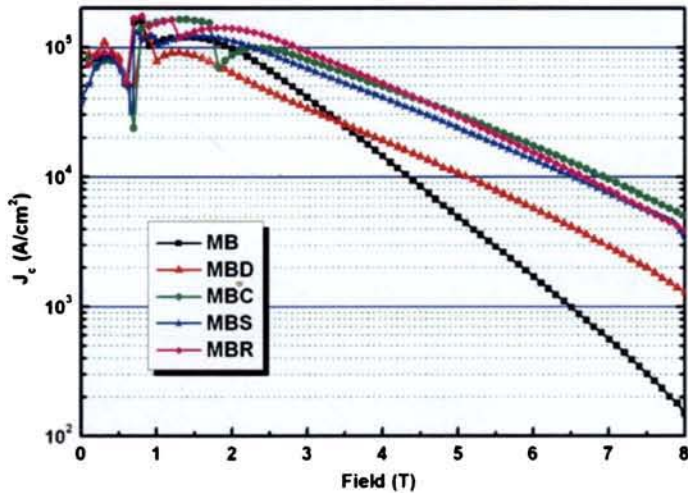


Figure 4.15: DC magnetic moment versus temperature plots for pure and carbon variants doped MgB_2 samples

Temperature dependence of zero field cooled magnetization values ($M-T$) for the undoped and doped samples are shown in figure 4.15. T_C is defined as the onset temperature at which the samples exhibit diamagnetic properties and the measured values of T_C are tabulated in table 4.3. As shown in table, the undoped sample has a T_C of 38.6 K which decreases by 1-3 K in doped samples. This is expected due to the C substitution at the B site. The substitution of C at the B site reduces the hole concentration and causes changes in the phonon modes. The reduced density of states and weakened electron-phonon coupling are the reasons for T_C reduction in the doped samples. The decrease is more in the case of MBS compared to MBC and MBD. The unreacted Mg in case of n-D and unreacted SiC and Mg_2Si in case of n-SiC doped samples are also responsible for T_C decrease in the doped samples. ΔT_C of the samples is also determined and tabulated in table 4.3. The undoped sample has a ΔT_C of 1 K, which increases to 1.3-2.1 K for the doped samples. Among the doped samples, the MBR and MBC samples show lower ΔT_C values. The comparatively higher ΔT_C of other doped samples indicates that both C substitution and the presence of non-superconducting phases reduce crystallinity and sample homogeneity, as seen in XRD.

Table 4.3: Superconducting properties of pure and carbon variants doped MgB_2 samples

Samples	T_C (K)	ΔT_C (K)	J_C (A/cm ²) at 5 K		F_{Pmax} (GN/m ³)
			4 T ($\times 10^4$)	8 T ($\times 10^3$)	
MB	38.6	1.0	1.4	0.1	1.9
MBD	36.7	2.0	1.9	1.4	1.3
MBC	36.3	1.3	4.9	5.1	2.5
MBS	35.8	2.1	3.6	4.9	2.3
MBR	37.7	1.0	5.2	4.0	3.0

**Figure 4.16: $J_C(H)$ curves of pure and carbon variants doped MgB_2 samples**

The magnetic field dependence of J_C , calculated from magnetic hysteresis measurements at 5 K for all samples is illustrated in figure 4.16. J_C jumps abruptly at lower fields due to the flux jump. For the undoped sample, J_C drops rapidly in the presence of magnetic field but, at higher fields, all the doped samples show significant enhancement in $J_C(H)$ behavior with respect to the pure sample. For MBD, J_C value is much lower when compared with the other doped samples. This implies that at lower

fields, the presence of excess Mg (as seen in XRD) reduces the J_C and at higher fields, the partial substitution of C gives moderately higher J_C as compared to pure sample. Of all the doped samples, MBC and MBR give the best J_C performance up to the maximum field studied (8 T) and the level of J_C enhancement is around 50 times greater than the undoped sample at 5 K (8 T). MBS also shows considerably improved $J_C(H)$ behavior at higher fields, but it exhibits lower J_C values compared to MBC and MBR at lower fields. This implies that the secondary non-superconducting phases observed in these samples affect the grain connectivity and hinder the flow of super current at lower fields. The contribution towards the J_C enhancement in MBS and MBR comes partly due to C substitution and partly due to the presence of reacted phase Mg_2Si as flux pinners. But for MBC, C substitution solely is the reason for significant enhancement of J_C at higher fields.

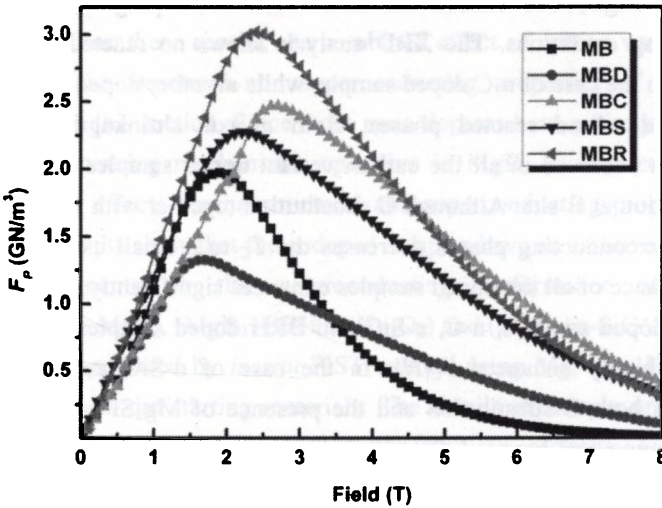


Figure 4.17: $F_p(H)$ curves for the pure and carbon variants doped MgB_2 samples

Figure 4.17 shows the bulk $F_p(H)$ curves of the pure and carbon variants doped MgB_2 samples. Since the flux jumps show significant marks on the shape of the curves, the curves are plotted after refining the $J_C(H)$ data up to 2 T. Here, the F_p of the sample doped with BRH is significantly enhanced for the entire field of study as compared to pure and other doped

samples and the maximum flux pinning force density (F_{Pmax}) for MBR is 3 GN/m³ (table 4.3). It is also observed that the C substitution at B site causes a shift in F_{Pmax} of all the doped samples towards high field, except for MBD. In MBR, both C substitution at the B site and the reaction induced secondary phase Mg₂Si contribute to further pinning and these are the main reasons for the significant enhancement in F_P and hence $J_C(H)$ performance. The F_P of MBC also shows significant enhancement at higher fields and here C substitution is solely the reason for flux pinning. In the case of MBS, both C substitution and the presence of Mg₂Si are the reasons for the enhancement of flux pinning at higher fields. Among all the doped samples, MBD shows poor flux pinning behavior due to the low reactivity of n-D.

4.5.3: Conclusion

A comparative study on the effect of doping of n-D, n-C, n-SiC and BRH in MgB₂ was carried out under identical doping levels of C and processing conditions. The XRD analysis shows no reacted or unreacted phases in the case of n-C doped sample, while all other doped samples show unreacted or/and reacted phases. Both *a* axis shrinkage and FWHM variation observed in all the carbon variant doped samples confirm the C substitution at B site. Although C substitution together with the presence of non-superconducting phases decreases the T_C to a small extent, the $J_C(H)$ performance of all the doped samples enhances significantly. On comparing all the doped samples, n-C, n-SiC and BRH doped samples competitively exhibit highly enhanced $J_C(H)$. In the case of n-SiC and BRH doped samples, both C substitution and the presence of Mg₂Si causes enhanced flux pinning and hence $J_C(H)$, while for n-C doped one C substitution is solely the reason. The present work also shows that BRH is an inexpensive, promising and alternate candidate for n-C and n-SiC.

4.6: Codoped MgB₂: An effective method for enhancing the in-field critical current density of MgB₂

4.6.1: Introduction

Based on the nature of the dopant/additive, it can cause substitution at Mg/B site, or react with Mg/B to form reacted secondary phases or can be

incorporated in the superconductor matrix as inclusions without any chemical reaction. Addition of carbon containing compounds causes substitution of C at B site in the boron planes which modifies the σ and π band scattering and enhances the H_{C2} of MgB_2 significantly. The lattice distortions, defects and strains caused by C substitution improve the flux pinning strength and in-field critical current density. From the comparative study of carbon variants (as described in section 4.5), n-C, n-SiC and BRH doped MgB_2 samples are found to exhibit enhanced flux pinning and J_C both at lower and higher fields, competitively. Besides these carbon variants, addition of nano oxides such as Tb_4O_7 , Ho_2O_3 and SiO_2 are also found to increase flux pinning and critical current considerably, as seen in section 4.4. Of these, Ho_2O_3 causes the formation of HoB_4 as the reacted impurity phase, which interacts more strongly with the flux lines. Hence, n- Ho_2O_3 doped sample exhibits better flux pinning behavior and thereby $J_C(H)$ performance.

Based on these results, the combined effect of carbon variants and n- Ho_2O_3 on the structural and superconducting properties of MgB_2 is investigated in this section. Since these nano dopants have entirely different reaction/flux pinning mechanisms operative in MgB_2 , it is interesting to compare their effects on the structural and superconducting properties of MgB_2 . Our results show that the codoped samples have an additive effect of both the dopants on the superconducting performance of MgB_2 . Polycrystalline MgB_2 , ($MgB_2+BRH+n-Ho_2O_3$) and ($MgB_2+n-SiC+n-Ho_2O_3$) samples were prepared by *in situ* PIST method using Mg, B, n- Ho_2O_3 , n-SiC and BRH as the starting materials. The details of sample preparation and characterizations are discussed in the previous sections. The MgB_2 samples pure, ($MgB_2+n-Ho_2O_3$), (MgB_2+BRH), ($MgB_2+n-SiC$), ($MgB_2+n-Ho_2O_3+BRH$) and ($MgB_2+n-Ho_2O_3+n-SiC$) are named as MB, MBHo, MBR, MBS, MBHR and MBHS respectively.

4.6.2: Results and discussion

The XRD patterns of pure and codoped MgB_2 samples are shown in figure 4.18. In the case of pure MgB_2 , all characteristic peaks are obtained with a trace amount of MgO. The MgO formation is due to the entrapped air

before the end sealing of the tubes and it slightly increases with the addition of BRH and $n-Ho_2O_3$. Mg_2Si phase is formed in MBHS which confirms the dissociation of SiC and it is consistent with the result obtained for monodoping of $n-SiC$. The dissociated Si reacts with Mg to form Mg_2Si and the free C is incorporated into the MgB_2 lattice. In MBHR sample, XRD pattern also shows Mg_2Si and MgO as main impurity phases wherein the MgO content is much higher compared to the other doped samples. Hence, it is clear that SiO_2 contained in BRH reacts with Mg to form Mg_2Si and MgO and the remaining C substitutes at B site. The presence of HoB_4 phase and the absence of residual Ho_2O_3 in both MBHR and MBHS indicate that the added Ho_2O_3 completely decomposes and reacts with B to form HoB_4 . The codoped samples show both the reacted phases Mg_2Si and HoB_4 and these are found to have significant role in the enhancement of the flux pinning property of MgB_2 .

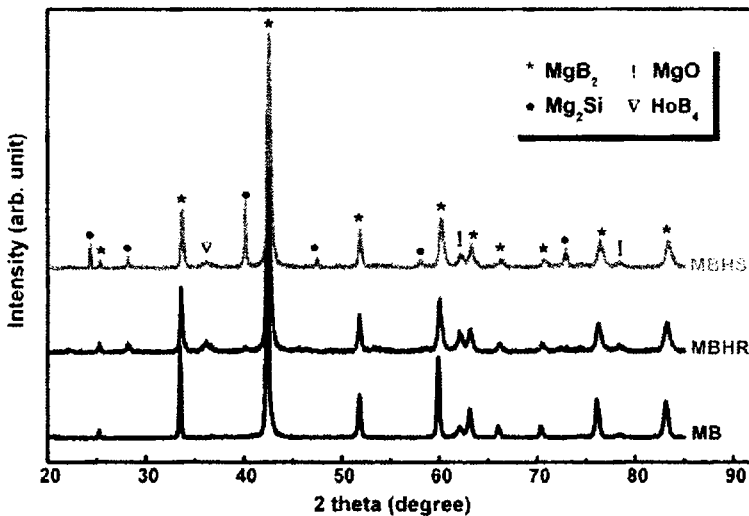


Figure 4.18: XRD patterns of pure and codoped MgB_2 samples

It is clearly observed that the position of (110) peak slightly shifts to higher angles for codoped samples, indicating a decrease in the lattice parameter a . While, there is no shift in the (002) peak of any of the samples suggesting that there is no measurable change in the lattice parameter c . This means that the lattice parameter c does not vary significantly within the

range of dopants studied, but the lattice parameter a decreases. The lattice parameter a of MgB₂ and its doped variants are calculated and tabulated in table 4.4. Compared to pure sample lattice parameter a is found to be decreasing for all the codoped samples. The decrease of a is an indication of the C substitution at B site which is further proved by the depression of T_c in codoped samples.

Table 4.4: Structural properties of pure and carbon variants doped MgB₂ samples

Samples	Lattice parameters (nm)		FWHM (degree)			
	a	c	(100)	(101)	(002)	(110)
MB	0.3087	0.3519	0.155	0.207	0.239	0.215
MBHR	0.3078	0.3526	0.261	0.348	0.341	0.415
MBHS	0.3073	0.3515	0.259	0.336	0.288	0.398

From the XRD, typical FWHM values of the MgB₂ peaks which represent peak broadening are given in table 4.4. The X-ray peak broadening is influenced by both crystallite size and lattice strain. The FWHM of all the codoped samples are found to be broadened as compared to pure MgB₂ sample. As in the case of lattice parameter a , here also C substitution has dominant role in enhancing the peak broadening. Since (100) and (110) peaks reflect the in-plane lattice constant of honeycomb boron lattice, the broadening of these peaks suggests the occurrence of some distortion in the lattice as a result of C substitution at B site. As the honeycomb boron lattice is responsible for superconductivity in MgB₂, the distortion results in the impurity induced scattering of charge carriers and thus enhances critical field through a reduction of coherence length.

To analyze the effect of grain size on peak broadening and observe the morphological features, microstructural examination was carried out using SEM. Figure 4.19 (a) and (b) shows the SEM images of the fractured surfaces of the MBHR and MBHS codoped samples. These samples show similar microstructure with randomly oriented and tightly packed flaky hexagonal grains. Figure 4.19 (c) and (d) show the TEM images of these

samples. The impurities in these codoped samples are clearly visible and are distributed within the MgB_2 grains. These nano size (~ 20 nm) impurities with size comparable to the coherence length of MgB_2 can pin the flux lines within the grains.

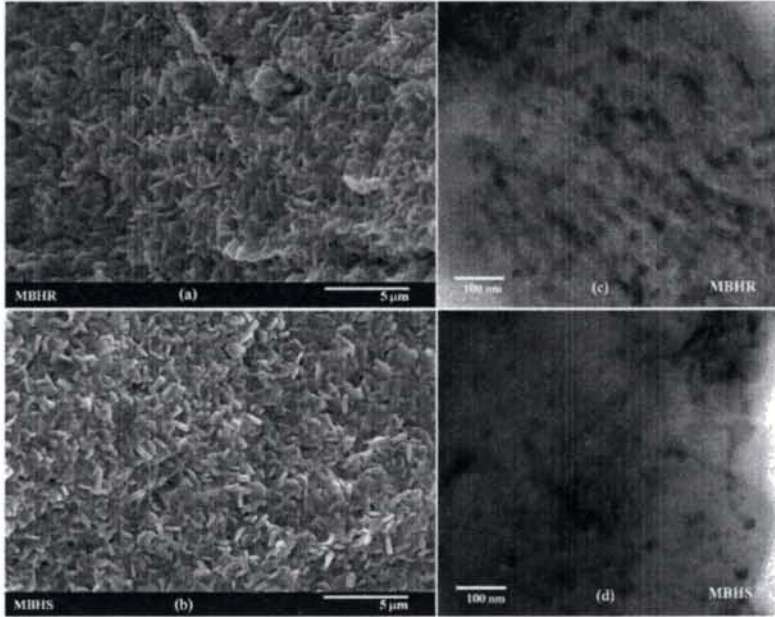


Figure 4.19: (a)-(b) SEM and (c)-(d) TEM images of codoped MgB_2

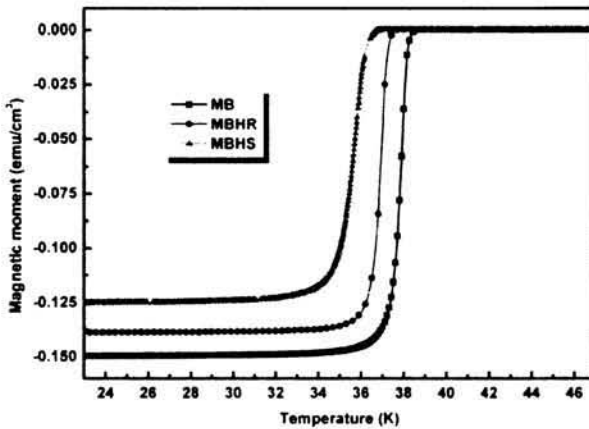


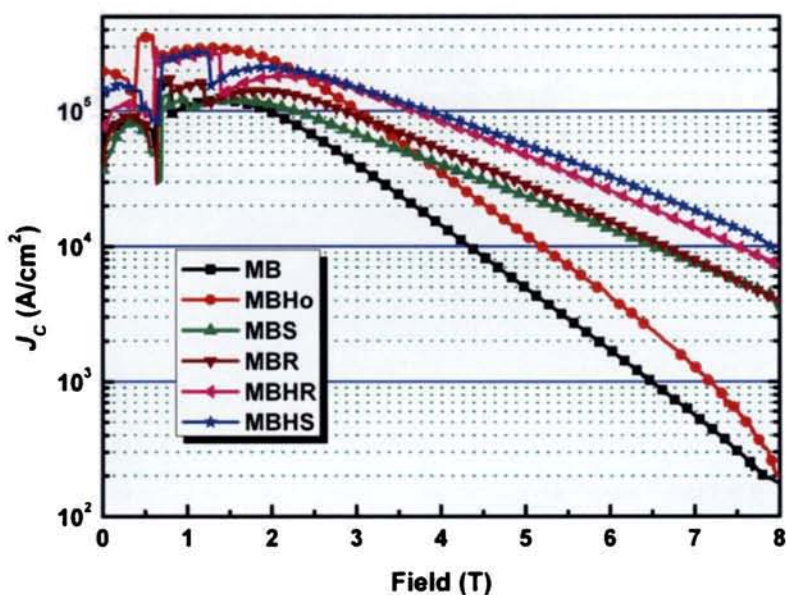
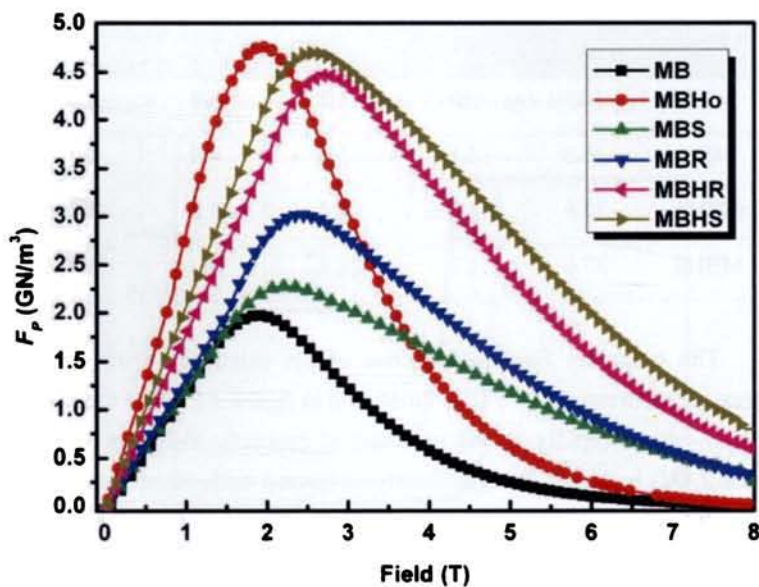
Figure 4.20: Temperature dependence of DC magnetization plots for pure and codoped MgB_2 samples

Temperature dependence of zero field cooled magnetization values for the undoped and codoped samples are shown in *figure 4.20*. *Table 4.5* shows a comparison of superconducting properties of pure, monodoped and codoped MgB₂ samples. All the doped samples show a reduction in T_C as compared to pure sample. C substitution together with the presence of non-superconducting phases decreases the T_C in doped samples, while for MBHo sample the presence of reacted phase alone is the reason for T_C reduction. The ΔT_C of superconducting transition of all the samples are also tabulated. The comparatively higher ΔT_C of MBS indicates that both C substitution due to SiC addition and the presence of non-superconducting reacted phases such as Mg₂Si reduce crystallinity and sample homogeneity.

Table 4.5: Comparison of superconducting properties of pure, monodoped and codoped MgB₂

Samples	T_C (K)	ΔT_C (K)	J_C (A/cm ²) at 5 K		F_{Pmax} (GN/m ³)
			4 T ($\times 10^4$)	8 T ($\times 10^3$)	
MB	38.6	1.0	1.4	0.1	1.9
MBHo	38.1	1.0	3.5	0.1	4.8
MBR	37.7	1.0	5.2	4.0	3.0
MBS	35.8	2.1	3.6	4.9	2.3
MBHR	37.6	1.2	8.4	7.2	4.5
MBHS	37.0	1.7	9.3	10.1	4.7

The magnetic field dependence of J_C , calculated from magnetic hysteresis measurements at 5 K is illustrated in *figure 4.21*. For the undoped sample, J_C drops rapidly in the presence of magnetic field but for doped samples $J_C(H)$ behavior is significantly enhanced with respect to the pure sample throughout the entire range of field studied. Of all the doped samples, the codoped samples MBHR and MBHS give the best performance and the level of J_C enhancement is around two times greater than their corresponding monodoped sample at 5 K and 8 T. The monodoped n-Ho₂O₃

Figure 4.21: $J_c(H)$ curves of pure, monodoped and codoped MgB_2 samplesFigure 4.22: $F_p(H)$ curves for the pure, monodoped and codoped MgB_2 samples

itself exhibits enhanced in-field J_C compared to pure sample. The contribution towards the J_C enhancement of n-SiC and BRH monodoped samples, comes partly from C substitution and partly due to the presence of reacted phases as flux pinners. For the codoped sample MBHS, both these effects, i.e. substitution due to C and flux pinning due to the reacted phases like Mg_2Si and HoB_4 contribute to the strong enhancement of J_C . Combined addition of n- Ho_2O_3 with BRH is also found to be much effective for the enhancement of $J_C(H)$ of MgB_2 than the solo addition of any one of the additives. The substitution of C at B site by BRH and the formation of magnetic particles of HoB_4 by Ho_2O_3 are the reasons for the strong improvement of $J_C(H)$ in this sample.

Figure 4.22 shows the bulk $F_p(H)$ curves of the pure, monodoped and codoped MgB_2 samples. Since the flux jumps show significant marks on the shape of the $F_p(H)$ curves, the curves are plotted after refining the $J_C(H)$ data up to 2 T. It can be observed that the flux pinning behavior and F_{Pmax} values of all the doped samples have improved appreciably. Moreover, a peak shift of F_{Pmax} towards high field is observed for all the doped samples except MBHo. This is because all the doped samples except MBHo undergo C substitution at B site. At fields above F_{Pmax} , both the codoped samples exhibit excellent flux pinning behavior due to the additive effect of n- Ho_2O_3 and corresponding carbon variants. From this, it can be concluded that combined addition of Ho_2O_3 with BRH and n-SiC was found to be much more effective than their solo addition for the enhancement in flux pinning and hence $J_C(H)$ performance of MgB_2 .

4.6.3: Conclusion

The effect of combined addition of n- Ho_2O_3 with carbon variants, namely n-SiC and BRH on MgB_2 was investigated and its superconducting properties were compared to pure and its monodoped samples. The variations in both a lattice parameter and FWHM imply that in codoped samples C is more effectively substituted at B site, which results local strains in MgB_2 lattice and the depression of T_C also supports this. The $J_C(H)$ is significantly enhanced for all monodoped and codoped samples compared with the pure sample among which the codoped samples exhibit

the best performance in flux pinning and J_C enhancement. The C substitution at B site by carbon dopants and the formation of Mg₂Si and magnetic particles like HoB₄ by Ho₂O₃ as flux pinners are the reasons for the strong improvement of $J_C(H)$ in these samples.

4.7: Summary

The influence of processing temperature and various nano dopants on the structural and superconducting properties of bulk MgB₂ superconductor prepared by *in situ* PIST method was studied. The samples heat treated at relatively lower temperatures particularly at 800 °C showed enhanced flux pinning as compared to those processed at higher temperatures. The reduced grain size and hence increased grain boundary is the main reason behind the improved flux pinning and $J_C(H)$ for the samples sintered at lower temperatures. In the comparative study of nano oxide doped MgB₂ samples, the $J_C(H)$ performance is significantly enhanced for all the doped samples. The addition induced reacted phases act as strong flux pinners thereby improving the $J_C(H)$ and H_{irr} of the nano oxide doped samples. Flux pinning analysis also confirms the same, where n-Ho₂O₃ doped MgB₂ sample shows the maximum flux pinning behavior in the entire field of study because of the presence of magnetic impurities like HoB₄ as strong flux pinners. On comparing all the carbon variants doped samples, the n-C, n-SiC and BRH doped samples competitively exhibit highly enhanced $J_C(H)$. In the case of n-SiC and BRH doped samples, both C substitution and the presence of Mg₂Si cause enhanced flux pinning and hence $J_C(H)$ while for n-C doped one C substitution is solely the reason. The codoping of n-Ho₂O₃ with n-SiC and BRH exhibit excellent performance in flux pinning and J_C enhancement up to a field of 8 T as compared to pure sample and their corresponding monodoped samples. The C substitution at B site by carbon dopants and the formation of Mg₂Si and magnetic particles like HoB₄ by Ho₂O₃ as flux pinners are the reasons for the strong improvement of $J_C(H)$ in these samples.

References:

1. C. Buzea and K. Robbie, *Supercond. Sci. Technol.* 18, R1 (2005)
2. K. Vinod, R. G. Abhilash Kumar, and U. Syamaprasad, *Supercond. Sci. Technol.* 20, R1 (2007)
3. Y. Bugoslavsky, L. F. Cohen, G. K. Perkins, M. Polichetti, T. J. Tate, R. Gwilliam and A. D. Caplin, *Nature* 411, 561 (2001)
4. A. Durán, E. Verdín, D. H. Galvan, C. Romero-Salazar, F. Morales, E. Adem, J. Rickards, M. B. Maple and R. Escudero, *J. Appl. Phys.* 104, 093917 (2008)
5. Y. Ma, A. Xu, X. Li, X. Zhang, S. Awaji and K. Watanabe, *Japan. J. Appl. Phys.* 45, L493 (2006)
6. S. X. Dou *et al.*, *Phys. Rev. Lett.* 98, 097002 (2007)
7. H. Kumakura, H. Kitauchi, A. Matsumoto and H. Hatakeyama, *Appl. Phys. Lett.* 84, 3669 (2004)
8. G. Serrano, A. Serquis, S. X. Dou, S. Soltanian, L. Civale, B. Maiorov, T. G. Holesinger, F. Balakirev and M. Jaime, *J. Appl. Phys.* 103, 023907 (2008)
9. R.G. Abhilashkumar, K. Vinod, R.P. Aloysius and U. Syamaprasad, *Mater. Lett.* 60, 3328 (2006)
10. Neson Varghese, K. Vinod, Ashok Rao, Y.K. Kuo, and U. Syamaprasad, *J. Alloys Compd* 470, 63 (2009)
11. H. Kitaguchi, A. Matsumoto, H. Hatakeyama and H. Kumakura, *Supercond. Sci. Technol.* 17, S486 (2004)
12. A. Serquis, L. Civale, D. L. Hammon, J. Y. Coulter, X. Z. Liao, Y. T. Zhu, D. E. Peterson and F. M. Mueller, *Appl. Phys. Lett.* 82, 1754 (2003)
13. H. Suo, C. Beneduce, M. Dhallé, N. Musolino, J. Genoud and R. Flükiger, *Appl. Phys. Lett.* 79, 3116 (2001)
14. W. Goldacker, S. I. Schlachter, B. Obst and M. Eisterer, *Supercond. Sci. Technol.* 17, S490 (2004)
15. Y. Feng, G. Yan, Y. Zhao, C. F. Liu, X. H. Liu, P. X. Zhang, L. Zhou, A. Sulpice, E. Mossang and B. Hebra, *J. Phys.: Condens. Matter* 16, 1803 (2004)
16. E. Martínez, L. A. Angurel and R. Navarro, *Supercond. Sci. Technol.* 15, 1043 (2002)

17. S. Hata, T. Yoshidome, H. Sosiati, Y. Tomokiyo, N. Kuwano, A. Matsumoto, H. Kitaguchi and H. Kumakura, *Supercond. Sci. Technol.* 19, 161 (2006)
18. R. Zeng, L. Lu, J. L. Wang, J. Horvat, W. X. Li, D. Q. Shi, S. X. Dou, M. Tomsic and M. Rindfleisch, *Supercond. Sci. Technol.* 20, L43 (2007)
19. P. C. Canfield, S. L. Budko and D. K. Finnemore, *Physica C* 385, 1 (2003)
20. S. Ueda, J. Shimoyama, A. Yamamoto, S. Horii and K. Kishio, *Supercond. Sci. Technol.* 17, 926 (2004)
21. S. K. Chen., Z. Lockman, M. Wei, B. A. Glowacki and J. L. M. Driscoll, *Appl. Phys. Lett.* 86, 24250 (2005)
22. T. A. Prikhna, W. Gawalek, Y. M. Savchuk, V. E. Moshchil, N. V. Sergienko, A. B. Surzhenko, M. Wendt, S. N. Dub, V. S. Melnikov, C. Schmidt and P. A. Nagorny, *Physica C* 386, 565 (2003)
23. M. Dhalle, P. Toulemonde, C. Beneduce, N. Musolino, M. Decroux and R. Flukiger, *Physica C* 363, 155 (2001)
24. Handstein, D. Hinz, G. Fuchs, K. H. Muller, K. Nenkov, O. Gutfleisch, V. N. Narozhnyi and L. Schultz, *J. Alloys Comp.* 329, 285 (2001)
25. X. L. Wang, S. Soltanian, M. James, M. J. Qin, J. Horvat, Q. W. Yao, H. K. Liu and S. X. Dou, *Physica C* 408, 63 (2004)
26. E. Martinez, P. Mikheenko, M. Martinez-Lopez, A. Millan, A. Bevan and J. S. Abell, *Phys. Rev. B* 75, 134515 (2007)
27. P Mikheenkol, E Martínez, A Bevan, J S Abell and J L MacManus-Driscoll, *Supercond. Sci. Technol.* 20, S264 (2007)
28. C.P. Bean, *Phys. Rev. Lett.* 8, 250 (1962)
29. P. W. Anderson, *Phys. Rev.* 124, 41 (1961)
30. J. Wang, Y. Bugoslavsky, A. Berenov, L. Cowey, A. D. Caplin, L. F. Cohen, J. L. Mac Manus Driscoll, L. D. Cooley, X. Song and D. C. Larbalestier, *Appl. Phys. Lett.* 81, 2026 (2002)
31. S. K. Chen, M. Wei and J. L. Mac Manus Driscoll, *Appl. Phys. Lett.* 88, 192512 (2006)
32. C. Cheng and Y. Zhao, *Appl. Phys. Lett.* 89, 252501 (2006)

33. X. F. Pan, T. M. Shen, G. Li, C. H. Cheng and Y. Zhao, *Phys. Status Solidi (a)* 204, 1555 (2007)
34. K. Vinod, Neson Varghese, U. Syamaprasad, Shipra and A. Sundaresan *Supercond. Sci. Technol.* 21, 025003 (2008)
35. N. Ojha, G. D. Varma, H. K. Singh and V. P. S. Awana, *J. Appl. Phys.* 105, 07E315 (2009)
36. H. Yamada, M. Hirakawa, H. Kumakura and H. Kitaguchi, *Supercond. Sci. Technol.* 19, 175 (2006)
37. R. A. Ribeiro, S. L. Bud'ko, C. Petrovic and P. C. Canfield, *Physica C* 384, 227 (2003)
38. P. C. Canfield and G. W. Crabtree, *Phys. Today* 56, 34 (2003)
39. Neson Varghese, K. Vinod, S. Rahul, P. Anees, K. M. Devadas, Syju Thomas, Shipra, A. Sundaresan, S. B. Roy and U. Syamaprasad, *J. Am. Ceram. Soc.* 94, 1133 (2011)
40. Neson Varghese, K. Vinod, U. Syamaprasad and S. B. Roy, *J. Alloys Comp.* 484, 734 (2009)
41. W. K. Yeoh, and S. X. Dou, *Physica C* 456, 170 (2007)
42. M. Avdeev, J. D. Jorgensen, R. A. Ribeiro, S. L. Bud'ko and P. C. Canfield, *Physica C* 387, 301 (2003)
43. Y. Ma, X. Zhang, A. Xu, X. Li, L. Xiao, G. Nishijima, S. Awaji, K. Watanabe, Y. Jiao, L. Xiao, X. Bai, K. Wu and H. Wen, *Supercond. Sci. Technol.* 19, 133 (2006).
44. A. Yamamoto, J. Shimoyama, S. Ueda, Y. Katsura, I. Iwayama, S. Horii and K. Kishio, *Appl. Phys. Lett.* 86, 212502 (2005)
45. Y. Zhao, Y. Feng, T. M. Shen, G. Li, Y. Yang and C. H. Cheng, *J. Appl. Phys.* 100, 123902 (2006)

5

OPTIMIZATION OF PROCESSING PARAMETERS AND NOVEL PREPARATION TECHNIQUES FOR MgB_2 WIRES

5.1: Introduction

Impressive progress has been made in the fabrication of MgB_2 wires for practical applications such as magnets and cables, since its discovery. The key to magnet applications of superconductors lies in the rare combination of low cost and a ready wire fabrication route. Due to the recent advances in cryocoolers, many electric utilities have to be optimized at temperatures of 10-35 K, a domain for which MgB_2 could provide the cheapest superconducting wires. Another important advantage of the MgB_2 conductor fabrication compared to the other superconductors is that the formation of MgB_2 phase with better superconducting properties occurs at relatively low temperatures and short durations. The first successful process of MgB_2 wire fabrication, via diffusion of Mg vapor into boron fibers encapsulated in Ta tubes, was reported by Canfield *et al.* [1]. Soon after, many techniques were developed to produce long wires with higher critical current densities (J_C). Among these, powder in tube (PIT) method came out as the most acceptable method for preparation of good quality wires in long length. Based on this method, certain groups [2-4] followed the so called *ex situ* technique, while majority [5-8] preferred to use the *in situ* technique. Though *ex situ* technique is found to be suitable for the development of long conductors with complex multifilamentary wire geometry, the $J_C(H)$ behavior of the *ex situ* conductors has not been as good as the *in situ* ones. Besides this, *in situ* route has several advantages such as low cost, low processing temperature and easiness to dope impurity atoms at Mg/B sites. However, the superconducting properties of *in situ* PIT processed MgB_2 wires strongly depend on the type and quality of precursor powder, chemical compatibility and workability of sheath material, processing temperature and preparation techniques. Therefore, the reactivity of sheath materials with Mg/B, effects of processing temperature, substitution and

addition of impurity atoms and nano dopants and novel preparation techniques such as lowering the processing temperature of MgB₂ and hot-pressing of self-heated MgB₂ wires are studied in detail and discussed in this chapter.

5.2: Influence of reactivity of sheath materials with Mg/B on superconducting properties of MgB₂

5.2.1: Introduction

On considering the fabrication of metal sheathed MgB₂ conductors, the metal sheath should play the role of a diffusion barrier for the volatile and reactive Mg and it must be chemically compatible with Mg/B without any degradation of superconducting properties of MgB₂ core. Moreover, the sheath material must have adequate strength to give mechanical support to the brittle superconducting core and should be ductile enough to withstand the mechanical working. A number of sheath materials viz. Fe, Ni, Cu, Ag, Nb, Ta and SS have been used to fabricate MgB₂ wires [9-16]. Among these, most of them form intermetallics or solid solutions with Mg/B causing reduction in superconducting volume and critical current. Apart from sheath reactivity, sheath materials such as Ag, Nb and Ta are very much expensive. Hence, the effect of the reactivity of commonly used sheath materials such as Cu, Ni, Fe and SS on superconducting properties of MgB₂ was investigated to understand the chemical compatibility of these sheath materials for preparation of MgB₂ wires.

The samples were prepared by *in situ* PIST method as detailed in the previous chapters. Stoichiometrically weighed Mg, amorphous B and 10 wt% of sheath material powder (Cu, Ni, Fe and SS of size <75 μm) were uniformly mixed, then packed into the SS tubes and heat treated at different temperatures. SS tube was chosen as the sheath material because of its relatively better chemical stability and mechanical strength at elevated temperatures. The XRD analysis of the above mentioned samples processed at different temperatures showed better result at 825 °C and hence the samples processed at this temperature were chosen for further superconducting measurements. The samples added with Cu, Ni, Fe and SS are labeled as MBCu, MBNi, MBFe and MBSS respectively.

5.2.2: Results and discussion

The results obtained from XRD analysis of MgB₂ added with the powders of various sheath materials processed at different temperatures are summarized in *table 5.1*. 'Pure' phase corresponds to MgB₂ and 'others' corresponds to Mg and MgO for all samples, while 'reacted' phase corresponds to Mg₂Cu/MgCu₂, MgNi_{2.5}B₂ and FeB₂ for MBCu, MBNi and MBFe samples respectively. Semi quantitative phase analysis of the samples was done from XRD data using the formula, Vol% of phase X = $(\Sigma I_X / \Sigma I) \times 100$ where ΣI_X = sum of integrated peak intensities of phase X and ΣI = sum of integrated peak intensities of all phases and the data are given in *table 5.1* for comparison.

Table 5.1: Volume percentage of various phases formed at different processing temperatures for MgB₂ samples added with Cu, Ni, Fe and SS

Samples	Phases	Vol.% of various phases				
		600 °C	675 °C	750 °C	825 °C	900 °C
MBCu	Pure	2.5	7.6	55.9	86.6	75.9
	Reacted	39.9	42.9	41.7	12.7	23.2
	Others	57.6	49.5	2.4	0.7	0.9
MBNi	Pure	2.2	7.2	62.5	59.8	68.8
	Reacted	45.3	43.1	32.8	39.7	30.7
	Others	52.5	49.7	4.7	0.5	0.5
MBFe	Pure	6.5	7.1	87.6	96.2	95.8
	Reacted	0	0	0	0	3.7
	Others	93.5	92.9	12.4	3.8	0.5
MBSS	Pure	3.3	8.6	88.5	97.2	97.2
	Reacted	0	0	0	0	0
	Others	96.7	91.4	11.5	2.8	2.8

In MBCu sample, Mg and Cu reacts even at 600 °C leading to the formation of a binary phase Mg₂Cu. As the reaction temperature is increased to 750 °C, Mg₂Cu undergoes partial decomposition and releases a part of the Mg resulting in the phase formation of MgCu₂. These reactive phases both Mg₂Cu and MgCu₂ reduce the volume of MgB₂ considerably as shown in *table 5.1*. MBNi also shows significant reaction at temperatures as

low as 600 °C causing the formation of Mg_2Ni similar to $MBCu$ samples. At higher temperatures, B also takes part in the reaction process resulting in the formation of a tertiary compound $MgNi_{2.5}B_2$. The rate of this reaction is very fast and hence the reaction consumes significant parts of Mg and B leading to an increase in porosity of the superconducting core and thus lowering the superconducting properties. Thus, both Ni and Cu show distinct reactions with Mg/B even at 600 °C and reduce the amount of MgB_2 noticeably which make them unsuitable for conductor fabrications.

In the case of $MgFe$, Fe remains inert towards both Mg and B at temperatures up to 825 °C. But an intermetallic compound FeB_2 begins to form at around 900 °C due to the reaction of Fe with B. Mg and B are found to be inert in $MBSS$ samples even up to the highest heat treatment temperature of 900 °C, and it may be recalled that SS tubes were used for preparing all the samples in this study. Not even a trace of any reacted phase associated to SS is observed in any of the samples under the extreme heat treatment conditions used. Thus it is confirmed that Fe and SS do not react with Mg or B even up to 825 °C where phase formation of MgB_2 almost completes, suggesting the chemical compatibility of Fe and SS for MgB_2 wire fabrication. Hence, the samples processed at 825 °C were chosen for further detailed investigation.

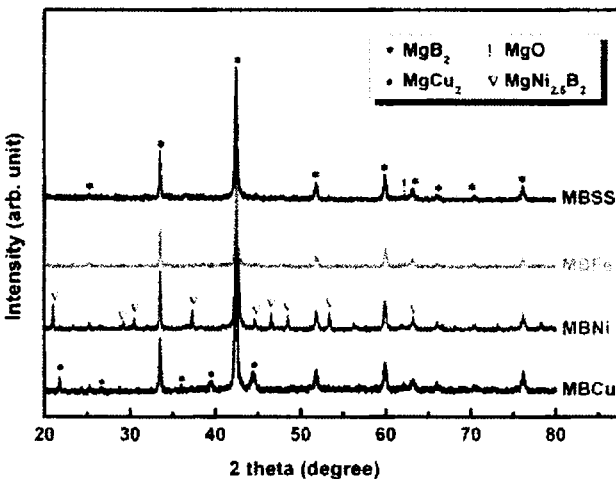


Figure 5.1: XRD patterns of MgB_2 samples added with Cu, Ni, Fe and SS powders processed at 825 °C

Figure 5.1 shows the XRD patterns of samples added with SS, Fe, Cu and Ni sheath powders processed at 825 °C. All X-ray diffraction results give sharp peaks of MgB₂ phase with only a minute fraction of MgO. Absence of any reacted phases of Fe and SS with Mg/B in MBFe and MBSS samples shows their chemical compatibility for wire fabrication, whereas significant quantities of reacted phases such as MgCu₂ and MgNi_{2.5}B₂ are present in MBCu and MBNi respectively. Lattice parameter calculations show that there is no significant variation in lattice parameters of MgB₂ (table 5.2). This indicates that the added sheath materials are not substituted at either Mg or B sites in MgB₂. For the sake of comparison, the lattice parameters, T_C and J_C data for MBCu, MBNi, MBFe and MBSS samples are summarized in table 5.2.

Table 5.2: Lattice parameters, T_C and J_C of MgB₂ added with various sheath materials

Samples	Lattice parameters(nm)		T_C (K)	J_C at 5 K (A/cm ²)	
	<i>a</i>	<i>c</i>		4 T (×10 ⁴)	7 T (×10 ³)
MBCu	0.3084	0.3527	38.3	0.9	0.8
MBNi	0.3086	0.3525	37.8	0.6	0.5
MBFe	0.3089	0.3523	38.5	1.9	5.5
MBSS	0.3086	0.3525	38.2	1.5	3.9

Figure 5.2 illustrates the dc magnetic susceptibility plots in ZFC condition for Cu, Ni, Fe and SS added MgB₂ samples. All the samples show superconducting transitions with T_C in the range 37.8-38.5 K irrespective of the additives. But the near constant values of T_C and the lattice parameters observed clearly point out that the additives do not substitute at either Mg or B sites. Fe added sample shows relatively higher T_C (38.5 K) while T_C of MBSS (38.2 K) and MBCu (38.3 K) are almost the same and that of MBNi sample is slightly lower (37.8 K). The samples MBSS and MBFe exhibit positive magnetization above transition temperature due to the paramagnetic or ferromagnetic nature of the additives.

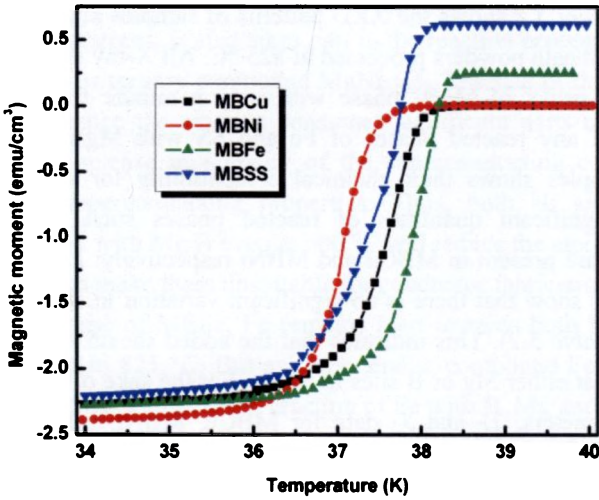


Figure 5.2: DC magnetic susceptibility vs temperature plots of MgB_2 samples added with Cu, Ni, Fe and SS

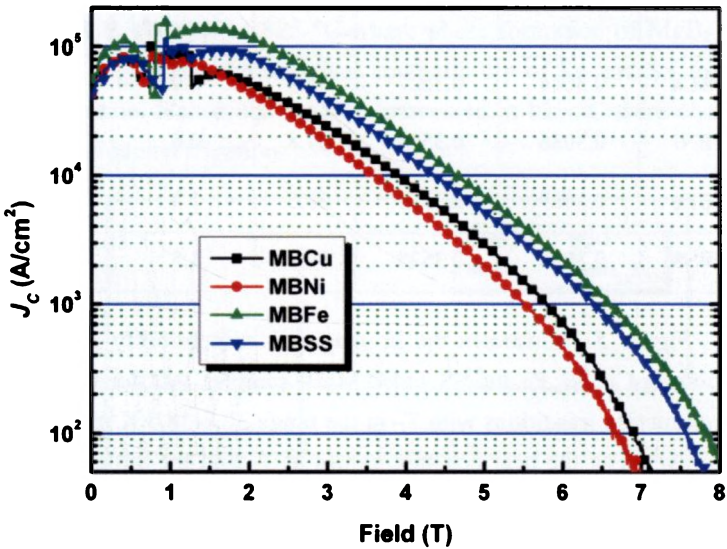


Figure 5.3: $J_c(H)$ curves of MgB_2 samples added with Cu, Ni, Fe and SS

As shown in figure 5.3, $J_c(H)$ characteristics imply that the intragrain J_c of Fe added MgB_2 sample attains better values among all samples. At higher fields, MBSS and MBFe samples show larger J_c than the other samples containing reacted phases, which implies that there is a direct

correlation of J_C with their superconducting core fraction and phase purity. The steep drop in J_C at higher fields in all samples is attributed to the flux penetration into the grain boundaries, which may contain impurities. The weaker grain connectivity and greater flux penetration due to the presence of impurities of reacted sheath powders in the grain boundaries lead to a larger reduction of J_C in MBCu and MBNi samples at higher fields.

5.2.3: Conclusion

The study shows the significant role of the reactivity of sheath material with Mg/B on the phase formation and superconducting properties of MgB₂. Absence of appreciable change in lattice parameters and T_C point out that the additives are not substituted at either Mg or B sites in MgB₂. The additives Cu and Ni react with Mg/B and the reacted phases reduce the volume fraction of superconducting core and impede intergrain connectivity resulting lower J_C at higher fields. On the other hand, Fe and SS added samples give higher volume fraction of MgB₂ core and hence better $J_C(H)$ characteristics which infers that Fe and SS are more suitable as sheath materials in MgB₂ wire fabrication.

5.3: Effect of processing temperature on the transport critical current of MgB₂/Fe superconducting wires

5.3.1: Introduction

Because of the huge difference in the melting points of Mg (650 °C) and B (2080 °C), there is hardly any scope for liquid-liquid reaction between the two; but reactions are feasible for solid-solid, solid-liquid and solid-gas interactions depending on the processing temperature. This in turn has a vital influence on the phase formation, microstructure, density and critical current of the MgB₂ superconductor. Based on various synthesis methods and nature of starting materials, many groups reported [17-18] that a heat treatment of 650-800 °C is required for the preparation of *in situ* MgB₂ wires. In the previous section, the influence of reactivity of different sheath materials such as Cu, Ni, Fe and SS on phase evolution and superconducting properties of MgB₂ has been discussed. Of these, Fe and its alloy SS seem to be the best among the sheath materials studied in achieving high J_C due to their chemical compatibility with Mg and B and

hence Fe is chosen as suitable sheath material for preparing MgB₂ wires due to its better mechanical workability than SS. Usually, heat treatment is done in vacuum or inert atmosphere in order to avoid Mg oxidation. Fabrication of MgB₂ wires would become much easier if the vacuum/inert atmosphere condition could be avoided. Hence, a simple ‘capping technique’ has been introduced for the end sealing of MgB₂ wires so as to heat treat them directly in air. As the processing conditions of bulk synthesis are entirely different from that of wire making, further optimization of the processing temperature is essential for preparing good quality MgB₂ wires with high performance. Therefore, the present chapter investigates the effect of processing temperature on the phase evolution, microstructure and transport critical current of MgB₂/Fe wires. A temperature range of 600-800 °C is chosen for this study.

5.3.2: Preparation and characterization of MgB₂/Fe monofilamentary wires

Fe tubes (OD/ID = 5/3 mm) of length 5 cm were used for the fabrication of short length monofilamentary wires. The tubes were then filled with stoichiometrically weighed and homogeneously mixed Mg+B powder and mechanically compacted. Copper studs were used as plugs to seal the ends of the tubes and both ends were crimped mechanically. The composite tube was then groove rolled down to the desired dimensions typically 1.33 mm and about 1 m in length, without any intermediate annealing. A schematic diagram for the preparation of monofilamentary MgB₂/Fe wires is shown in *figure 5.4* and a photograph of wire rolling process is shown in *figure 5.5*. The rolled monofilamentary wire was then cut into pieces of 10 cm length and these pieces were end sealed before heat treatment in air. The end sealing was done by a ‘capping technique’ where the ends of the conductors were inserted into suitable iron tubes of short length (1.5 cm) and mechanically fixed with the conductor using a hydraulic press. Then, the ends of the Fe tubes were welded using *dc* arc without any flux, by keeping the sample cooled using a wet cloth.

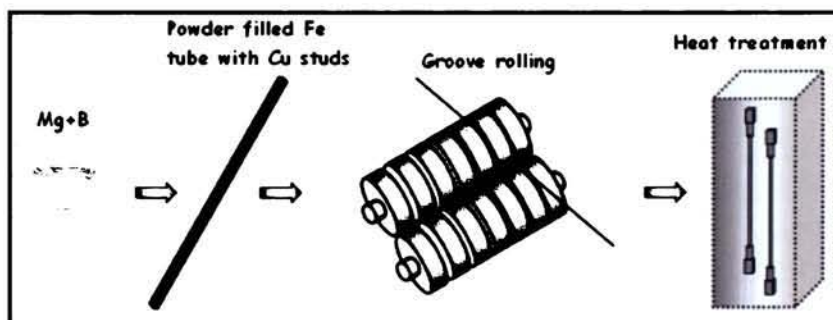


Figure 5.4: A schematic diagram of the preparation procedure of monofilamentary MgB_2 wires

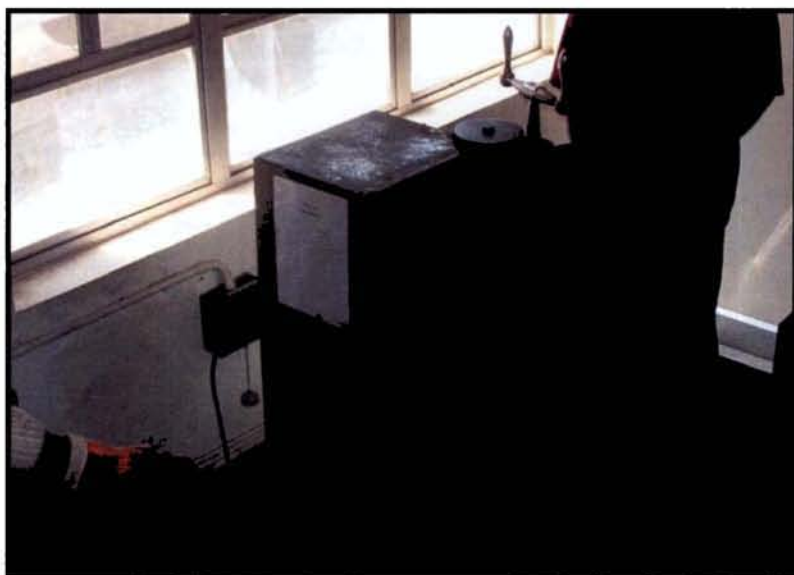


Figure 5.5: Photograph of groove roller and wire rolling

Samples were then heat treated directly in air at desired temperatures in a programmable muffle furnace with a ramp rate of 5 °C/minute and subsequently furnace cooled. The Fe sheathed MgB_2 wire is then used for transport measurements after thoroughly removing the slight layer of FeO. For XRD and SEM analysis, MgB_2 core was taken out by mechanically peeling off the Fe sheath. The samples heat treated at temperatures 600, 625, 650, 675, 700, 750 and 800 °C for 2 hrs are labeled

as MB600, MB625, MB650, MB675, MB700, MB750 and MB800 respectively.

The structural and phase analysis of the samples were performed using an X-ray diffractometer. Phase identification of the samples was performed using X'Pert Highscore Software in support with ICDD PDF II database. The grain morphology and microstructure were examined by SEM. The $R-T$ and $I-V$ measurements were carried out by employing a heavy duty cryocooler interfaced cryostat using dc four probe resistive method with the criterion of $1 \mu V/cm$. The transport J_C was obtained by dividing I_C by the cross sectional area of MgB_2 core.

5.3.3: Results and discussion

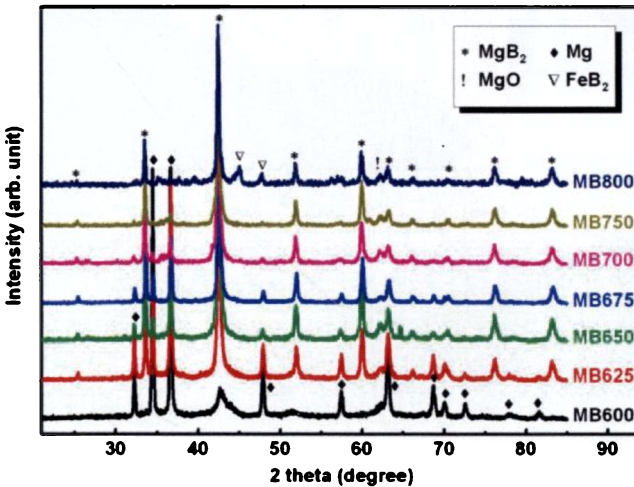


Figure 5.6: XRD pattern of MgB_2 samples processed at different temperatures

Figure 5.6 shows the XRD patterns of MgB_2 monofilamentary wire samples processed at 600-800 °C. Since the formation of MgB_2 starts at 600 °C, the sample heat treated at 600 °C shows lesser amount of MgB_2 and higher amount of unreacted Mg. However, MgB_2 peaks become sharper and stronger and peaks of unreacted Mg decrease as the processing temperature increases which indicate increase in phase purity and crystallinity. On the boron rich side, no peaks of MgB_4 and MgB_{12} phases were detected, which could be ascribed to the successful prevention of Mg evaporation at these heat treatment conditions. Moreover, absence of the peaks corresponding to

Fe and Fe containing compounds up to 750 °C indicates that there is no interfacial reaction occurring between the Fe sheath and Mg/B/MgB₂ at these temperatures. The presence of minor amount of FeB₂ phase in MB800 points out that its formation starts around this temperature. The traces of MgO detected in XRD may be due to the entrapped air in the reaction mixture. From XRD patterns, semi quantitative phase analysis of the samples processed at different temperatures are calculated and tabulated in *table 5.3*. As the processing temperature increases, the volume percentage of MgB₂ increases with a corresponding decrease in Mg. But the sample sintered at 800 °C shows the presence of impurity phases such as FeB₂ and consequently volume percentage of MgB₂ reduces. MgO content is more or less same in all the samples.

Table 5.3: Phase analysis, lattice parameters and T_C of MgB₂ wire samples

Samples	Vol. % of			Lattice parameters (nm)		T_C (K)
	MgB ₂	Mg	Others	<i>a</i>	<i>c</i>	
MB600	7.8	92.2	0	-	-	-
MB625	62.1	36.1	1.8	0.3081	0.3522	36.6
MB650	80.8	16.5	2.7	0.3082	0.3520	37.8
MB675	84.9	12.3	2.8	0.3083	0.3520	37.5
MB700	89.1	7.9	3.0	0.3083	0.3521	37.8
MB750	92.7	4.5	2.8	0.3084	0.3520	38.3
MB800	85.8	1.1	13.1	0.3083	0.3520	37.8

The lattice parameters were calculated from XRD for hexagonal structure and tabulated (*table 5.3*). The samples show no significant variations in lattice parameters, within the experimental error. FWHM of (100), (101), (002) and (110) peaks of the samples processed at different temperatures is shown in *figure 5.7*. FWHM of all the peaks decreases significantly on increasing the sintering temperature indicating the increase in grain size of MgB₂ with temperature. To analyze the effect of grain size on peak broadening, microstructural examination is also carried out using SEM. *Figure 5.8* shows typical SEM images of the fractured MgB₂ core of the wire samples heat treated at 625, 650, 700 and 800 °C. The samples show fine hexagonal and randomly oriented MgB₂ grains with excellent

connectivity. The SEM images also show that the average grain size of the crystalline MgB_2 increases with sintering temperature, well in agreement with the decrease of FWHM from XRD.

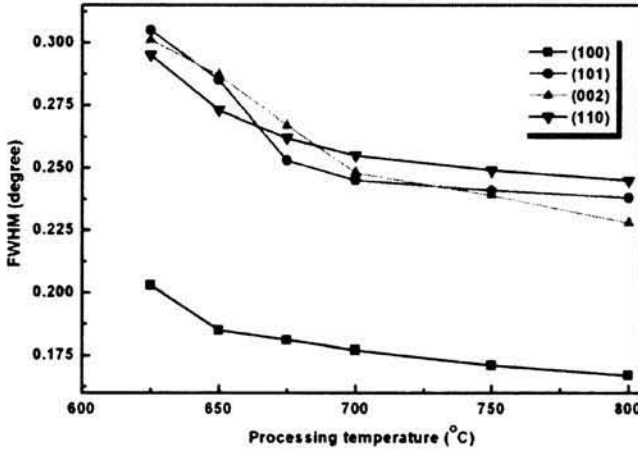


Figure 5.7: Variation of FWHM of the core of the MgB_2/Fe wires with processing temperature

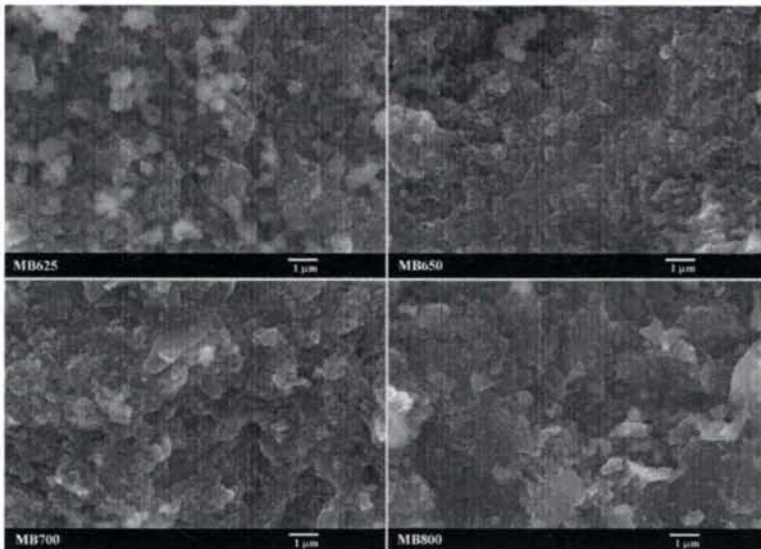


Figure 5.8: Typical SEM images of the core of the MgB_2/Fe wires processed at 625, 650, 700 and 800 °C

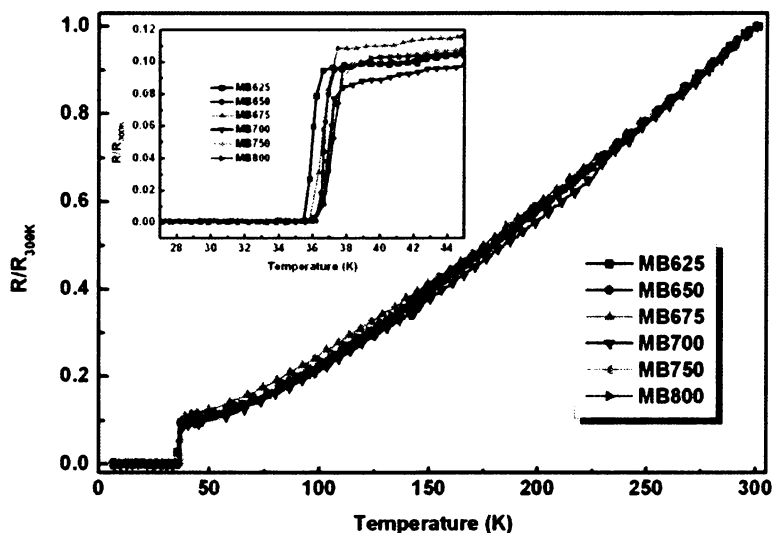


Figure 5.9: R - T plots of MgB_2/Fe wire samples processed at different temperatures. Inset shows the enlarged portion of R - T plot near the superconducting transition region

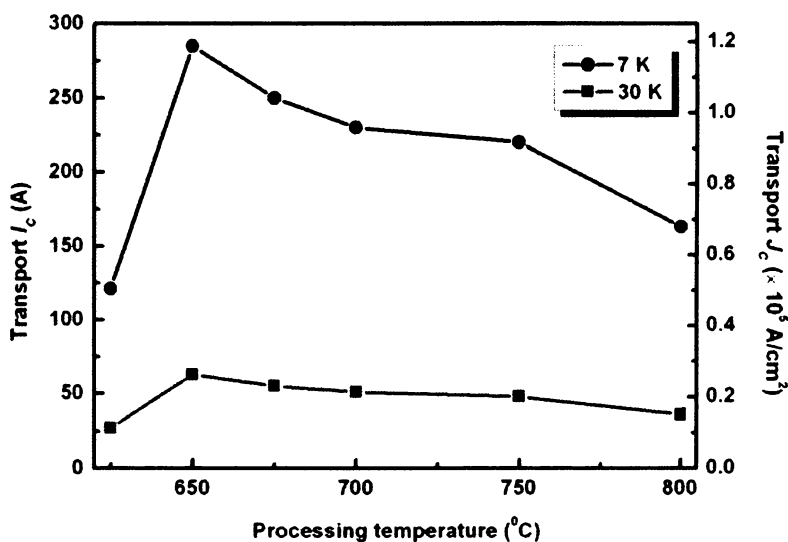


Figure 5.10: Variation of transport I_c and J_c of MgB_2/Fe wire samples with processing temperature

Figure 5.9 shows the temperature dependence of the normalized resistance of the MgB₂/Fe wires processed at different temperatures. All samples show sharp superconducting transitions and the observed T_C is tabulated in table 5.3. It is found that T_C increases systematically with processing temperature. This suggests that better crystallinity is achieved with higher processing temperatures. Relatively poor crystallinity in samples prepared at lower temperatures points to disorder in the crystal lattice, which leads to lower T_C .

The measurement of self-field transport current properties of MgB₂/Fe wires for different processing temperatures has been done at 7 and 30 K (figure 5.10). As seen from the graph, transport currents at both 7 and 30 K are found to be increasing systematically with the processing temperature, up to 650 °C. Among all samples, the one processed at 650 °C gives the highest transport current of 1.19×10^5 and 2.61×10^4 A/cm² at 7 and 30 K respectively. It is to be noted that the sample sintered at 650 °C contains only 80.8 % MgB₂ and it contains 16.5 % Mg. There were reports of better superconducting properties in MgB₂/Fe samples with excess Mg addition [19, 20]. Hence, the presence of unreacted Mg in moderate amount in the MgB₂ matrix helps in better connectivity. Moreover, both FWHM and SEM analysis confirm that grain size increases with the processing temperature. In the case of MgB₂, the grain boundaries can act as flux pinning centers and hence the grain size has significant role in enhancing the critical current at both self-field and in-field. The slight decrease in J_C of samples processed at higher temperatures is due to the decrease in the amount of unreacted Mg and increase in grain size, while the formation of non-superconducting phases such as FeB₂ causes significant reduction of J_C in the sample processed at 800 °C.

5.3.4: Conclusion

The effect of processing temperature on phase formation, microstructure and transport critical current of MgB₂/Fe monofilamentary wire samples processed at temperatures 600-800 °C were studied. All samples show a systematic increase in MgB₂ phase formation and T_C except for the sample processed at 800 °C. At lower processing temperatures, the crystallinity and grain size of MgB₂ formed will be lesser and hence

contains more structural defects and grain boundaries. The sample processed at 650 °C gave the best self-field transport J_C value of 1.19×10^5 A/cm² at 7 K. The presence of reasonable amount of unreacted Mg and the reduced grain size are the reasons for enhancing the critical current of the sample processed at 650 °C.

5.4: Influence of nano Cu additive on MgB₂ phase formation, processing temperature and transport properties

5.4.1: Introduction

Doping of various elements and compounds has been attempted in order to fabricate *in situ* MgB₂ bulk and wires with high critical current density. However, most of these doped samples were fabricated at high temperatures above 650 °C and very often the sheath materials reacted with Mg/B at elevated temperatures. Moreover, processing at higher temperatures causes higher volatile loss of Mg and significant increase in the formation of MgO, which weakens the grain to grain connectivity in MgB₂ matrix [21, 22]. In order to avoid these problems, some recent studies have concentrated on the low temperature solid state sintering method to prepare pure or doped MgB₂ samples with improved J_C . Yamamoto *et al.* obtained pure MgB₂ samples by processing at 600 °C for 60 hrs [23]. Rogado *et al.* prepared pure MgB₂ bulk by processing at 550 °C for 16 hrs with an intermediate grinding step with improved J_C [24]. However, the reaction between Mg and B at 550 °C needed a very long time to form the complete MgB₂ phase due to the low diffusion rate of atoms in the solid state below the melting point of Mg. Some reports suggested that use of MgH₂ or nano sized Mg particles and high quality B powder as starting materials were effective in lowering the synthesis temperature of MgB₂ samples, but heating above 600 °C was essential to form the MgB₂ phase [25-28].

Recently, some efforts on lowering of synthesis temperature of MgB₂ were made by the addition of suitable metal powders into the system [29-33]. It was observed that the metal doping introduced liquid phase during the reaction which assisted the phase formation of MgB₂. Among these methods, Cu doping proved to be the most effective. However, the

results reported so far on Cu doped MgB_2 have been limited to magnetic measurements. The major concern is whether the material can carry large transport J_C . In this work, effect of nano Cu additive on phase formation, processing temperature and transport properties of MgB_2 is focused. Mg, amorphous B, Cu nano powder (<100 nm, 99.8 %) and commercially available Fe tubes were used for processing. The tubes were filled with homogeneously mixed pure (Mg+B) and doped (Mg+B+2.5 wt% Cu) powders and mechanically compacted. The reason for choosing 2.5 wt% Cu is explained in the subsequent section. The composite tubes were then groove rolled into wires of 1.33 mm OD. These were cut into short length (10 cm) samples and end sealed. The sealed wires were then heat treated directly in air at 550, 575, 600, 625, 650 and 675 °C for 2 hrs in a muffle furnace and subsequently cooled by switching off the furnace.

5.4.2: Results and discussion

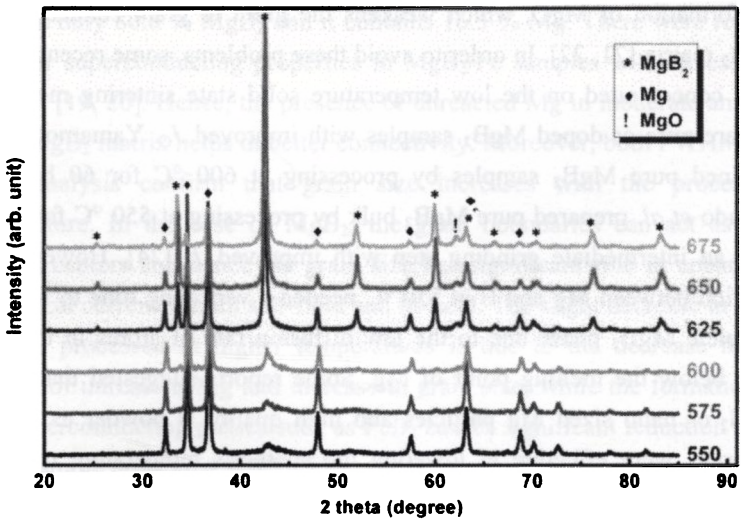


Figure 5.11: XRD patterns of pure MgB_2 samples processed at different temperatures (550-675 °C)

Figure 5.11 shows the XRD patterns of pure MgB_2 samples processed at temperatures varying from 550 °C to 675 °C. The first three samples processed at 550, 575 and 600 °C which are well below the melting point of Mg exhibit almost similar patterns. It is found that starting Mg

remained as the main phase with small peaks of MgB_2 . The rate of diffusion is not high enough to form considerable amount of MgB_2 within two hours at these temperatures. But when the processing temperature increases to 625 °C, diffusion rate increases and hence the formation rate of MgB_2 also increases. At higher temperatures, Mg starts melting and the reaction rate is further enhanced. But some unreacted Mg can be seen in these samples, because temperature/duration is insufficient for complete formation of MgB_2 . However, it is reported that an optimum amount of excess Mg is helpful in improving $J_C(H)$ behavior of MgB_2 [34].

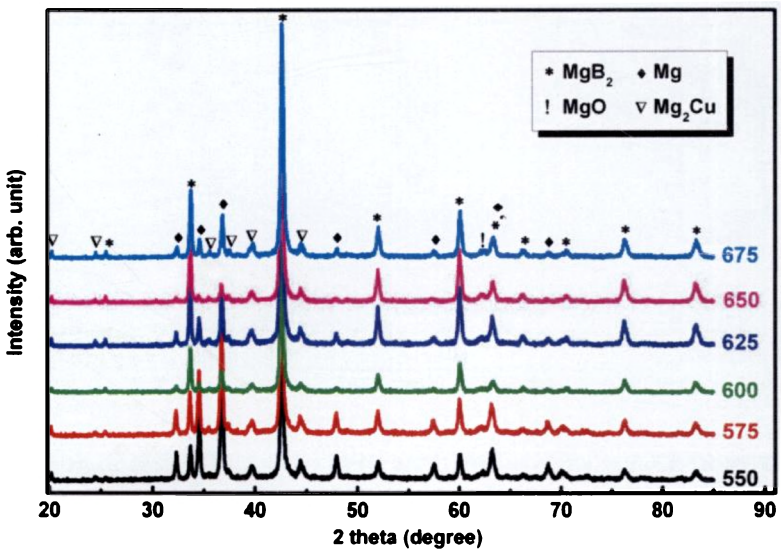


Figure 5.12: XRD patterns of nano Cu added MgB_2 samples processed at different temperatures (550-675 °C)

Figure 5.12 shows the XRD patterns of Cu added samples processed at temperatures similar to pure samples. It can be seen that, at 550 °C itself remarkable quantity of MgB_2 has been formed. As the temperature increases, the Mg content reduces and MgB_2 content improves. Some trace of MgO is observed in both pure and Cu added samples at higher temperatures. Since the size of Cu particles used in the present work are much smaller and are more reactive than the B particles, in MBCu samples Mg reacts first with Cu forming the Mg_2Cu phase. As a result, the presence of local Mg_2Cu liquid phase (melting point of Mg_2Cu is ~550 °C) could

accelerate the reaction between Mg and B and finally results in the formation of MgB_2 phase even at such low temperatures. The peak intensity of Mg_2Cu remains constant throughout the entire range of temperatures, which indicates that the formation of Mg_2Cu is saturated at 550 °C itself. In *figure 5.12*, it can also be observed that the peak positions of the MgB_2 phase in the Cu added samples remain unchanged, which indicates that there is no Cu substitution in MgB_2 .

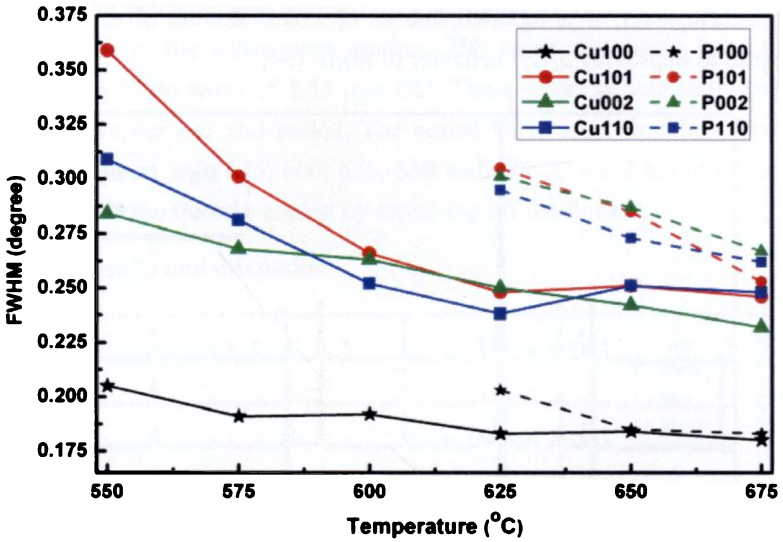


Figure 5.13: Variations of FWHM of (100), (101), (002) and (110) peaks of pure and Cu added MgB_2 samples

From the XRD, the FWHM values of (100), (101), (002), and (110) peaks of pure and Cu added MgB_2 are shown in *figure 5.13*. It can be seen that the FWHM values steadily decrease with the increase in processing temperature for both pure and Cu added MgB_2 samples indicating the increase in grain size of MgB_2 with temperature. The pure sample exhibits higher FWHM values compared to Cu added samples at identical processing temperatures. Further, the results are correlated with the microstructure of the samples. *Figure 5.14* shows the SEM images of both pure (625 and 650 °C) and Cu added (550, 575, 600 and 650 °C) MgB_2 samples. For pure samples, MgB_2 grains of relatively smaller size have been formed compared to corresponding Cu added samples at the same

temperature. The SEM images of Cu added samples show small MgB_2 grains starting from 550 °C itself. It is clear that addition of Cu not only accelerates the formation of the MgB_2 phase but also improves the crystallinity and grain connectivity of MgB_2 appreciably as the processing temperature increases. Another point to be noted from the microstructures is that the density of Cu added samples is distinctly higher than that of pure MgB_2 samples.

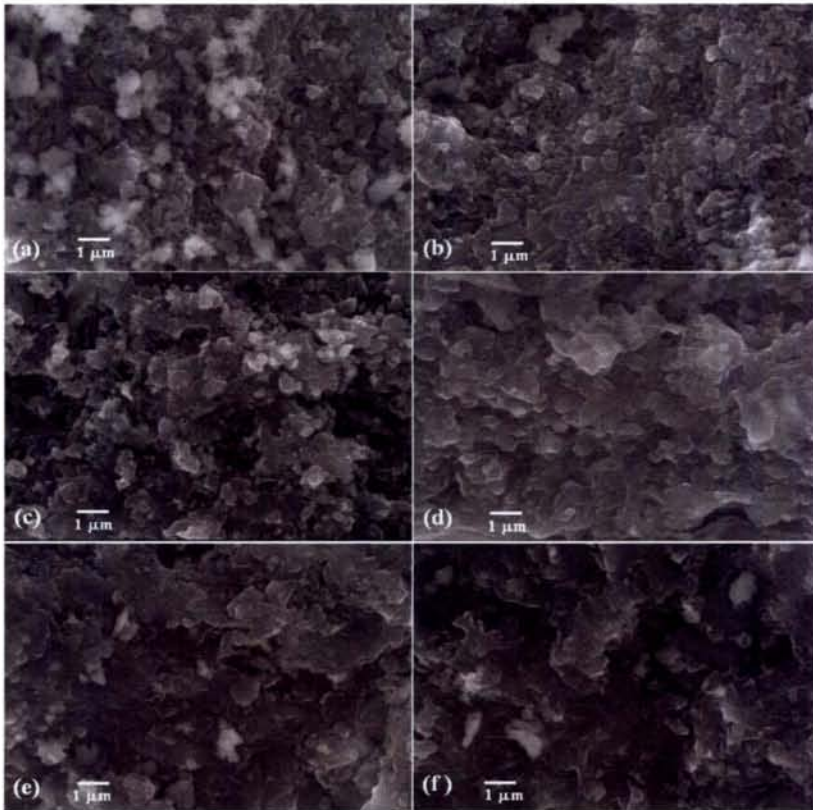


Figure 5.14: SEM images of the fractured surfaces of pure MgB_2 sample heat treated at (a) 625 °C and (b) 650 °C and Cu added MgB_2 samples heat treated at (c) 550 °C, (d) 575 °C, (e) 600 °C and (f) 650 °C

Figure 5.15 compares the temperature dependence of resistance for pure MgB_2 sample processed at 650 °C and Cu added sample at 550 °C. As shown, these samples exhibit sharp superconducting transitions with T_C

around 38 K and a transition width, $\Delta T_C < 1.5$ K. It is observed that for nano Cu added sample the superconducting transition remains sharp at 38 K which implies that Cu is not substituted at Mg/B sites and the impurities formed have little effect on T_C .

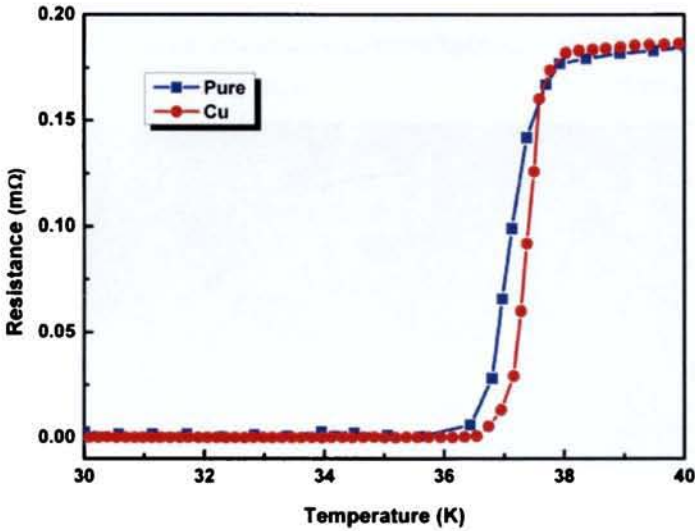


Figure 5.15: Temperature dependence of resistance for pure MgB_2 sample processed at 650 °C and Cu added sample at 550 °C

The measurement of self-field transport current properties of Cu doped MgB_2 wires has been done and compared with those of the pure MgB_2 wires for different processing temperatures (*figure 5.16*). As seen from the graph, J_C of Cu added MgB_2 wire measured at 30 K is higher compared to the corresponding pure MgB_2 wires till the processing temperature reaches 650 °C. The transport J_C of Cu added wire processed at 550 °C (2.2×10^4 A/cm²) is quite comparable with that of Cu-free wire processed at 650 °C (2.5×10^4 A/cm²). At/above 650 °C, both the samples exhibit nearly same critical current densities and the J_C is found to be slightly lesser for both samples beyond 650 °C. This may be due to the slight increase in MgO formation at the grain boundaries, in these samples. The highly enhanced critical current density for Cu added samples prepared at lower temperatures is due to the enhanced rate of formation of MgB_2 at lower temperatures. The selection of weight percentage of Cu as 2.5 was

done on the basis of J_C measurements of MgB₂ wires with varying weight percentage of Cu processed at 600 °C (inset of figure 5.16). Among which 2.5 wt% of Cu yielded the highest J_C .

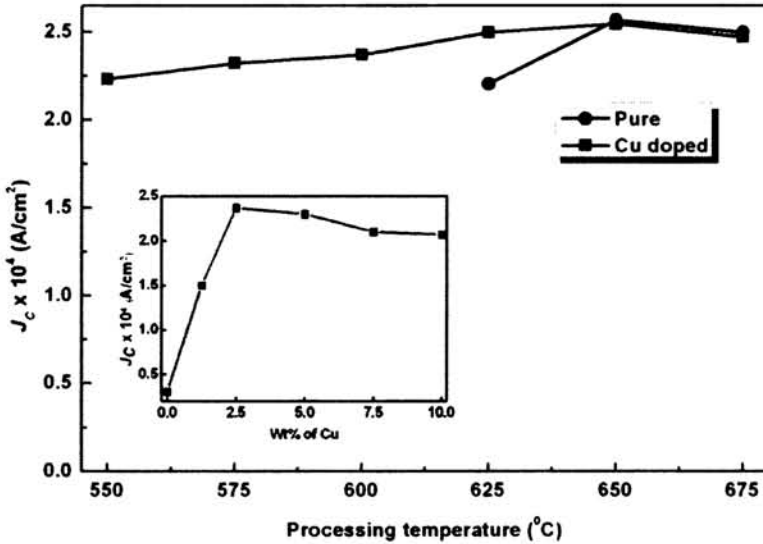


Figure 5.16: Variation of J_C with processing temperatures of pure and Cu added MgB₂ samples at 30 K. Inset shows variation of J_C with wt% of Cu added in the MgB₂ samples processed at 550 °C.

5.4.3: Conclusion

The effects of nano Cu addition on the superconducting properties of MgB₂/Fe wires were studied. Both pure and Cu added samples were prepared by *in situ* PIT method and processed at different temperatures ranging from 550–675 °C. It was found that the MgB₂ can be synthesized at around 550 °C with minor Cu addition, which offers a substantial reduction in the processing temperature compared to that of pure MgB₂. All the Cu added samples processed below 650 °C showed enhanced transport J_C values compared to the Cu-free samples. The transport J_C of Cu added wire processed at 550 °C is quite comparable with that of Cu-free wire processed at 650 °C. The added nano Cu preferentially reacts with Mg and forms Mg₂Cu which melts at around 550 °C. The liquid phase thus formed assists the formation of MgB₂ at a lower temperature.

5.5: Preparation of MgB_2/Fe superconducting tapes with highly densified core by hot-pressing of *in situ* PIT wires

5.5.1: Introduction

A major problem in the manufacture of MgB_2 conductors is their high porosity. This is severe in the case of *in situ* preparation in which only around 50 % of theoretical density could be achieved in many cases. This is mainly caused by the low packing density of Mg and B powder mixture and the volume shrinkage during the *in situ* formation of MgB_2 . The porosity limits the active current carrying area fraction and also weakens the grain connectivity. Measures to reduce porosity of MgB_2 have been taken since its discovery by adopting hot isostatic pressing or high pressure sintering with excellent results [35-37]. However, most of the works are limited to *ex situ* process and also the methods have limitations in making long length conductors. *In situ* process is more flexible with respect to chemical doping and hence leads to MgB_2 with improved performance in higher magnetic fields. Flükiger's group reported making of *ex situ* MgB_2 tapes by a conventional hot rolling method, wherein the roller has been heated to high temperatures [38]. By this method, they have studied the effect of rolling on the anisotropy and texture gradient of MgB_2 tapes with respect to the particle size of the precursor. However, energy required for heating up the massive roller for large scale production of thin MgB_2 tapes is considerably high.

In this work, we report a simple, energy efficient and inexpensive method for preparation of Fe-sheathed MgB_2 conductors with high core density and critical current by hot-pressing of *in situ* PIT wires. Compared to the conventional hot rolling method this method is energy efficient as the sample itself is heated instead of the massive roller. The method also significantly reduces the oxidation and evaporation loss of Mg and has many advantages such as less preparation cost and power consumption due to the avoidance of special furnaces with inert gas atmosphere. With suitable engineering, the present method can be transformed into a hot rolling process for the continuous production of high quality MgB_2 conductors.

5.5.2: Preparation and characterization of hot-pressed MgB_2 tapes

Mg, amorphous B and Fe tubes of suitable dimensions were used for the preparation of PIT wires. The tubes were filled with homogeneously mixed Mg and B powders and mechanically compacted. The composite tubes were then groove rolled into wires of 1.47 mm OD. Samples of length 20 cm were used for hot-pressing after end sealing. In this work, PIT wire was heated by passing a suitable current, followed by pressing in hot conditions with the help of a hydraulic press.

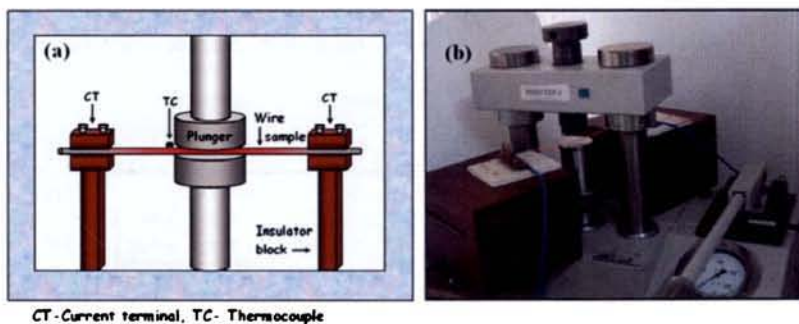


Figure 5.17: (a) Schematic diagram and (b) photograph of the experimental set up for hot-pressing

The system for electrical self-heating and hot-pressing mainly consists of a programmable current source (*DC*), hydraulic press and the sample anchored horizontally as shown in *figure 5.17 (a) and (b)*. The sample is positioned such that it is aligned parallel between the top and bottom plungers of the press. A thermocouple (*TC*) is kept very close to the uniform hot region outside the plunger area to monitor the temperature. The sample is heated by passing a suitable current through the sample, either manually or automatically through a *PC* interface. Temperature of the sample is increased at a ramp rate of $20\text{ }^{\circ}\text{C}/\text{min}$, soaked for a total period of 60 or 120 minutes at $700\text{ }^{\circ}\text{C}$, and then cooled at a rate of $20\text{ }^{\circ}\text{C}/\text{min}$ to room temperature. During the soaking period, samples were pressed at a pressure of 500 MPa without putting off the power. Four sets of different samples were prepared with varying soaking durations, before and after pressing. The voltage and current readings during soaking were 3.2 V and 28 A respectively and the energy consumption for preparation of a typical sample

with 60 min soaking was 0.11 kWh. Apart from these, a set of wire samples was prepared by electrical self-heating at 700 °C without pressing for comparison of microstructure and density with the hot-pressed ones. The sample details are given in *table 5.4*. Short length samples for characterizations were then selected by properly cutting out the hot-pressed area.

Phase analysis and microstructural investigation of the samples were performed using XRD and SEM. The density of the MgB_2 core was determined by hydrostatic method. Superconducting properties such as $R-T$ and I_C measurements were carried out by employing a cryocooler interfaced cryostat by four probe resistive method.

5.5.3: Results and discussion

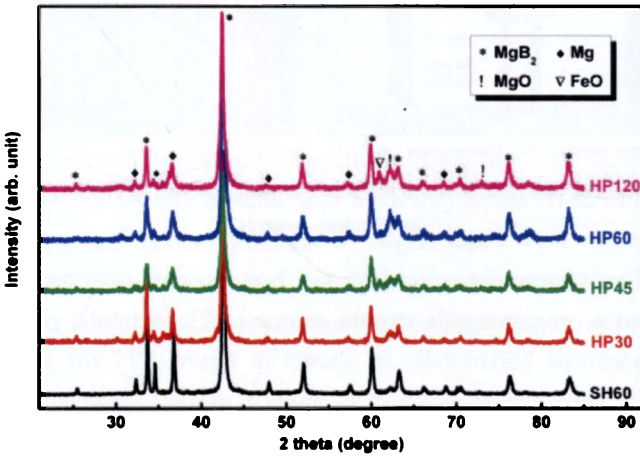


Figure 5.18: XRD patterns of self-heated and hot-pressed MgB_2 samples

XRD patterns of the hot-pressed samples soaked for different durations before and after pressing are shown in *figure 5.18*. All the patterns contain MgB_2 as the major phase. Traces of MgO and some unreacted Mg are observed in all the samples. Minor amount of FeO is found in some samples which may be from the sheath material. Absence of FeB_2 peaks indicates that there is almost no (or very small) reaction between Fe sheath and B . *Figure 5.19* shows SEM images of fractured surface (both transverse sectional view and enlarged core view) of MgB_2 wire (SH60) prepared by self-heating alone and a tape (HP60) prepared by hot-pressing. The images

show distinct microstructural differences for the samples with and without hot-pressing. The core is observed to be significantly densified in the tape compared to the wire. The wire contains large pores, characteristic of the *in situ* prepared MgB₂, caused by the low green density of the (Mg+B) mixture and the volume shrinkage during MgB₂ formation. On the other hand, the tape has highly dense core with well connected grains.

Table 5.4: Soaking details, density and transport current of self-heated and hot-pressed MgB₂ samples

Samples	Soaking duration (min)		Density (g/cm ³)	I_C (A)	J_C ($\times 10^4$ A/cm ²) at 30 K
	Before pressing	After pressing			
SH60	60 (without pressing)		1.41	31	0.8
HP30	30	30	2.38	36	1.4
HP45	45	15	2.33	40	1.6
HP60	60	00	2.45	75	3.0
HP120	120	00	2.23	65	2.6

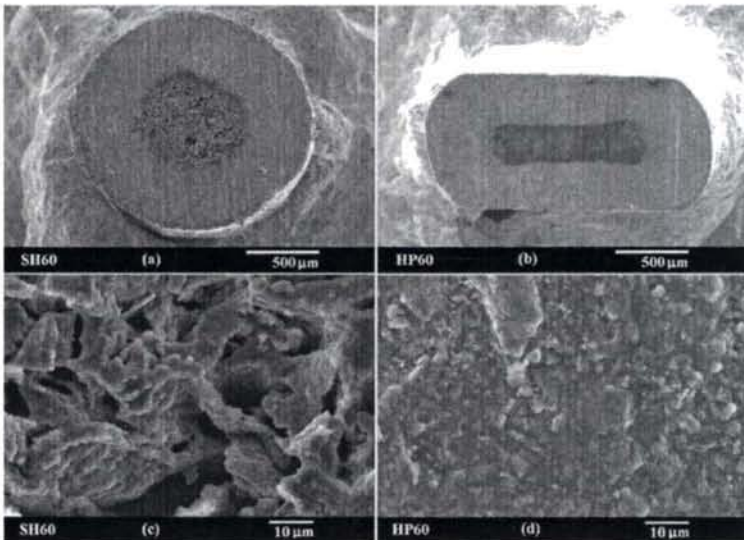


Figure 5.19: SEM images of fractured surface of typical MgB₂ samples

The core density of the self-heated and hot-pressed MgB_2 samples is also given in *table 5.4*. All the hot-pressed samples have significantly higher density compared to the sample prepared without pressing. The core density of the self-heated wire and the hot-pressed tape after a soaking duration of 60 min is found to be 1.41 and 2.45 g/cm^3 respectively which corresponds to 53.6 % and 93.2 % of the theoretical density of MgB_2 (2.63 g/cm^3). The increase in density was verified by estimating the volume reduction of the core by comparing the core area of the wire and tape with the help of an image analyzer. The volume reduction was estimated to be 41.8 %, which matches with the increase in density.

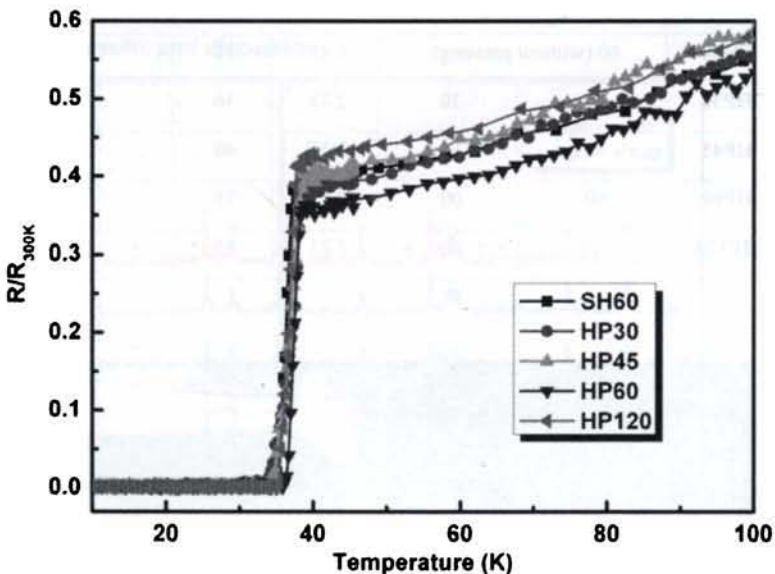


Figure 5.20: R - T plots of self-heated and hot-pressed MgB_2 samples

Temperature dependence of the normalized resistance of all samples exhibit sharp superconducting transitions with T_C around 38.5 K and a transition width, $\Delta T_C < 1$ K as observed in *figure 5.20*. The measurement of self-field transport current properties of self-heated and hot-pressed MgB_2 samples has been done at 30 K and tabulated in *table 5.4*.

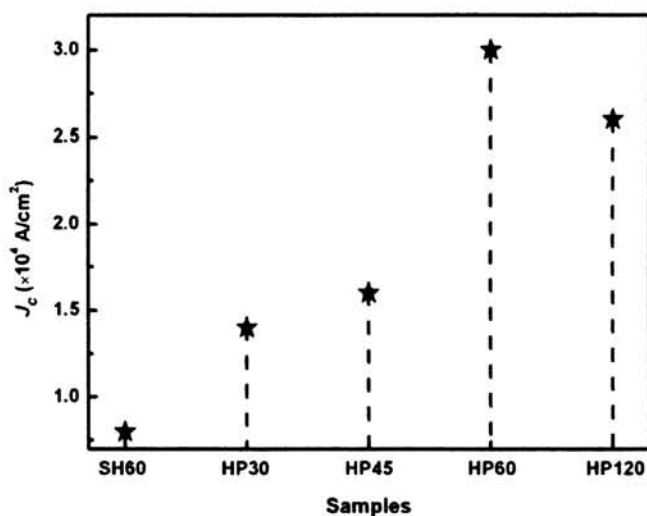


Figure 5.21: J_C of self-heated and hot-pressed MgB_2 samples

The variation of J_C of each sample is plotted in *figure 5.21*. Among the hot-pressed samples, critical current is minimum for HP30 and maximum for HP60. The J_C values of all the hot-pressed samples are significantly higher compared to the self-heated wire sample (SH60). It is to be noted that the samples HP30, HP45 and HP60 have undergone a total period of 60 min soaking at 700 °C. For hot-pressed samples, J_C is found to be increasing with the initial soaking duration (before pressing), up to 60 min. On the other hand, further increase in soaking duration shows a reduction trend in both density and J_C . The maximum J_C achieved for the hot-pressed sample (3×10^4 A/cm 2 at 30 K) is almost 4 times of that obtained for the self-heated sample soaked for the same duration without pressing. This clearly shows that for obtaining maximum J_C the sample needs to be soaked for an optimum period before pressing, which is necessary for the maximum densification of MgB_2 core so as to achieve well connected grains for a maximum super current flow. The method described here can be engineered into a continuous hot rolling process with an array of groove rollers in tandem initially for wire making, followed by an arrangement for electrical self-heating and flat rolling at the end. This can produce highly densified high performance MgB_2 conductors.

5.5.4: Conclusion

A simple and easy method for preparation of *in situ* MgB₂ superconducting tapes with highly densified core has been demonstrated. The method comprises heating of the PIT wire by passing a suitable current, followed by pressing in hot conditions with the help of a hydraulic press. A core density of 2.45 g/cm³ (93.2 % of theoretical density) and almost 4-fold increase in critical current are achieved for the best hot-pressed sample. The method is highly energy efficient since it uses electrical power only for heating the wire/tape whereas in conventional heat treatment process electrical power is required for heating a furnace loaded with the wire/tape.

5.6: Summary

The role of the reactivity of sheath material with Mg/B on the phase formation and superconducting properties of MgB₂ was studied. It was found that Cu and Ni react with Mg/B and the reacted phases reduce the volume of superconducting core and impede intergrain connectivity resulting lower J_c at higher fields. On the other hand, in the case of Fe and SS, the samples give higher volume fraction of MgB₂ core and hence better $J_c(H)$ characteristics which infers that Fe and SS are more suitable as sheath materials in MgB₂ wire fabrication. The effect of processing temperature on phase formation, microstructure and transport critical current of MgB₂ monofilamentary wire samples processed at temperatures in the range 600-800 °C were also studied. The sample processed at 650 °C gave the best self-field transport J_c . The presence of reasonable amount of unreacted Mg and the reduced grain size are found to be the reasons for enhancing the critical current of the sample processed at 650 °C. The effects of nano Cu addition on the superconducting properties of MgB₂/Fe wires were studied. It was found that the MgB₂ can be synthesized at around 550 °C with minor Cu addition, which offers a substantial reduction in the processing temperature (by around 100 °C) compared to that of pure MgB₂. The added nano Cu preferentially reacts with Mg and forms Mg₂Cu which melts at around 550 °C. The liquid phase thus formed assists the formation of MgB₂ at a lower temperature. Fe sheathed *in situ* MgB₂ superconducting tapes with high densities were prepared by hot-pressing of electrically self-heated

PIT wires. The method comprises heating of the PIT wire by passing a suitable current, followed by pressing in hot conditions with the help of a hydraulic press. A core density of 2.45 g/cm³ (93.2 % of theoretical density) and almost 4-fold increase in critical current are achieved for the best hot-pressed sample.

References:

1. P. C. Canfield, D. K. Finnemore, S. L. Bud'ko, J. E. Ostenson, G. Lapertot, C. E. Cunningham and C. Petrovic, *Phys. Rev. Lett.* 86, 2423 (2001)
2. P. Kovac, I. Husek, C. Grosvenor and C. Salter, *Supercond. Sci. Technol.* 16, 292 (2003)
3. H. Kitaguchi, A. Matsumoto, H. Hatakeyama and H. Kumakura, *Supercond. Sci. Technol.* 17, S486 (2004)
4. K. Yamamoto, K. Osamura, S. Balamurugan, T. Nakamura, T. Hoshino and I. Muta, *Supercond. Sci. Technol.* 16, 1052 (2003)
5. W. Goldacker, S. I. Schlachter, B. Obst and M. Eisterer, *Supercond. Sci. Technol.* 17, S490 (2004)
6. Y. Feng, G. Yan, Y. Zhao, C. F. Liu, X. H. Liu, P. X. Zhang, L. Zhou, A. Sulpice, E. Mossang and B. Hebral, *J. Phys.: Condens. Matter* 16, 1803 (2004)
7. H. Yamada, M. Hirakawa, H. Kumakura, A. Matsumoto and H. Kitaguchi, *Appl. Phys. Lett.* 84, 1728 (2004)
8. E. Martinez, L. A. Angurel and R. Navarro, *Supercond. Sci. Technol.* 15, 1043 (2002)
9. X. L. Wang, S. Soltanian, J. Horvat, A. H. Liu, M. J. Qin, H. K. Liu and S. X. Dou, *Physica C* 361, 149 (2001)
10. E. W. Collings, E. Lee, M. D. Sumption, M. Tomsic, X. L. Wang, S. Soltanian and S. X. Dou, *Physica C* 386, 555 (2003)
11. S. Soltanian, X. L. Wang, J. Horvat, A. H. Li, H. K. Liu and S. X. Dou, *Physica C* 382, 187 (2002)

12. B. A. Glawacki, M. Majors, M. E. Vickers and B. Zeimetz, *Physica C* 372, 1254 (2002)
13. G. Grasso, A. Malagoli, D. Marre, E. Bellinger, V. Braccini, S. Roncallo, N. Scati and A. S. Siri, *Physica C* 378, 899 (2002)
14. H. L. Suo, C. Beneduce, M. Dhall'e, N. Musolino, J. Y. Genoud and R. Fl'ukiger, *Appl. Phys. Lett.* 79, 3116 (2001)
15. P. Kov'a'c, I. Hu'sek, T. Meli'sek, M. Kulich and V. Strb'ik, *Supercond. Sci. Technol.* 19, 600 (2006)
16. W. Goldacker, S. I. Schlachter, C. Zimmer and H. Reiner, *Supercond. Sci. Technol.* 14, 787 (2001)
17. H. Fang, S. Padmanabhan, Y. X. Zhou and K. Salama, *Appl. Phys. Lett.* 82, 4113 (2003)
18. H. Fang, P. T. Putman, S. Padmanabhan, Y. X. Zhou and K. Salama, *Supercond. Sci. Technol.* 17, 717 (2004)
19. C. H. Jiang, T. Nakane and H. Kumakura, *Appl. Phys. Lett.* 87, 252505 (2005)
20. O. Perner, J. Eckert, W. H'a'bler, C. Fischer, J. Acker, T. Gemming, G. Fuchs, B. Holzapfel and L. Schultz, *J. Appl. Phys.* 97, 056105 (2005)
21. C. H. Jiang, H. Hatakeyama and H. Kumakura, *Physica C* 423, 45 (2005)
22. J. H. Kim, S. X. Dou, D. Q. Shi, M. Rindfleisch and M. Tomsic, *Supercond. Sci. Technol.* 20, 1026 (2007)
23. A. Yamamoto, J. I. Shimoyama, S. Ueda, Y. Katsura, S. Horii and K. Kishio, *Supercond. Sci. Technol.* 18, 116 (2005)
24. N. Rogado, M. A. Hayward, K. A. Regan, Y. Wang, N. P. Ong, H. W. Zandbergen, J. M. Rowell and R. J. Cava, *J. Appl. Phys.* 91, 274 (2002)
25. H. Fujii, K. Togano and H. Kumakura, *Supercond. Sci. Technol.* 15, 1571 (2002)
26. C. Chen, Z. J. Zhou, X. G. Li, J. Xu, Y. H. Wang, Z.X. Gao and Q. R. Feng, *Solid State Commun.* 131, 275 (2004)
27. S. X. Dou, S. Soltanian, J. Horvat, X. L. Wang, S. H. Zhou, M. Ionescu, H. K. Liu, P. Munroe and M. Tomsic, *Appl. Phys. Lett.* 81, 3419 (2002)

28. S. K. Chen, K. A. Yates, M. G. Blamire and J. L. MacManus-Driscoll, *Supercond. Sci. Technol.* 18, 1473 (2005)
29. J. Shimoyama, K. Hanafusa, A. Yamamoto, Y. Katsura, S. Horii, K. Kishio and H. Kumakura, *Supercond. Sci. Technol.* 20, 307 (2007)
30. J. C. Grivel, A. Abrahamsen and J. Bednarčák, *Supercond. Sci. Technol.* 21, 035006 (2008)
31. Z. Ma, H. Jiang and Y. Liu, *Supercond. Sci. Technol.* 23, 025005 (2010)
32. Z. Q. Ma, Y. C. Liu, Q. Z. Shi, Q. Zhao and Z. M. Gao, *Supercond. Sci. Technol.* 21, 065004 (2008)
33. Z. Ma, Y. Liu, W. Hu, Z. Gao, L. Yu and Z. Dong, *Scr. Mater.* 61, 836 (2009)
34. R. Zeng, L. Lu, W. X. Li, J. L. Wang, D. Q. Shi, J. Horvat, S. X. Dou, M. Bhatia, M. Sumption, E. W. Collings, J. M. Yoo, M. Tomsic and M. Rindfleisch, *J. Appl. Phys.* 103, 083911 (2008)
35. T. C. Shields, K. Kawano, D. Holdom and J.S. Abell, *Supercond. Sci. Technol.* 15, 202 (2002)
36. A. Serquis, L. Civale, D. L. Hammon, X. Z. Liao, J. Y. Coulter, Y. T. Zhu, M. Jaime, D. E. Peterson, F. M. Mueller, V. F. Nesterenko and Y. Gu, *Appl. Phys. Lett.* 82, 2847 (2003)
37. Y. Takano, H. Takeya, H. Fujii, H. Kumakura, T. Hatano, K. Togano, H. Kito and H. Ihara, *Appl. Phys. Lett.* 78, 2914 (2001)
38. P. Lezza, C. Senatore, R. Gladyshevskii and R. Flükiger, *IEEE Trans. Appl. Supercond.* 17, 2834 (2007)

6.1: Introduction

Extensive efforts are going on in MgB₂ conductor development aiming to improve the properties such as transport J_C , upper critical field, and irreversibility fields suitable for specific applications [1-4]. A few groups [5-7] are also focusing on different multifilamentary wire geometries in order to attain features like transport current stability, strain tolerance, flux jump stability, and ac loss reduction. The filamentary subdivision is essential for Bi based conductors (HTS) and NbTi (LTS) in order to improve strain tolerance and limit flux jump respectively, and both these are applicable for MgB₂ conductors as well. The current carrying capability of superconducting wires will be also degraded by stress. Therefore, stress-strain characteristics are one of the key feedback parameters to be monitored for their use in high field magnet and electric power applications. Along with good electromechanical properties, it is also necessary to demonstrate long MgB₂ wires with adequate homogeneity of I_C distribution in solenoid or coil forms for magnetic applications. At operating temperatures from 4 to 30 K, price performance of the MgB₂ wire can potentially enable the design and fabrication of magnetic windings and magnets, which are central elements for many large scale applications. MgB₂ can also be used for making superconducting current leads which can feed high currents from electrical power sources kept at room temperature into magnets operating at very low temperatures with reduced heat leak. In brief, for application purposes, it is highly essential to develop multifilamentary wires, coils and current leads with high current carrying capacity and this chapter deals with the same.

6.2: Development of MgB_2 multifilamentary wires with enhanced in-field critical current density

6.2.1: Introduction

In parallel to basic research on improving the critical current density behavior of bulk MgB_2 , strenuous efforts are continuing on the fabrication of multifilamentary conductors from an application point of view. MgB_2 composite wires suitable for windings need to use sufficiently strong sheath material due to its direct effect on the powder core density [8] and also with good electrical and thermal conductivity to sustain good thermal stability [9-11]. Thermal stability is related to the maximum current that a superconducting filament can carry. When the current becomes too high, current density fluctuations cause localized dissipation. Such hotspots can grow and drive the whole wire non-superconducting. Thermal stability is increased using low resistive alternative current paths, enabling the current to bypass local hotspots and thus avoiding thermal runaway [10, 11]. Oxygen free high conductivity (OFHC) copper is a proper material that can be incorporated for making stabilized superconducting wires. In the case of MgB_2 , due to the high reactivity of boron and magnesium with copper, it has to be protected by some barrier material. Hence, in order to manufacture multifilamentary wires, numerous monofilaments containing the superconducting powder with a protective sheath and a stabilizer must be stacked within another tube and then drawn down to the required wire diameter and length. In this section, the role of the outer sheath materials such as Cu, Fe and Ni in the transport properties of MgB_2 multifilamentary wires for a typical 4 filament configuration and the effect of typical nano dopants, especially those which gave the best results in bulk MgB_2 (*chapter 4*), on the in-field transport critical current of MgB_2 multifilamentary wires are discussed.

6.2.2: Preparation and characterization of MgB_2 multifilamentary wires:

6.2.2.1: Outer sheath variation

The preparation and optimization of parameters and identification of sheath material, for monofilamentary MgB_2 wires, have already discussed in *chapter 5*. Fe was chosen as the barrier material for the

6.2.2.2: Dopant variation

MgB_2 , $(MgB_2+n-SiC)$, (MgB_2+BRH) , (MgB_2+n-C) , $(MgB_2+BRH+n-Ho_2O_3)$ and $(MgB_2+n-SiC+n-Ho_2O_3)$ multifilamentary samples were prepared using Mg, B, n-SiC, BRH, n-C and n- Ho_2O_3 as the starting materials for monowires. The Ni sheathed and Cu stabilized configuration is used for the preparation of doped MgB_2 multifilamentary wires. The samples pure MgB_2 , (MgB_2+BRH) , $(MgB_2+n-SiC)$, (MgB_2+n-C) , $(MgB_2+BRH+n-Ho_2O_3)$ and $(MgB_2+n-SiC+n-Ho_2O_3)$ are named as MB, MBR, MBS, MBC, MBHR and MBHS, respectively. The samples were then heat treated directly in air at 650 °C after end sealing. These Ni sheathed MgB_2 multiwires were then subjected to further characterizations. The in-field J_C measurements were done using LHe based 8 T solenoid magnet system.

6.2.3: Results and discussion:

6.2.3.1: Effect of outer sheath variation on MgB_2 multiwires

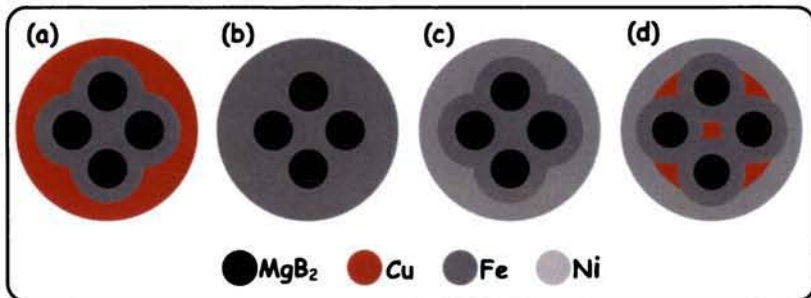


Figure 6.2: Schematic diagrams of the cross section of (a) MBCu, (b) MBFe, (c) MBNi and (d) MBNC multiwires

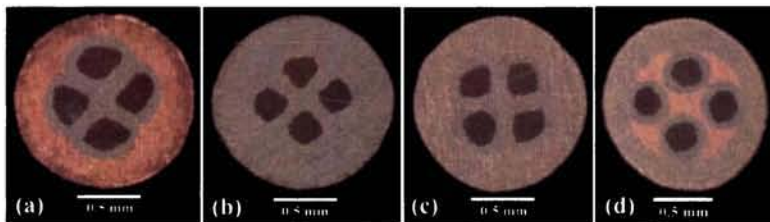


Figure 6.3: Optical images of the cross section of (a) MBCu, (b) MBFe, (c) MBNi and (d) MBNC multiwires

The multifilamentary MgB_2 wires of different configurations were subjected to optical microscopy to know whether there are any cracks or interfacial reaction between the core and the various sheath materials used. Figure 6.2 and 6.3 show the schematic view and the optical image of the cross sections of MBCu, MBFe, MBNi and MBNC multifilamentary MgB_2 wires, respectively. The MgB_2 core can be seen distinct, clear and free of any cracks in the images of all the multiwire samples. In the case of MBCu, the outer sheath Cu is clearly distinct from the barrier Fe matrix while for other samples the distinction between the outer sheath and the barrier is not clear due to the similarity in their colour. In all samples, the core-sheath interface is observed to be distinct, indicating the non reactivity of the core with sheath metal. The Cu filaments in MBNC multiwire are also visible without any significant diffusion between the barrier and outer sheath metals. Optical microscopy measurements, taken with the help of a scale built into the eyepiece, were used for the exact estimation of core and sheath cross sectional area.

The core area and the Vickers hardness (HV) of the outer sheath of the multiwires are tabulated in table 6.1. It is found that the core area decreases with the hardness of the outer sheath metal which indicates that the latter has a significant role in the superconducting core area fraction. The sheath hardness may enhance the J_C by improving the grain connectivity and density of MgB_2 matrix.

Table 6.1: Mechanical characteristics of MgB_2 multifilamentary wires

Wire samples	Outer sheath	Stabilizer	HV of outer sheath (MPa)	Core area (10^{-3} cm^2)	AF_{MgB_2} (%)
MBCu	Cu	-	369	2.37	17.1
MBFe	Fe	-	608	1.83	13.2
MBNi	Ni	-	638	1.59	11.5
MBNC	Ni	5Cu _f	638	1.54	11.1

Figure 6.4 shows the resistance versus temperature plots of MgB_2 multifilamentary wires with different outer sheaths. All multifilamentary wires show sharp transitions in the range 38.2-38.4 K (table 6.2) with transition width $\Delta T_C < 1$ K. The almost constant T_C and low ΔT_C values of the multifilamentary wires as those observed in both bulk and monofilamentary wire samples indicate the good quality and homogeneity of the superconducting core in the wires. The variations of resistance and slope of the R - T curve of the samples in the normal state are found to depend on the electrical resistivity of the outer sheath material used and these have no effect on the superconducting parameters like T_C and ΔT_C .

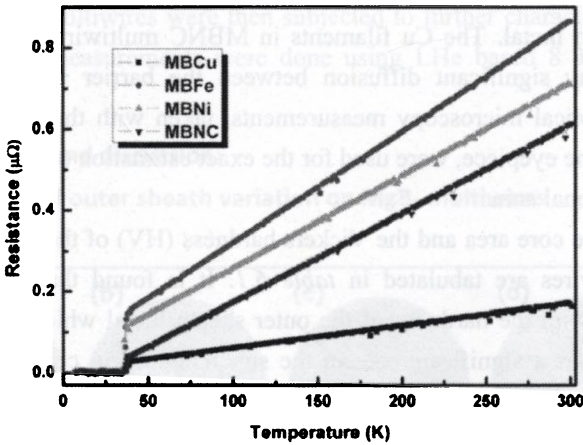


Figure 6.4: R - T plots of MgB_2 multifilamentary wires with different outer sheaths

Table 6.2: Superconducting characteristics of MgB_2 multifilamentary wires

Wire samples	T_C (K)	I_C (A) at		J_C (A/cm ²) at	
		4.2 K	30 K	4.2 K ($\times 10^5$)	30 K ($\times 10^4$)
MBCu	38.2	212	43	0.89	1.81
MBFe	38.4	170	35	0.93	1.91
MBNi	38.3	161	32	1.01	2.01
MBNC	38.4	165	33	1.07	2.14

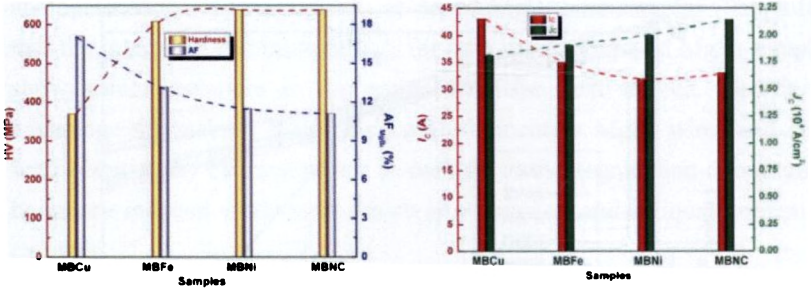


Figure 6.5: Variation of HV & AF_{MgB_2} (left) and I_C & J_C at 30 K (right) of MgB_2 multifilamentary wires with different outer sheaths

Figure 6.5 shows the variation of HV, AF_{MgB_2} , I_C and J_C (at 30 K) of MgB_2 multifilamentary wires with different outer sheaths where AF_{MgB_2} is the area fraction of MgB_2 core to that of the total cross section in percentage. Even though I_C decreases with the MgB_2 core fraction, J_C is found to be increasing which clearly indicates that the nature of the outer sheath has significant effect on J_C . This implies that the hardness of the outer sheath metal enhances J_C by improving the MgB_2 core density. Being an excellent stabilizing material, Cu can be used as outer sheath with high electrical and thermal conductivity. But as the hardness of Cu is much lower than that of Fe and Ni, it has little effect on core compaction and hence the lower J_C . Considering Fe and Ni as outer sheaths, their mechanical strength and stability are higher, despite their lower electrical and thermal conductivity. Among all, Ni sheathed wire exhibits higher J_C at 4.2 and 30 K as shown in table 6.2. Hence, it is obvious that on introducing Cu filaments as thermal stabilizers, Ni sheathed multiwire yields the highest J_C in view of the favorable mechanical characteristics of Ni and the electrical and thermal characteristics of Cu.

6.2.3.2: Effect of nano dopants on in-field transport J_C

On the basis of the study described in the previous section (section 6.2.3.1), Ni sheathed and Cu stabilized multifilamentary configuration is chosen for the preparation of MgB_2 multifilamentary wires ($MgB_2/Fe/Cu/Ni$) added with typical nano dopants especially those which gave best results in bulk MgB_2 as discussed in chapter 4.

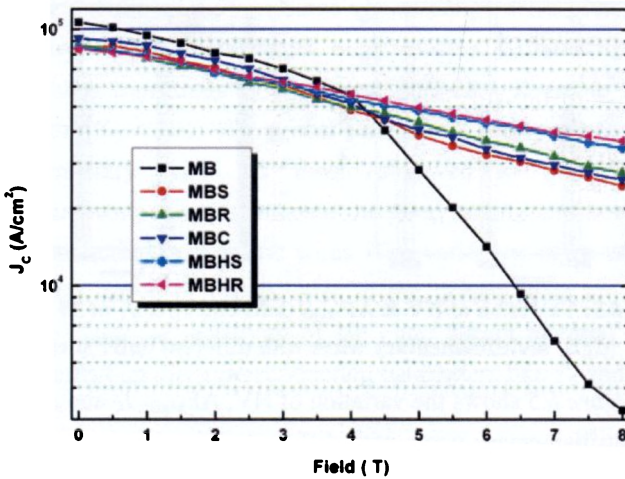


Figure 6.6: Field dependence of transport J_C for multifilamentary MgB_2 wires added with different nano dopants (at 4.2 K)

The field dependence of transport J_C at 4.2 K for multifilamentary MgB_2 wires added with different nano dopants such as n-SiC, BRH, n-C and n- Ho_2O_3 is shown in *figure 6.6*. The in-field J_C of pure MgB_2 wire is found to reduce rapidly above 4 T, whereas the MgB_2 multiwires added with nano dopants exhibit excellent $J_C(H)$ performance at higher fields. All the doped MgB_2 multiwires show almost similar trend at lower fields, but the codoped multiwires exhibit comparatively higher transport J_C than the monodoped ones at higher fields. The contribution towards the J_C enhancement of n-SiC and BRH monodoped samples, comes partly from C substitution and partly due to the presence of reacted phases as flux pinners while C substitution is the only reason for the J_C enhancement of MBC sample. For the codoped sample MBHS, both these effects, i.e. substitution due to C and flux pinning due to the reacted phases such as Mg_2Si and HoB_4 , contribute to the strong enhancement of J_C . Combined addition of n- Ho_2O_3 with BRH (MBHR) is found to be much effective for the enhancement of $J_C(H)$ of MgB_2 than the solo addition of any one of the additives. The substitution of C at B site by BRH and the formation of magnetic particles of HoB_4 by Ho_2O_3 are the reasons for the strong improvement of $J_C(H)$ in this sample. In short, the field dependence of transport J_C for the doped multifilamentary MgB_2 wires shows a behavior

analogous to that of magnetic J_C of doped MgB₂ bulk samples. This infers that the intergrain and intragrain J_C for both pure and doped MgB₂ samples show similar behavior in the entire magnetic field studied. This is an advantage for making long length multifilamentary MgB₂ wires and coils with better $J_C(H)$ characteristics, in contrast to the degradation due to grain boundary induced weak links which is a common and serious problem in cuprates.

6.2.4: Conclusion

Multifilamentary MgB₂ wires with different sheath configurations are prepared and the effect of the outer sheath materials such as Cu, Fe and Ni on the transport properties of the wires is studied for a typical 4 filament configuration. It is observed that the core density of MgB₂ increases in accordance with the increase in hardness of the outer sheath material which in turn improves the self-field transport J_C . The choice of Ni as outer sheath and Cu filament as stabilizer is found to be the best configuration yielding the highest J_C . The influence of typical nano dopants on the in-field transport J_C of multifilamentary MgB₂/Fe/Cu/Ni wires is also examined. At higher fields, the doped multifilamentary wires exhibit highly enhanced $J_C(H)$ performance when compared to the pure sample. For the codoped samples, both substitution of C at the B site and flux pinning due to the reacted phases like Mg₂Si and HoB₄ contribute to the strong enhancement of transport J_C , significantly higher than the monodoped ones. In short, the in-field J_C of doped MgB₂ multifilamentary wires shows excellent performance, even better than the corresponding bulk samples.

6.3: Electromechanical properties of multifilamentary wires and development of MgB₂ coil

Large scale superconducting electric devices for the power industry, such as high field magnets, fault current limiters, motors and generators, superconducting magnetic energy storage systems, and transformers; depend critically on long length wires with high critical current densities at temperatures where cryogenic refrigeration efficiency is acceptable. AC losses are also an issue in power system design and MgB₂ seems to have the potential to become a good low loss superconductor operating in the 15-30

K range [12]. The losses like hysteresis loss developed in a superconductor are proportional to the width of the superconducting filament. However, appropriate filamentation and reduction of filament size i.e. the use of multifilamentary wire geometry is a solution to reduce this and it is much easier in MgB_2 as compared to HTS. The metallic matrix of the barriers and stabilizers used in multiwires not only reduces the hysteretic losses by the filamentation but also enables proper current sharing within the strand. The development of multifilamentary MgB_2 conductors is proceeding with increasing prospects. But it is highly essential to characterize long length multiwires in coil forms so as to accomplish excellent properties over long length making it appropriate for specific applications. Compared with low temperature superconductors, the life cycle costs of MgB_2 coils are lower due to the higher operating temperature and associated refrigeration cost. The coil and magnet applications such as MRI and high field magnets are likely in 20-30 K range, taking advantage of the improved high field performance of MgB_2 at these temperatures. But on switching over from multifilamentary wires to coils one should also certainly consider its mechanical stability to withstand applied stresses and strains along with their effect on J_C . It is often observed that severe degradation of J_C is caused by strains induced from deformation like bending [13]. The present section elucidates the preparation of 4, 8 and 16 filament MgB_2 multifilamentary wires (labeled as MB4, MB8 and MB16) and the effect on transport J_C by the strain developed in the short length pieces of these wire samples bent to different diameters. In order to check the homogeneity of J_C along the long length multiwires, a typical MgB_2 coil is also developed using wind and react (WaR) method which is also detailed in the section.

6.3.1: Preparation and characterization:

6.3.1.1: Variation in filament configuration

The MgB_2 multifilamentary wires were fabricated by PIT technique followed by WIT method. As discussed in previous section (*section 6.2.2*), Fe tubes (OD/ID: 5/3 mm) were chosen as the barrier material for the superconducting core. After filling the (Mg+B) powder in the Fe tube, the composite tube was groove rolled down to 1.33 mm OD. The as prepared

monofilamentary wires were cut, bundled and packed inside Ni tubes of different OD/ID: 6/4, 8/6 and 10/8 mm for the preparation of 4, 8 and 16 filamentary MgB₂ multiwires respectively (details are given in *table 6.3*). Cu wires of diameter 0.7 mm were also inserted appropriately in the Ni tube along with the monofilaments for thermal stabilization of the conductor. After rolling down to 1.33 mm OD, the composite wires were cut into short length pieces for further analysis and heat treatment. After sealing the ends by capping technique, the wires were heat treated at 650 °C for 2 hrs.

Table 6.3: Processing parameters for 4, 8 and 16 filamentary MgB₂ multiwires

Processing parameters for MgB ₂ multiwires	MB4	MB8	MB16
Fe tube for PIT: OD/ID	5/3 mm		
Powder packing density	1 g/cm ³		
Final OD of MgB ₂ /Fe	1.33 mm		
Ni tube for WIT: OD/ID	6/4 mm	8/6 mm	10/8 mm
No. of MgB ₂ /Fe fils.	4	8	16
Stabilizer material	Cu _r (0.7 mm OD)		
Fill factor	~10		
Avg. area reduction per pass	~3 %		
Final OD of MgB ₂ /Fe/Cu/Ni	1.33 mm		
Heat treatment temp.	650 °C		

6.3.1.2: Bent & react and react & bent wires

The as prepared 4, 8 and 16 filament multiwires cut into equal lengths were categorized into two sets:

- (1) Bent and react (BaR) - multiwires bent before heat treatment
- (2) React and bent (RaB) - multiwires bent after heat treatment

The bent samples were prepared by bending the sample into circular arcs of different radius of curvatures with the help of cylindrical mandrels to produce desired bending strains. A schematic illustration and a photograph of the bent wires are shown in *figure 6.7* where an initially straight piece of multifilamentary wire was bent to different arcs of diameters 15, 10, 5 and

2.5 cm, respectively. The bending strain measurements were performed on both two sets of wires.

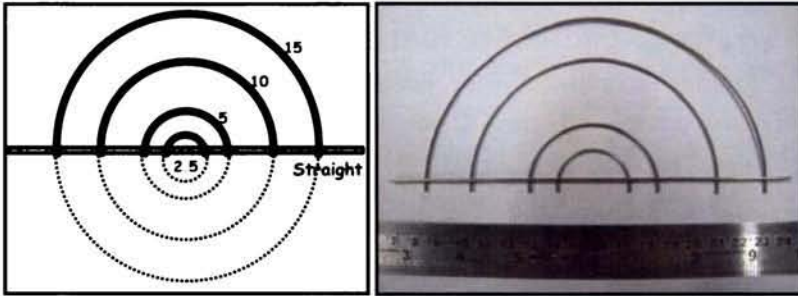


Figure 6.7: Schematic diagram and photograph of a typical set of straight and bent MgB_2 multiwires

6.3.1.3: MgB_2 coil

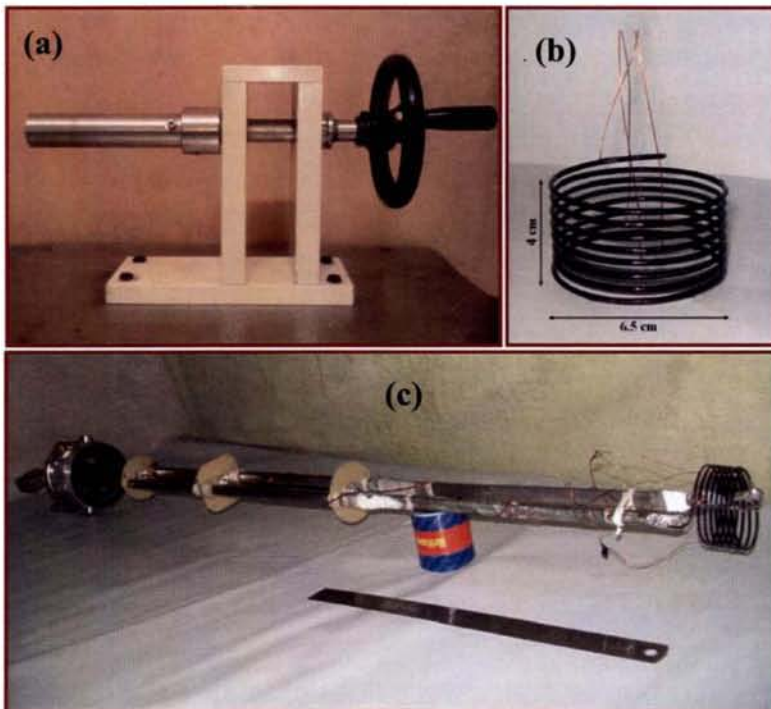


Figure 6.8: Photographs of (a) the winding device used for making MgB_2 coil (b) typical MgB_2 coil made using wind and react method (c) MgB_2 coil anchored to the high current insert of a liquid He cryostat for I_c measurement

An MgB_2 multifilamentary coil in the form of a solenoid is also fabricated by the wind and react method using a 1.65 m long 4 filamentary $MgB_2/Fe/Cu/Ni$ composite wire. The preparation is detailed in section 6.2.2. The coil is made with the help of a winding device as shown in figure 6.8 (a). The wound coil is coated with a cryostable epoxy resin (stycast) for insulation. The processing parameters used for the preparation of the coil are given in table 6.4. The self-field transport J_C of the coil is measured in liquid helium using *dc* pulse four probe resistive method.

Table 6.4: Processing parameters for $MgB_2/Fe/Cu/Ni$ multifilamentary coil

Processing parameters for MgB_2 coil	
Fe tube for PIT: OD/ID	5/3 mm
Powder packing density	1 g/cm ³
Final OD of MgB_2/Fe	1.33 mm
Ni tube for WIT: OD/ID	6/4
No. of MgB_2/Fe fils.	4
Stabilizer material	Cu_r
Fill factor	~10
Avg. area reduction per pass	~3 %
Final OD of $MgB_2/Fe/Cu/Ni$	1.65 mm
Final length of $MgB_2/Fe/Cu/Ni$	1.65 m
Coil diameter	6.5 cm
Coil length	4 cm
No. of turns	8
Heat treatment temp.	650 °C

6.3.2: Results and discussion

The multifilamentary MgB_2 wires of different filament configurations were examined using an optical microscope to study the internal cracks, if any, in MgB_2 core, interfacial reactions between the core

and sheath material and uniformity in core area. Figure 6.9 shows the optical micrographs of the cross sections of 4, 8 and 16 filamentary MgB_2 multiwires. The MgB_2 core can be seen clearly in the micrographs of all the multiwire samples. Similarly, in all samples, the core-sheath interface is observed to be distinct, indicating the non reactivity of the core with the barrier material Fe. The Cu filaments are also visible without any significant diffusion between the barrier and outer sheath metals.

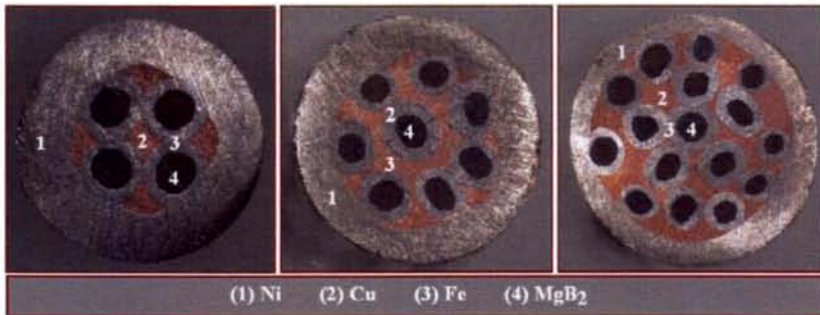


Figure 6.9: Optical micrographs of the cross sections of 4, 8 and 16 filamentary MgB_2 multiwires

Table 6.5: Bending parameters for MB4, MB8 and MB16 multiwires

Diameter (cm)	Strain (%)
15	0.8
10	1.3
5	2.6
2.5	5.0

In order to understand the effect of bending strain of the 4, 8, and 16 filament multiwires, both BaR and RaB sets of wires bent to different bending diameters were subjected to microstructural and transport characterizations. Bending of all the samples was done at room temperature and the bending strain, ξ was determined using the equation,

$$\xi = \left(\frac{d}{D+d} \right) \times 100$$

Here, d is the diameter of the multifilamentary wire and D is the bending diameter. The bending strain corresponding to each bending diameter is tabulated in *table 6.5*. As expected, the bending strain becomes higher as the bending radius decreases.

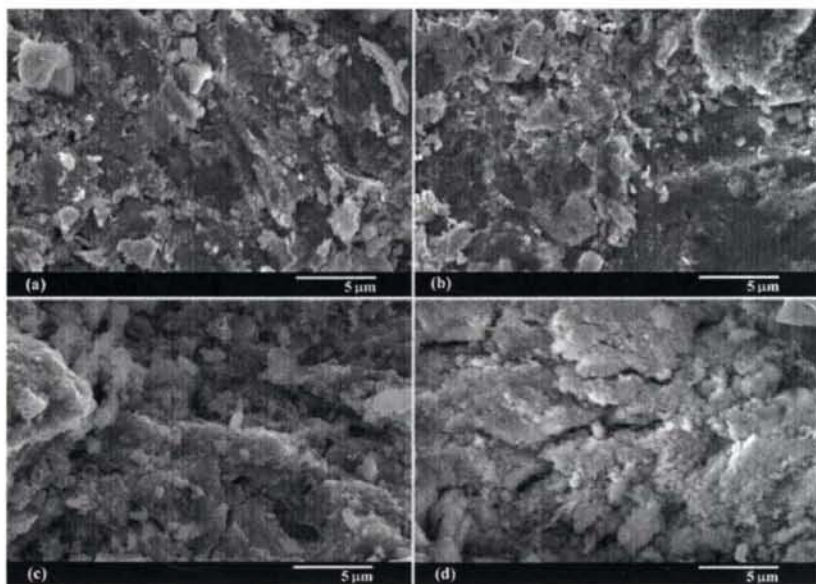


Figure 6.10: Typical SEM images of multifilamentary MgB_2 (a) straight wire, (b) & (c) BaR wires with bending diameters of 10 & 2.5 cm respectively and (d) RaB wire with 10 cm diameter

Figure 6.10 gives typical SEM images of cross sections of 4 filamentary MgB_2 multiwires with and without bending at room temperature. It is observed that there are no micro level cracks or breaks in the superconducting core of the straight multiwire. The SEM image of BaR multiwire with bending diameter of 10 cm also indicates that there are no cracks in the sample which was bent and then heat treated. While cracks are visible in RaB sample with bending diameter of 10 cm which was bent after being fully heat treated and the level of cracking increases further with decrease in bending diameter. It is evident that enough cracks are generated in the as rolled multiwires during bending and the heat treatment process followed after bending could heal the cracks during the *in situ* formation of the superconducting phase. The microstructure of the BaR multiwire sample

with a 2.5 cm bending diameter shows minor micro level cracks which is due to the incomplete healing of the relatively larger cracks produced in the post heat treatment stage. This is quite obvious as the bending strain and corresponding level of cracking are comparatively higher in the wire with such a lower bending diameter.

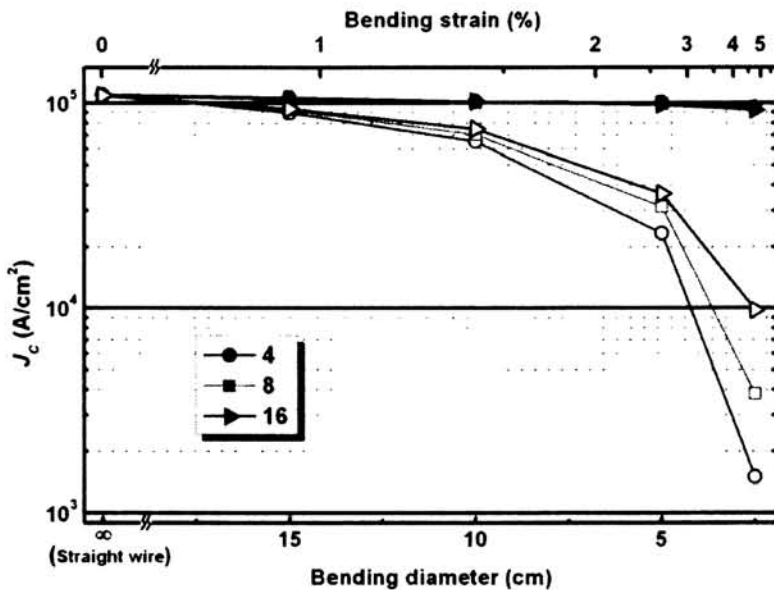


Figure 6.11: Variation of J_C with bending diameters and strain in 4, 8 and 16 filamentary MgB_2 multiwires for both BaR (closed) and RaB (open) sets at 4.2 K

Figure 6.11 shows the plots of self-field transport J_C as a function of bending diameter and strain for 4, 8 and 16 filamentary MgB_2 multiwires for both BaR and RaB sets at 4.2 K. The filamentation of MgB_2 wire into 4, 8 and 16 filament geometry has negligible impact on the transport J_C of BaR wires down to a bent diameter of 5 cm, while for RaB wires degradation of J_C is found to be lesser for higher filament numbers. Also on comparing the BaR and RaB sets, the degradation of J_C with decreased bending diameter is rapid for the latter, i.e. the wires that are bent after being fully heat treated; while the degradation of J_C for the former, i.e. the wires that are heat treated after bending, is not significant even down to a bending radius of 5 cm. The reduction of J_C with respect to bending strain for the MgB_2 BaR multiwires

is only 4.5 % of the J_C obtained for the straight sample after bending to a diameter of 5 cm. Whereas the RaB multiwire shows a 14 % J_C reduction that begins itself from the 15 cm diameter and thereafter the reduction rate is rapid which reaches up to 78.8 % for 4 filamentary multiwire with a bending diameter 5 cm. The microstructural analysis discussed above explains this J_C behavior wherein a larger degradation of J_C occurs in RaB wires compared to BaR due to the cracks formed in the MgB_2 core of the former while bending after reaction. As expected, for both BaR and RaB multiwires, the degradation of J_C with bending strain reduces with increase in filament number. In a nutshell, the BaR set of MgB_2 multifilamentary wires sustain a major portion of their J_C even after bending to a diameter of 5 cm.

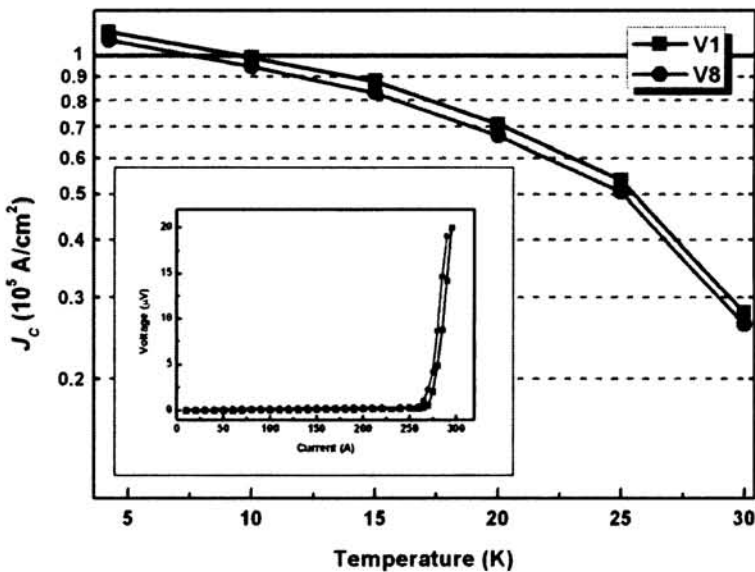


Figure 6.12: $J_C(T)$ plots of MgB_2 coil measured using two different voltage taps across a single turn and 8 turn. Inset shows $I-V$ plots of the same at 4.2 K

A typical long length 4 filamentary MgB_2 multiwire was successfully fabricated. The ability of BaR multiwires to sustain a major portion of J_C up to a diameter of 5 cm prompted us to follow the wind and react (WaR) method to prepare a coil having a bending diameter of 6.5 cm. A bending diameter of 6.5 cm was chosen not only to compromise the

bending strain but also to suite the inner diameter of the cryostat used for measurement. *Figure 6.12* shows the variation of self-field J_C with temperature (4.2-32.5 K) of the MgB₂ coil measured across two voltage taps labeled as V1 and V8, which are the voltages measured across a single turn of length ~20.5 cm in the middle and the other across 8 turns i.e. the whole length ~165 cm, respectively. The reduction of J_C with respect to temperature shows similar behavior across both single turn and whole length. The result shows that there is only a difference of 4 % between the whole length and single turn J_C at 4.2 K and it slightly increases to 6 % at 32.5 K. Typical I - V plots of the measurements across single turn and 8 turn of the coil at 4.2 K are given as an inset of *figure 6.12*. The I_C of the single turn is 270 A corresponding to a J_C of 1.08×10^5 A/cm², while the I_C of 8 turn is found to be 260 A which corresponds to a J_C of 1.04×10^5 A/cm². The results of this study strongly suggest that the performance of the MgB₂ coil has been quite satisfactory with respect to the whole length critical current and its homogeneity over short sections. Nevertheless, taking into account that the present work is just a preliminary study of coil fabrication, it is expected that the transport performance of MgB₂ coils can be further improved by optimizing the fabrication parameters of the wire and coil.

6.3.3: Conclusion

MgB₂/Fe/Cu/Ni multifilamentary wires with 4, 8 and 16 filament configurations were successfully fabricated. The transport J_C of 4, 8 and 16 filamentary MgB₂ multiwires was almost comparable at self-field and 4.2 K which indicates that filamentation of multiwires into 4, 8 and 16 filament geometry has negligible impact on the transport properties of MgB₂ wires. The effect of bending strain on transport properties of these multifilamentary wires was also investigated. Only a very small reduction of J_C (4.5 %) was obtained in multiwires heat treated after bending even up to a diameter of 5 cm. This prompted us to develop a prototype MgB₂ coil having an OD of 6.5 cm and length ~165 cm using the wind and react approach. An overall homogenous $J_C \sim 10^5$ A/cm² was achieved in the coil at 4.2 K. Moreover, there was only a difference of 4 % between the whole length and single turn J_C at 4.2 K which slightly increased to 6 % at 32.5 K. Thus, it became clear that the fabrication of long length multifilamentary

wires and their transformation into coils using *in situ* wind and react method can be realized without much J_C degradation along the whole length.

6.4: Development of MgB_2 based current lead

Many superconducting devices operate at high currents which must be transmitted from room temperature to an operating temperature around 5-20 K. Current leads with high current carrying capacity and lower thermal conductivity are essential in order to minimize the heat input into the cryogenic system. In addition, current leads must also have the ability to withstand repeated thermal and current cycles. It must also endure fault conditions such as loss of coolant or power failure without much degradation. Before the advent of HTS, current leads made of normal metals especially Cu based conductors were employed for the above purpose. Cu based current leads have two main drawbacks: firstly the conductive heat leak from the hot end to the low temperature source due to the high thermal conductivity and secondly, the joule heating due to the inherent electrical resistance. This leads to a huge consumption of expensive liquid helium.

HTS current leads were found to be advantageous over the Cu based ones because of their high critical current density and low thermal conductivity with operating temperatures easily achievable using liquid nitrogen [14-16]. But HTS are restricted to oxygen permeable and flexible sheath material such as silver or silver alloys. Whereas for MgB_2 composites, economic sheath materials having enough mechanical strength and workability can be used as outer sheaths. Moreover, the relatively high T_C of 39 K allows the use of this material at elevated temperatures up to 20-30 K which is above the T_C of NbTi or Nb₃Sn. These temperatures are easily attainable with cryocoolers, or even with coolants like liquid hydrogen or liquid neon. Another advantage of MgB_2 is the fact that it is not mandatory to texture this material in order to get high critical current densities. Hence, we made an effort to develop an MgB_2 based current lead and the present section gives a compendium on the preparation and characterization of the same.

6.4.1: Preparation and characterization of MgB_2 current lead

The MgB_2 based current lead is fabricated by PIT technique followed by WIT method. The current lead is fabricated in the shape of rods with the dimensions; OD: 5.8 mm and length; 20 cm. This shape is chosen to provide current flow in such a manner so as to reduce the current induced self magnetic field which varies as $1/r$ (where r is the radius) and to reduce the Lorentz forces between high current conductors. As discussed in previous sections, thoroughly mixed Mg and B powders were filled in Fe tube (OD/ID: 5.7/4.5 mm) and groove rolled down to 2.3 mm. The as prepared monofilamentary wires were cut, bundled and packed inside Ni tube (7.8/6.4 mm) for the preparation of 4 filamentary MgB_2 composite. The low thermal conductivity of Ni helps in minimizing the heat losses from the warm end of the MgB_2 composite to the cold end. Five Cu wires of diameter 1 mm were also inserted appropriately in the Ni tube along with the mono filaments for adequate thermal stabilization of the conductor. After rolling down to 5.8 mm OD and sealing the ends, the composite was heat treated at $675\text{ }^\circ\text{C}/2\text{ hrs}$. One of the major concerns in this experiment is the proper attachment of the normal current lead to the superconducting sample. At high currents, large contact resistances can limit the critical current. To minimize this problem, the end portions of the MgB_2 composite were soldered into the copper end caps used for anchoring the leads to the measurement system. Schematic diagram and photographs of longitudinal and sectional views of the MgB_2 current lead are shown in *figure 6.13* and *figure 6.14* respectively.

The transport current measurements were carried out using an indigenously designed cryostat integrated with an imported cryocooler. The flanges at the two stages of the cryocooler are suitably extended by providing additional strips to anchor the test current leads. Sectional views of the cryocooler integrated cryostat are shown in *figure 3.4* (*chapter 3*). Provision is made at one side of the chamber for inserting high current feed through of capacity ranging from 100-1200 A which supply power to the test leads. During operation, the current lead is anchored between the two stages so that it gets cooled by conduction mode. Necessary heaters are provided at both the stages for controlling the stage and sample

temperatures. The schematic diagram and photograph of MgB_2 current lead test facility are shown in *figure 6.15*. It is possible to achieve a temperature of ~ 25 K in stage-1 and ~ 7 K in stage-2 without any thermal load by continuously operating the cryocooler. The transport current measurements were carried out by *dc* pulse four probe resistive method with current fed to current lead from a programmable current source. A nano voltmeter is used to measure the voltage drop across the inner terminals. Sufficient spacing is provided between the current and voltage taps to ensure uniform current distribution in all the strands. Table 6.6 shows the processing parameters used for the preparation of MgB_2 based superconducting current lead.

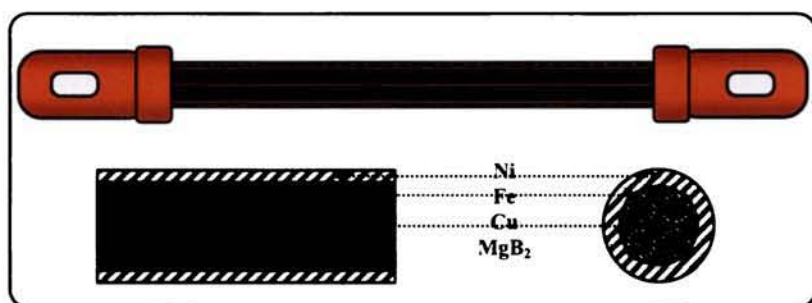


Figure 6.13: Schematic diagram of MgB_2 based current lead

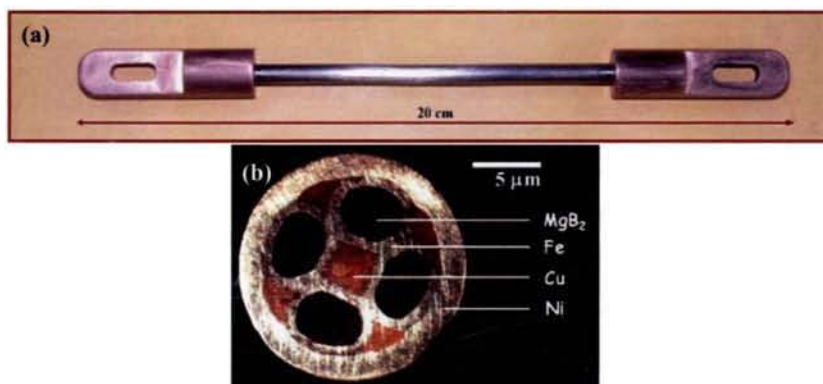


Figure 6.14: (a) Longitudinal and (b) sectional views of current lead

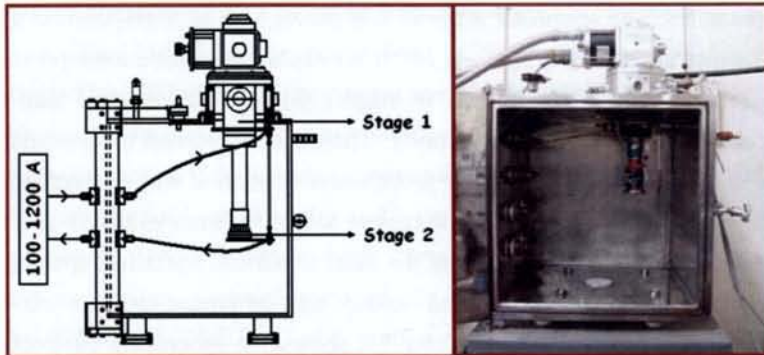


Figure 6.15: Schematic diagram and photograph of experimental set up for MgB_2 based current lead

Table 6.6: Processing parameters of MgB_2 based superconducting current lead

Specifications of MgB_2 current lead	
Fe tube for PIT: OD/ID	5.7/4.5 mm
Powder packing density	1 g/cm ³
Final OD of MgB_2/Fe	2.3 mm
Ni tube for WIT: OD/ID	7.8/6.4
No. of MgB_2/Fe fils.	4
Stabilizer material	Cu_r
Area fraction of metallic matrix	Fe-22%, Cu-12%, Ni-40 %
Fill factor of superconducting core	26%
Processing temperature	675 °C
Final OD & length of MgB_2 composite	5.8 mm & 10 cm
Current lead end terminals	Copper
Total length of current lead	20 cm
I_C rating	1000 A (20-37 K)
Conductive heat leak of current lead	<1 W (10-37 K)

6.4.2: Results and discussion

A Ni sheathed and Cu stabilized 4 filamentary MgB_2 based current lead is successfully fabricated. Figure 6.16 shows a typical self-field I - V plot of MgB_2 based current lead at 20-37 K. The current lead shows an I_C of 1050 A and an equivalent J_C of 10^4 A/cm² at 20-37 K. The lead is expected to carry a critical current of 3000 A if anchored between 4.2 and 20 K.

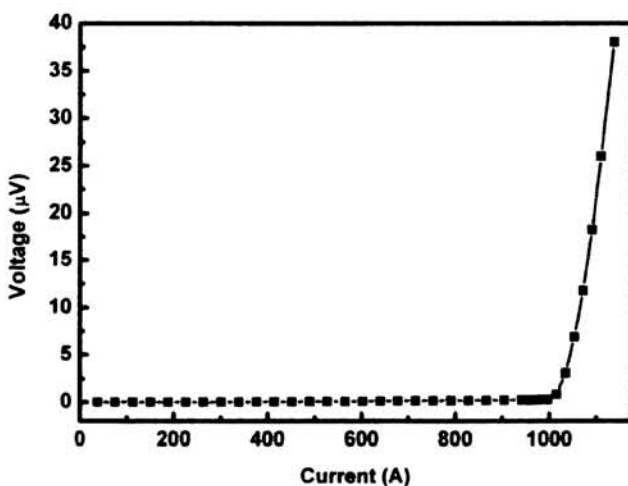


Figure 6.16: Typical I - V plot of MgB_2 based current lead at 20-37 K

It is very important to determine the conductive heat leak of a current lead before it is put into any application. Conductive heat leak of a current lead is defined as the heat flow from the 'warm' end (T_2) to the 'cold' end (T_1) when the lead is anchored between T_2 and T_1 . It is estimated by measuring the increase in temperature of the cold end when the ends of the lead are anchored between the two desired temperatures T_1 and T_2 . In the present work, heat leak of the leads is measured by keeping T_1 at 10 K and T_2 at 37 K. For this, the cryocooler is operated continuously without connecting the load till stage-1 and stage-2 reach the lowest possible temperatures (say 25 K and 7 K respectively). By controlling the heater currents at both stages the temperatures are set to the desired values T_1 and T_2 (say $T_1 = 10$ K and $T_2 = 37$ K). Having known the heater power required for keeping the stage temperatures at T_1 and T_2 , put off the cryocooler and allow the cryostat to reach room temperature. Now anchor the lead

between the stages and operate the cryocooler till the stages reach the lowest possible temperatures. Switch on the heaters at both stages and control the heater power such that the stage-2 heater has exactly the same power as given earlier and stage-1 temperature reaches the desired temperature T_2 (say 37 K). On attaining steady state, the stage-2 temperature will show a temperature slightly higher than T_1 (say > 10 K). The increase in temperature of stage-2 corresponds to the conductive heat leak from the warm end to the cold end. The power required for the increase in the stage-2 temperature is measured by applying an additional known power to the stage-2 without connecting the test lead. The conductive heat leak of the lead thus estimated is found to be < 1 W.

6.4.3: Conclusion

A general purpose conduction cooling type current lead based on MgB₂/Fe/Cu/Ni with a rating of 1000 A (20-37 K) has been successfully developed. The lead was subjected to transport critical current measurements under conduction cooling mode using a closed cycle cryocooler integrated cryostat. The conductive heat leak of the lead was estimated which is about 30 times less than that of conventional OFHC leads.

6.5: Summary

Multifilamentary wires with different configurations were developed and the effect of the outer sheath materials such as Cu, Fe and Ni on the transport properties of MgB₂ multifilamentary wires was studied for a typical 4 filament configuration. The choice of Ni as outer sheath and Cu filament as stabilizer was found to be the best configuration to yield high transport J_C . The influence of typical nano dopants on the in-field transport J_C of multifilamentary MgB₂/Fe/Cu/Ni wires was also examined. The in-field J_C of doped MgB₂ multifilamentary wires showed excellent performance, relatively better than the corresponding bulk samples. MgB₂/Fe/Cu/Ni multifilamentary wires with 4, 8 and 16 filament configurations were also fabricated. The transport J_C of 4, 8 and 16 filamentary MgB₂ multiwires was almost comparable at self-field and 4.2 K indicating that filamentation of multiwires has negligible impact on its

transport properties. In addition, the bending strain studies of these multifilamentary wires exhibited better transport J_C for multiwires heat treated after bending which remained almost constant even up to a diameter of 5 cm. Following the successful fabrication of multifilamentary wires, a prototype MgB₂ coil having an OD of 6.5 cm and length 4 cm was developed using the wind and react approach. An overall homogenous J_C $\sim 10^5$ A/cm² was achieved in the coil at 4.2 K. A general purpose conduction cooled current lead based on MgB₂/Fe/Cu/Ni with a rating of 1000 A (20-37 K) was also successfully developed. The leads were further subjected to various tests such as rated current and conductive heat leak under conduction cooling mode using a closed cycle cryocooler integrated cryostat. The conductive heat leak of the lead is found to be <1 W which is about 30 times less than OFHC leads of identical current rating.

References:

1. H. Fang, S. Padmanabhan, Y. X. Zhou and K. Salama, *Appl. Phys. Lett.* 82, 4113 (2003)
2. W. Goldacker, S. I. Schlachter, B. Liu, B. Obst and E. Klimenko, *Physica C* 401, 80 (2004)
3. M. Tomsic, M. Rindfleisch, J. Yue, K. McFadden, D. Doll, J. Phillips, M. D. Sumption, M. Bhatia, S. Bohnenstiehl and E. W. Collings, *Physica C* 456, 203 (2007)
4. V. Braccini, D. Nardelli, R. Penco and G. Grasso, *Physica C* 456, 209 (2007)
5. O. Sangjun, J. H. Kim, L. Chulhee, C. Heekyung, C. J. Kim, S. X. Dou, M. Rindfleisch and M. Tomsic, *Physica C* 468, 1821 (2008)
6. M. D. Sumption, M. Bhatia, X. Wu, M. Rindfleisch, M. Tomsic and E. W. Collings, *Supercond. Sci. Technol.* 18, 730 (2005)
7. H. Kumakura, A. Matsumoto, H. Fujii and K. Togano, *Appl. Phys. Lett.* 79, 2435 (2001)
8. M. D. Sumption, M. Bhatia, M. Rindfleisch, M. Tomsic and E. W. Collings, *Supercond. Sci. Technol.* 19, 155 (2006)

9. E. Martinez, F. Lera, M. Martinez-Lopez, S. I. Schlachter, P. Lezza and P. Kovac, *Supercond. Sci. Technol.* 19, 143 (2006)
10. M. N. Wilson, *Superconducting Magnets (Oxford: Oxford University Press)* (1983)
11. P. Kovac, I. Husek, T. Melisek, E. Martinez and M. Dhalle, *Supercond. Sci. Technol.* 19, 1076 (2006)
12. M. Tomsic, M. Rindfleisch, J. Yue, K. McFadden and J. Phillips, *Int. J. Appl. Ceram. Technol.* 4, 250 (2007)
13. K. Salama, Y. X. Zhou, M. Hanna, M. Alessandrini, P. T. Putman and H. Fang, *Supercond. Sci. Technol.* 18, S369 (2005)
14. D. U. Gubser, M. M. Millee, L. Toth, R. Rayne, S. Lawrence, N. M. Alford and T.W. Buttons, *IEEE Transactions On Magnetics* 27, 2 (1991)
15. R. Wesche, R. Heller, P. Bruzzone, W. H. Fietz, R. Lietzow and A. Vostner, *Fusion Engineering and Design* 82, 1385 (2007)
16. W. H. Fietz, R. Heller, A. Kienzler and R. Lietzow, *IEEE Transactions On Applied Superconductivity* 19, 3 (2009)

7

SUMMARY AND CONCLUSIONS

7.1: Summary

As against the objectives of the thesis highlighted in *Chapter 2*, the overall work done can be consolidated under the following categories: *(a) Effect of processing temperature and various nano dopants on the properties of bulk MgB₂, (b) Optimization of processing parameters and novel preparation techniques for MgB₂ wires and (c) Development of MgB₂ multifilamentary wires, coils and current leads for technological applications.*

The superconducting properties of bulk *in situ* PIST MgB₂ processed at temperatures in the range 750-900 °C were studied. Since the samples heat treated at relatively lower temperatures particularly at 800 °C exhibited best $J_c(H)$ performance, this temperature was chosen for further chemical addition/doping using nano dopants in bulk MgB₂ to enhance J_c at higher magnetic fields. Nano SiO₂ and typical nano rare earth oxides like Tb₄O₇ and Ho₂O₃ were initially tried as nano inclusions for studying their effect on J_c and flux pinning. Later on carbon based dopants such as nano carbon, nano diamond, nano SiC and burned rice husk (BRH) were chosen to enhance $J_c(H)$ property through carbon substitution. Finally, the combined effect of both substitution and inclusions on the enhancement of J_c using typical combinations of above mentioned nano dopants was also analyzed.

In order to convert bulk MgB₂ into conductors fit for practical applications, efforts were made to optimize parameters such as sheath material reactivity and processing temperature. The role of the reactivity of commonly used sheath materials such as Cu, Ni, Fe and SS with Mg/B on the phase formation and superconducting properties of MgB₂ was studied. The effect of processing temperature on phase formation, microstructure and transport critical current of MgB₂ monofilamentary wire samples

processed at temperatures 600-800 °C were studied. Further, an attempt was made to lower the processing temperature of MgB_2 wires by the incorporation of nano Cu was quite successful. A novel preparative method was also demonstrated to fabricate Fe sheathed *in situ* MgB_2 superconducting tapes with high densities by hot-pressing of electrically self-heated PIT wires.

Subsequently multifilamentary wires with different configurations were developed and the effect of the outer sheath materials like Cu, Fe and Ni on the transport properties of MgB_2 multifilamentary wires was studied for a typical 4 filament configuration. The in-field transport J_C of MgB_2 multifilamentary wires doped with nano dopants which gave the best results for bulk MgB_2 was also studied. Thereafter, $\text{MgB}_2/\text{Fe}/\text{Cu}/\text{Ni}$ multifilamentary wires with 4, 8 and 16 filament configurations were successfully fabricated. The effect of bending strain on transport properties of these multifilamentary wires was also investigated. The promising results obtained from the studies on multifilamentary wires prompted to develop a prototype MgB_2 coil using the wind and react method and a general purpose current lead suitable for practical applications.

7.2: Conclusions

- ☛ *The optimization of processing temperature for bulk in situ PIST MgB_2 showed that 800 °C is the optimum processing temperature since it gives the best $J_C(H)$ performance. The reduced grain size and hence increased grain boundary is the main reason behind the improved flux pinning and $J_C(H)$ for the samples sintered at lower temperatures.*
- ☛ *Addition of nano sized oxides in bulk MgB_2 exhibited enhanced $J_C(H)$ behavior for the doped samples as compared to pure MgB_2 . Among the different additives tried, nano Ho_2O_3 doped MgB_2 gave the maximum flux pinning behavior in the entire field of study. In all samples, the addition induced reacted phases act as strong flux pinners thereby improve the $J_C(H)$ and H_{irr} of the nano oxide added samples.*

- ☛ *On comparing the effect of various carbon based dopants in MgB_2 , all of them showed competitively enhanced in-field critical current density. In the case of n-SiC and BRH doped samples, both C substitution and the presence of Mg_2Si caused enhanced flux pinning and hence $J_C(H)$ while for n-C doped one C substitution is solely the reason.*
- ☛ *The codoping of n- Ho_2O_3 with n-SiC and BRH exhibits excellent flux pinning performance and J_C enhancement up to a field of 8 T as compared to pure and their corresponding monodoped samples. The C substitution at B site by carbon dopants and the formation of Mg_2Si and magnetic particles like HoB_4 by Ho_2O_3 as flux pinners are the reasons for the strong improvement of $J_C(H)$ in these samples.*
- ☛ *For conductor fabrication, the role of the reactivity of sheath material with Mg/B on the phase formation and superconducting properties of MgB_2 was studied. Fe and SS added samples gave higher volume fraction of MgB_2 core and hence better $J_C(H)$ characteristics which infers that Fe and SS are more suitable sheath materials in MgB_2 wire fabrication.*
- ☛ *The effect of processing temperature on phase formation, microstructure and transport critical current of MgB_2 monofilamentary wire samples processed at temperatures 600-800 °C was studied. The sample processed at 650 °C gave the best self-field transport J_C value of 1.19×10^3 A/cm² at 7 K. The presence of reasonable amount of unreacted Mg and the reduced grain size are the reasons for enhancing the critical current of the sample processed at 650 °C.*
- ☛ *An attempt to lower the processing temperature of MgB_2 wire showed that a substantial reduction in the processing temperature (~ 550 °C) can be achieved using nano Cu as an additive. The transport J_C of Cu added wire processed at 550 °C is quite comparable with that of Cu-free wire processed at 650 °C.*
- ☛ *A simple and easy method for preparation of in situ MgB_2 superconducting tapes with highly densified core has been*

demonstrated. A core density of 2.45 g/cm^3 and nearly 4-fold increase in critical current are achieved for the best hot-pressed sample.

- ☛ Development of multifilamentary wires with different configurations was carried out and the effect of the outer sheath materials like Cu, Fe and Ni on the transport properties of MgB_2 multifilamentary wires was studied for a typical 4 filament configuration. The choice of Ni as outer sheath and Cu filament as stabilizer proved to be the best configuration yielding higher transport current.
- ☛ The influence of typical nano dopants on the in-field transport J_C of multifilamentary $\text{MgB}_2/\text{Fe}/\text{Cu}/\text{Ni}$ wires was examined. Both substitution of C at the B site and flux pinning due to the reacted phases like Mg_2Si and HoB_4 contribute to the strong enhancement of J_C , significantly higher than the monodoped ones as observed in their respective bulk samples.
- ☛ $\text{MgB}_2/\text{Fe}/\text{Cu}/\text{Ni}$ multifilamentary wires with 4, 8 and 16 filament configurations were successfully fabricated. The transport J_C of 4, 8 and 16 filamentary MgB_2 multiwires was almost comparable at self-field and 4.2 K which indicates that filamentation of multiwires into 4, 8 and 16 filament geometry has negligible impact on the transport properties of MgB_2 wires.
- ☛ The effect of bending strain on the transport properties of multifilamentary wires was also investigated. It was observed that almost constant transport J_C was obtained in 4, 8 and 16 filamentary MgB_2 multiwires heat treated after bending even up to a diameter of 5 cm.
- ☛ A prototype MgB_2 coil having an OD of 6.5 cm and length ~ 165 cm was developed using the wind and react approach. An overall homogenous $J_C \sim 10^5 \text{ A/cm}^2$ was achieved in the coil at 4.2 K.
- ☛ A general purpose conduction cooling type current lead based on $\text{MgB}_2/\text{Fe}/\text{Cu}/\text{Ni}$ with a rating of 1000 A at 20-37 K has been successfully developed.

7.3: Scope for future work

The present thesis focused on the optimization of processing parameters and enhancement of in-field critical current density in bulk MgB_2 through doping. The results obtained in bulk MgB_2 were successfully used for the development of good quality mono/multifilamentary wires, coils and current leads with an application point of view. Though much effort has been taken to bring out the potential of MgB_2 for technological applications, there are still certain areas both in bulk and conductor development which need further attention.

The issues to be addressed regarding the bulk MgB_2 are:

- ✧ To enhance self-field J_c of bulk MgB_2 by improving the core density using different preparation techniques.
- ✧ Fine tuning of the C and SiO_2 in rice husk by suitable heat treatment to optimize the ratio of C to SiO_2 .
- ✧ To explore further on natural and economic alternatives like BRH for expensive C based nano dopants.

While considering conductor development focus must be given on:

- ✧ Finding more dopants like Cu for reducing the processing temperature of MgB_2 .
- ✧ Studying the influence of self-heating and hot-pressing on the doped variants of MgB_2 .
- ✧ Improving the fill factor of superconducting core in multifilamentary MgB_2 wires without affecting its stability.
- ✧ Making appropriate modifications in the MgB_2 superconducting coil demonstrated so as to make it suitable for superconducting magnet applications such as in MRI.
- ✧ Scaling up of the current rating of the MgB_2 based current lead without compromising its thermal stability.

List of Symbols

mK	: milli Kelvin
K	: Kelvin
T_C	: Critical temperature
H_C	: Critical field
J_C	: Critical current density
$J_C(H)$: In-field critical current density
λ	: London penetration depth
ξ	: Coherence length
H	: Magnetic field
H_{C1}	: Lower critical field
H_{C2}	: Upper critical field
H_{irr}	: Irreversibility field
ρ	: Resistivity
ρ_n	: Normal state resistivity
χ	: Magnetic susceptibility
$\Psi(\mathbf{r})$: Wave function
n	: Total number of free electrons
n_s, n_n	: Number of superconducting, non-superconducting electrons
T	: Temperature
I	: Current
V	: Voltage
R	: Resistance
R_{300K}	: Resistance at the temperature 300 K
K	: Ginzburg-Landau parameter
Φ_0	: Magnetic flux quantum
I_C	: Transport current
f_L	: Lorentz force per unit length
F_L	: Lorentz force per unit volume
F_P	: Pinning force per unit volume
Ω	: Unit of resistance
a, c	: Lattice parameters

a, b	: Sample dimensions
α	: Isotopic coefficient
$\Delta(0)$: Energy gap at 0 K
$T_{C\text{-onset}}$: Temperature corresponding to onset of transition
$T_{C\text{-offset}}$: Temperature corresponding to offset of transition
ΔT_C	: Width of transition
Θ_D	: Debye temperature
V	: Average matrix element of electron interaction
Λ	: Coupling constant between the electrons and phonons
$N(E_F)$: Electronic level density near the Fermi surface in the normal state
Å	: Angstrom unit
θ	: Angle of diffraction
σ	: σ bands
π	: π bands
d	: Inter atomic spacing
h, k, l	: Miller indices of crystal planes
M	: Magnetization
ΔM	: Width of the M - H Loop
F_P	: Flux pinning force density
F_{Pmax}	: Maximum flux pinning force density
d	: Diameter of the multifilamentary wire
D	: Bending diameter of the multifilamentary wire
ε	: Bending strain
T_1	: Temperature at the warm end of current lead
T_2	: Temperature at the cold end of current lead
r	: Radius of the MgB_2 current lead

List of Abbreviations

2D	Two Dimensional
3D	Three Dimensional
AC, <i>ac</i>	Alternating Current
AF _{MgB₂}	Area Fraction of MgB ₂ Core
AMI	American Magnetics Inc.
ARPES	Angle Resolved Photoemission Spectroscopy
BCS	Bardeen Cooper and Schrieffer
BaR	Bent and React
BRH	Burned Rice Husk
BSCCO	Bismuth Strontium Calcium Copper Oxide
Cu _f	OFHC- Cu filaments
DC, <i>dc</i>	Direct Current
DOS	Density of States
EDS/EDX	Energy Dispersive X-ray Spectroscopy
FWHM	Full Width at Half Maximum
HIP	Hot Isostatic Pressing
HPS	High Pressure Sintering
HRTEM	High Resolution Transmission Electron Microscope
HTS	High Temperature Superconductors
ID	Inner Diameter
ITER	International Thermonuclear Experimental Reactor
JNCASR	Jawaharlal Nehru Centre for Advanced Science and Research
LHe	Liquid Helium
LTS	Low Temperature Superconductors
MRI	Magnetic Resonance Imaging
OD	Outer Diameter
OFHC	Oxygen Free High Conductivity
PC	Personal Computer
PDOS	Partial Density of States
PIST	Powder In Sealed Tube

PIT	Powder In Tube
PPMS	Physical Property Measurement System
RaB	React and Bent
RE	Rare Earth
REO	Rare Earth Oxide
<i>rf</i>	Radio Frequency
RRCAT	Raja Ramanna Centre for Advanced Technology
SEM	Scanning Electron Microscope
SFCL	Superconductive Fault Current Limiters
SMES	Superconductive Magnetic Energy Storage
SQUID	Superconducting Quantum Interference Device
SS	Stainless Steel
TEM	Transmission Electron Microscopy
Vol%	Volume percentage
VSM	Vibrating Sample Magnetometer
VTI	Variable Temperature Insert
WaR	Wind and React method
WIT	Wire In Tube
wt%	Weight percentage
XAS	X-ray Absorption Spectroscopy
XES	X-ray Emission Spectroscopy
XRD	X-ray Diffraction
YBCO	Yttrium Barium Copper Oxide
ZFC	Zero Field Cooling

